

Experimental and Numerical Determination of the Constitutive Parameters of a Micro-Mechanical Material Model of a Single-phase Steel (S700)

A master thesis submitted by
Goodness Udochukwu, Okoh, B. Eng.
Matr.Nr.: 384649

To the faculty of
Georesources and Materials Engineering
Of the RWTH Aachen University

In partial fulfilment of the requirement for the award of a
Master of Science, M.Sc., degree in Metallurgical Engineering
(Specialization: Physical Metallurgy and Materials)

Under the Guidance of:
Prof. Dr.-Ing. habil Ulrich Krupp
Dr.-Ing. Christian Haase
Karthik Ramalingam, M. Sc.

At the
Institut für Eisenhüttenkunde, RWTH Aachen University
Intzestraße 1, 52072 Aachen

October 2021

Eigenständigkeitserklärung

Ich erkläre hiermit, die vorliegende Arbeit selbständig und ohne unzulässige fremde Hilfe angefertigt zu haben. Die verwendeten Quellen und Hilfsmittel sind im Literaturverzeichnis vollständig aufgeführt. Ich versichere alles kenntlich gemacht zu haben, was aus Arbeiten anderer unverändert oder mit Abänderungen übernommen wurde.

Aachen, 13 October 2021

Goodness Udochukwu, Okoh

Acknowledgement and Dedication

I wish to acknowledge all the shoulders upon which this work stands; the researchers who tirelessly seek to understand nature and whose quality research records have been used, my professors who have immensely imparted knowledge and the appreciation of questions from critical thought, my colleagues whose interactions help motivation, the Steel institute, IEHK for the opportunity to work within your research unit, Mr Karthik Ramalingam for his assistance in the course of this work, my parents for the labour of love and sacrifice, and Germany for the opportunity to partake in their heritage of world-class education within RWTH Aachen University at almost no cost. This work is dedicated to you all.

Abstract

Experimental and numerical methods based on a continuum dislocation density derived micro-mechanical model were applied to investigate the behaviour and determine the constitutive parameters of a micro-mechanical model of a single-phase steel (S700). The uniaxial tension test, using standard ASTM recommendations for sheet specimen, at strain rates range of $10^{-4}/s$ to $10^{-1}/s$, in the temperature range of $25^{\circ}\text{C} - 500^{\circ}\text{C}$ were performed to measure the flow properties, point-parameter optimization was executed based on the visco-plastic continuum dislocation density based model of material flow behaviour developed by Amir and Prahls to determine the constitutive parameters of the material, and simulation of the tensile test conditions in ABAQUS software using the user subroutine functionality and an explicit analysis based on the elastic predictor plastic corrector algorithm followed the experimental tests. The constitutive parameters obtained only fairly replicated the observed experimental data, and also, only incompletely simulated the test conditions. The constitutive parameters and its incapability are discussed based on the postulates of the model and already established knowledge.

Table of Content

Eigenständigkeitserklärung	i
Acknowledgement and Dedication.....	ii
Abstract.....	iii
Chapter 1: Introduction.....	1
1.1: Motivation	1
1.2: Objectives.....	2
1.3: Scope of this Work	2
Chapter 2: Overview on Metal Plasticity.....	3
2.1: Plastic Deformation and Process Conditions.	3
2.2: Characterization of Plastic Deformation	8
2.2.1: Mechanical Characterization.....	8
2.2.2: Microstructural Characterization	10
Chapter 3: Hardening.....	13
3.1: Classical Rate-Independent Hardening.....	13
3.2: The Mechanism of Deformation and Strain/Work Hardening.....	16
Chapter 4: Models of Flow Stress (Rate-Dependent Plasticity)	26
4.1: Engineering/Empirical/Semi-Empirical/Phenomenological Models	27
4.2: Microstructural/Physical Based Material Model	28
4.2.1: Flow Stress Model Based on Microstructural Dislocation Mechanics.....	30
4.2.2: Flow Stress and Strain Hardening Models Based on Microstructural Dislocation Density	38
4.3: Amir & Prahl Model.....	44
Chapter 5: Experiments	51
5.1: Chemical Composition	51
5.2: Preparation of Sheet Specimen	51
5.3: Electron Back Scatter Diffraction, EBSD, Measurement	51
5.4: Tensile Tests	52
Chapter 6: Results, Discussion and Validation.....	53
6.1: Chemical Composition.....	53

6.2: Tensile Test and Computational Curves	54
6.2.1: Processing the Uniaxial Tensile Test Data	54
6.2.2: Obtaining the Constitutive Parameters	54
6.2.3: Experimental and Numerical Flow Curve at 0.0001s (The Reference Strain Rate).	58
6.2.4: Experimental and Numerical Flow Curve at 0.001s	59
6.2.5: Experimental and Numerical Flow Curve at 0.01s	61
6.2.6: Experimental and Numerical Flow Curve at 0.1s	62
6.3: Strain Hardening Rate at all Test Strain Rate & Temperatures.....	69
6.4: Dislocation Density Evolution.....	78
6.4.1: Total Dislocation Density.....	78
6.4.2: Cell Mobile Dislocation Density.	80
6.4.3: Cell Immobile Dislocation Density.....	83
6.4.4: Wall Immobile Dislocation Density.....	85
6.5: Material Dislocation Process Coefficient.....	93
6.5.1: Trapping of cell mobile dislocation	93
6.5.2: Remobilization of Cell and Wall Dislocations.	94
6.5.3: Nucleation of Wall Immobile Dislocation.	96
6.5.4: Annihilation of Dislocation.....	97
6.6: Validation.	101
6.6.1: Validated Results.....	102
Chapter 7: Why is a Large experimental error and discontinuous trends in the dislocation coefficient obtained?	104
Chapter 8: Conclusion and Recommendation.	106
References	vi
List of Figures.....	xv
List of Tables	xvii
List of Equations	xvii

Chapter 1: Introduction

1.1: Motivation

In terms of importance to the infrastructure of power generation, transportation vehicles and engineering structures, now and into the foreseeable future, metals and their alloys represent the most economically significant class of engineered materials. The goal of tailoring the material microstructure to control plastic deformation and related failure processes is of great economic importance. Product development cycles have become so short that traditional empirical approaches to alloy modification are non-competitive in the global marketplace. Second, materials selection and design for durability, which rests upon our understanding of phenomena occurring at microstructural scales as well as at the scale of structural components, is of critical importance as we head into an era where an extensive infrastructure must be maintained. Cost constraints on new systems dictate much more quantitative design and analysis procedures than in the past ([McDowell, 2010](#)).

Having in mind the challenges and constraints as stated in the foregoing, it becomes clear that to meet these, an improvement in the control over the behaviour of materials within production operations is very important. The most effective means of control would be the ability to accurately determine the cumulative response of these materials to the chain of processes and operations to which they are subjected. This control has come to be known as *modelling* and *simulation* of material behaviour.

Extensive development of models and their simulation using finite element analysis has become the main tool of control. Most industrial applied models have been developed via the continuum mechanics description of material behaviour which limits analysis to certain properties of materials, and the process conditions which affect material response, with only limited inclusion of the underlying mechanism via which these materials respond.

The modelling route employed in this work considers all these together i.e. multiscale modelling. This lends support to its ability to directly inform the alloy development cycle for better materials development.

1.2: Objectives

The objective of this thesis is to apply the microstructural constitutive model for visco-plasticity developed by ([Amir & Prahl, 2019](#); [Motaman et al., 2019](#)) in studying, via the uniaxial tension test, the plastic behaviour of a single phase S700 sheet steel, at strain rates range of $10^{-4}/s$ to $10^{-1}/s$, in the temperature range of $25^{\circ}\text{C} - 500^{\circ}\text{C}$.

1.3: Scope of this Work

To successfully achieve our objectives, the following experimental and numerical procedures are applied:

- Preparation of rolled sheets into microstructural samples and sheet tensile specimen via cutting, surface milling and polishing.
- Microstructural investigations via electron back scattered diffraction, *EBSD*.
- Tensile tests across strain rates and temperatures.
- Data processing to obtain optimized constitutive parameters.
- Simulation of tensile tests via Abaqus user subroutine tool.

Chapter 2: Overview on Metal Plasticity

2.1: Plastic Deformation and Process Conditions.

Metal plasticity may be defined at two levels;

1. Macroscopically, it refers to the ability with which materials are deformed and shaped under the action of controlled or arbitrary loads.
2. Microscopically or fundamentally, it refers to the nucleation and migration of dislocations in crystals and polycrystals as the underlying basis for microstructure rearrangement or evolution during plastic flow ([McDowell, 2010](#)).

This property is desirable because it determines, to some extent, the potential for materials' successful application as structural components, or successful shaping into desirable products under complex forming operations.

Considerable effort has and is still being devoted to the investigation of materials response under deformation through experiments, theory/modelling, and simulations.

Particularly, metallic materials such as steels, aluminium alloys and other non-ferrous based alloys which find applications in virtually all fields of industry such as aeronautics, automotive, engineering structure, power generation, marine, civil and military, have been studied widely because of their strength and ductility, and their ability to undergo substantial deformation at low and high homologous temperature. These materials are required to withstand wide range of strains, strain rates, and temperature while maintaining reliability in structural and/or geometric integrity. The interest range of load spans low loading conditions (quasi-static or static conditions) to ballistic impacts or blast loads (dynamic conditions) as shown in figure 2.1.

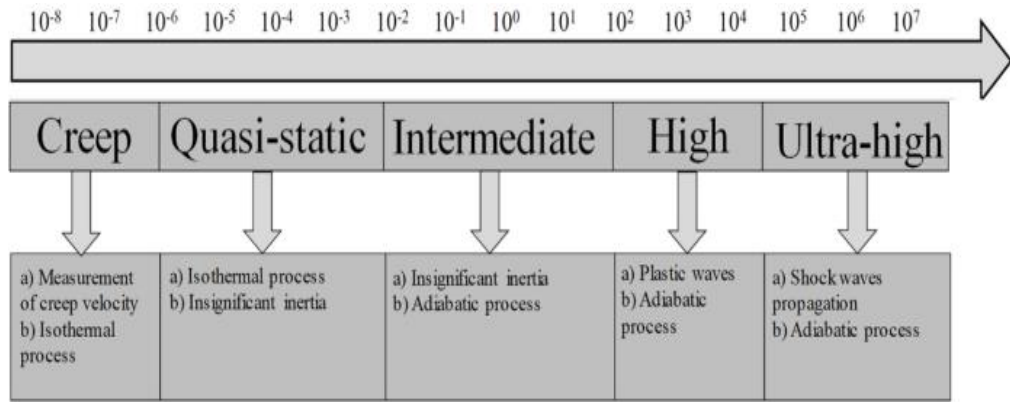


Figure 2.1: Regime of strain rate/loading rate ([Prusty & Banerjee, 2020](#)).

Figure 2.2 below gives an overview of the loading process, loading rate and loading extent of interest. The deformation also spans a wide range as may be seen in such processes as high pressure torsion, wire drawing etc.

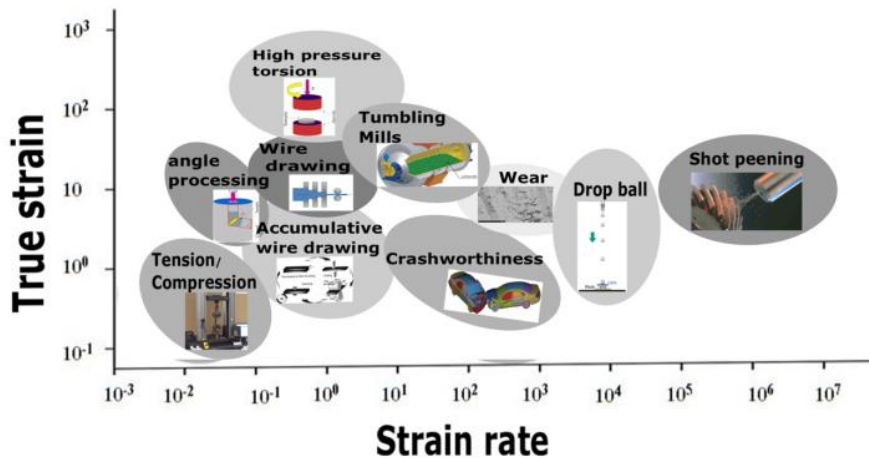


Figure 2.2: Deformation process extent and rate ([Prusty & Banerjee, 2020](#)).

Through a large number of experiments, it has been established that materials deform in different manner when subjected to static or dynamic loading. This response has been shown to depend on the nature and type of loading, the effect of temperature, and the loading rate/strain rate.

The problem of plasticity has also been shown to span a wide range of length scales as shown in Figure 2.3.

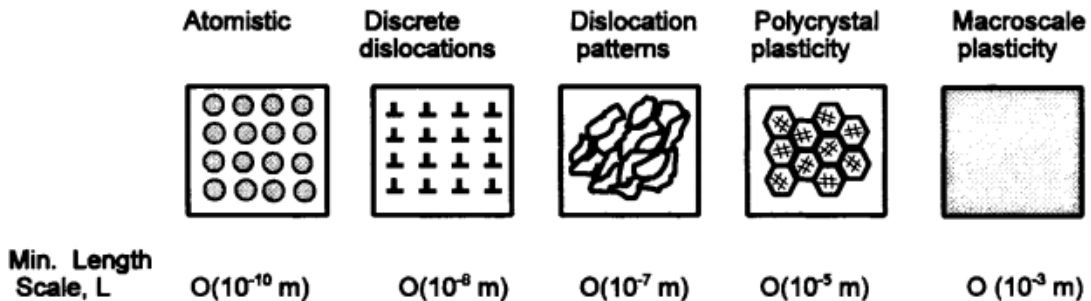


Figure 2.3: Resolution for plasticity including the typical minimum explicit length scale of resolution at each scale ([McDowell 2000](#)).

Observed at different length scale, one sees the movement from dynamics of particle system (atomistics) to dynamics of dislocation line segments (discrete dislocations) to self-organized patterns of dislocations (substructure) to heterogeneous flow within sets of crystals (crystal/polycrystal plasticity) to collective effects at hundreds of microns and above (macroscopic theory of plasticity). A right to left progression of theories (top-down approach) has been the experience in the field.

Early studies on foundational concepts of plasticity were developed to model the observation of yielding and plastic flow in metals based on distortion energy and maximum shear criteria i.e. Von-Mises and Tresca's criterion. Later and current studies describes plasticity in terms of the mechanics of defects, particularly dislocations across a wide range of length scales.

The transformation in the description of plasticity has been facilitated by two very important developments. These are ([McDowell 2000](#)):

1. Development of high resolution characterization tools for measuring microstructures directly related to plastic flow.
2. Development of computational modelling and simulation tools at broad range of length scales for plastic deformation.

Although many length scale appropriate conceptualizations have been developed e.g. gradient and nonlocal theories, statistical micromechanics, crystal plasticity etc.,

completeness remains far in sight especially because of the multiscale nature of plasticity which imparts a huge amount of degree-of-freedom to the problem of plasticity. The non-equilibrium and non-unique nature of the resulting substructures which evolves as plastic deformation also further complicates attempts at assessment. Models at given hierarchies are quite different in fundamental ways and the number of degrees-of-freedom associated with description at each scale decreases for the same volume of material from left to right. Reduced order models are sought for increasing scale of application to mitigate the intense nature of computation as well as to eliminate difficulties arising from prescription of initial conditions and boundary conditions at smaller length scales. Such reduced order models are obtained by averaging or homogenization schemes for fine details of substructures. Information necessarily for calibration of model parameters can flow from bottom to up, and up to bottom i.e. hierarchical multiscale models, or both ways i.e. concurrent multiscale models.

Plasticity at atomic scale is a nonlocal dynamics problem which involves contributions from long range nature of interaction forces between a large ensemble of atoms, and clusters of multiple phases. Descriptions here are subject to very short time scales, and are based on the theories of quantum mechanics or various approximations found in molecular dynamics. Continuum plasticity on the other end cuts off nonlocal action to facilitate a local treatment, and relies on the macroscopic and thermodynamic treatments of plastic deformation. Length scales within these extrema take on appropriate approximations which reflects the degree of nonlocal and/or local action considerations.

Continuum dislocation theory of plasticity attempts to rationalize the kinematics and anisotropy of crystalline slip, the principle of maximum plastic dissipation, the effects of loading path, the development and effects of heterogeneous dislocation substructures, and the developments and effects of micro- and macro- texture, into

self-consistent models of small and large strain plasticity. These basic theory of local nature expressed at the macroscale enables estimation of required forces and plastic flow in important technological applications such as stamping, drawing, rolling, forging, extrusion, impact, high speed machining of metals, collapse of structures, indentation, elastic–plastic fracture and fatigue at notches.

In conclusion, it is recognized that the quantification of plasticity at microstructure scales involves rigorous multi-physics and multi-mechanism linkage of various length scales' unit process models and interactions, and is key to next generation deformation and failure models with more predictive capabilities to guide and exploit material design of targeted properties.

The compelling reasons to develop multiscale models of plasticity include are ([McDowell, 2000, 2010](#));

1. Support design of microstructures with truly tailored deformation behaviour.
2. Facilitate accelerated application of process route to material processing.
3. More accurate prognosis of failure of material.
4. Accurate quantification of complicating contributions of material processing induced variability in material properties.
5. Development of self-consistent theories for bridging domains.

The main requirement of deformation problems such as structural components design, life prediction, high-speed machining, impact, and various primarily metal forming, is to develop constitutive relations which are widely applicable and capable of accounting for complex paths of deformation. Achieving such desirable goals for metallic homogeneous materials and alloys involves a comprehensive study of their microstructures and experimental observations under different loading conditions.

2.2: Characterization of Plastic Deformation

2.2.1: Mechanical Characterization

In bulk material deformation or finite strain plasticity, the mechanical curve obtained from a plot of stress and strain or force and elongation results from a simple uniaxial tension, compression, shear or torsion tests on standard test pieces is used to characterize plasticity. These tests are performed such that the force of deformation is applied in a way to keep loading rate or the strain rate constant throughout the testing. Analysis of the forms of the stress versus strain curve classify bulk materials into brittle, e.g. concrete, glass etc., or ductile, e.g. most metals. This classification depends on the extent of strain which can be achieved before the fracture of the material occur, where very little or appreciable strain is achieved for brittle and ductile materials respectively. Metals show varying characters of ductile plasticity which depends on the underlying mechanism (intrinsic material property) via which plastic deformation is achieved or the conditions under which plastic deformation is applied.

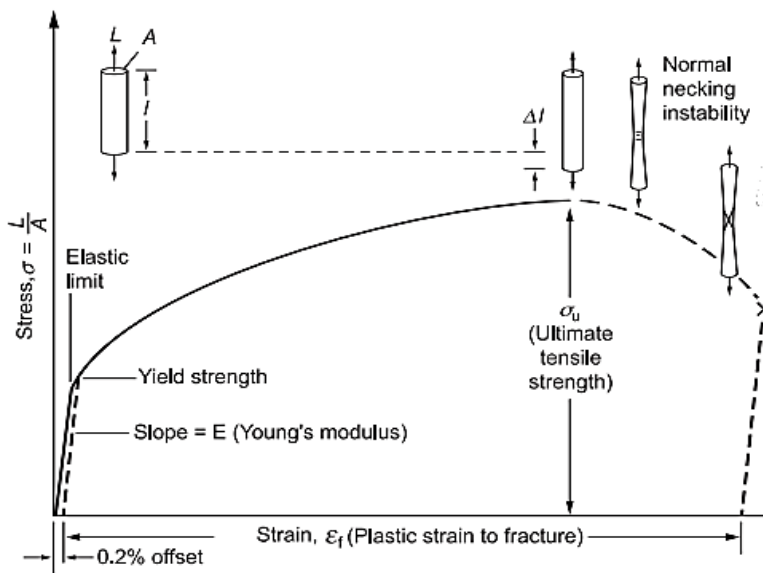


Figure 2.4: The Tensile Stress-Strain Curve (Gray et al., 2005).

The mechanical curve is divided into 2 parts; the elastic region and the plastic region. The strain obtained in the elastic region called the elastic strain is recoverable after the stress is removed i.e. no permanent change to the test piece's geometry is observed. In

contrast to this, the strain achieved in the plastic part contains both a recoverable part, and the non-recoverable part, the plastic strain, for which permanent change in the sample's geometry is observed.

The important features of the mechanical curve are ([Gottstein, 2004](#)):

- The Young's modulus, E , which is obtained as the gradient of the stress versus strain curve within the elastic region is an expression of the Hooke's law.
- The Yield Strength or Stress, σ_y which is the stress at which non-recoverable strain begins to develop. In practice, the yield stress is obtained at the intersection point of a straight line drawn with a gradient of the Young's modulus at 0.2% strain and the mechanical curve. This is done like so to handle the non-clear distinction between micro-yield and macro-yield phenomenon.
- The Ultimate Tensile Stress, σ_{uts} which is the maximum stress achievable at uniform deformation.
- The strain, ϵ_{uts} at the ultimate tensile stress.
- The Fracture Stress, σ_f which is the stress at the point of separation/break apart of the material.
- The Area-under-the-Curve, which provides the total energy expended for the deformation. This is an indicator of the toughness of a material i.e. the material's response under loading when a crack or void is present in the material.

Two forms of the mechanical curve are normally utilized depending on how the stress and strain are calculated, these are the engineering stress vs. strain and true stress versus strain curve. Each curve may be obtained from the other by simple transformation equations ([Gottstein, 2004](#)).

Other forms of mechanical characterization for plasticity are industrial formability tests for sheet metals such as the plane-strain tension test (results in the forming limit

diagram), balanced biaxial/in-plane stretching test e.g. bulge test (Wagoner & Chenot, 2001) etc.

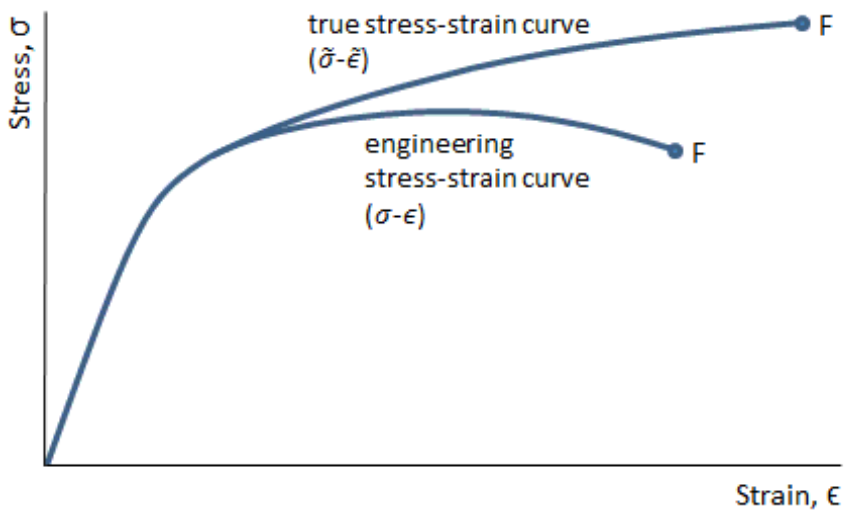


Figure 2.5: The true and engineering stress-strain curve (Mechanical Properties of Materials | MechaniCalc, n.d.)

2.2.2: Microstructural Characterization

Plasticity has also and is being studied and characterized microstructurally using microscopy and X-ray techniques to inform on the evolution of dislocation structures as plasticity progresses. Important information about such features which facilitates plasticity and its modelling such as dislocation densities, configuration, and substructures of different dislocation features, slip systems, grain/phase boundaries' densities and properties i.e. orientation, shape and size distributions etc. may be obtained.

Typical generic microstructural features of the deformed state which have been identified depending on the degree of deformation are, as shown in figure (Gottstein, 2004; Humphreys & Hatherly, 2004; Li et al., 2004; Rittel et al., 2012);

- **Cells/Subgrains:** these are features found within the grains. They result from entanglement and clustering of the dislocations formed as plastic deformation progresses. This entanglement and clustering of dislocation leads to the formation

of low angle boundaries called incidental dislocation boundaries. Within these boundaries the dislocation density is reduced.

- **Cell blocks and cell bands:** these features are a congregation of cells in which slip activity is similar but differs between blocks. They are bounded by aligned geometrically necessary boundaries called dense dislocation walls, *DDWs*, or micro-bands.

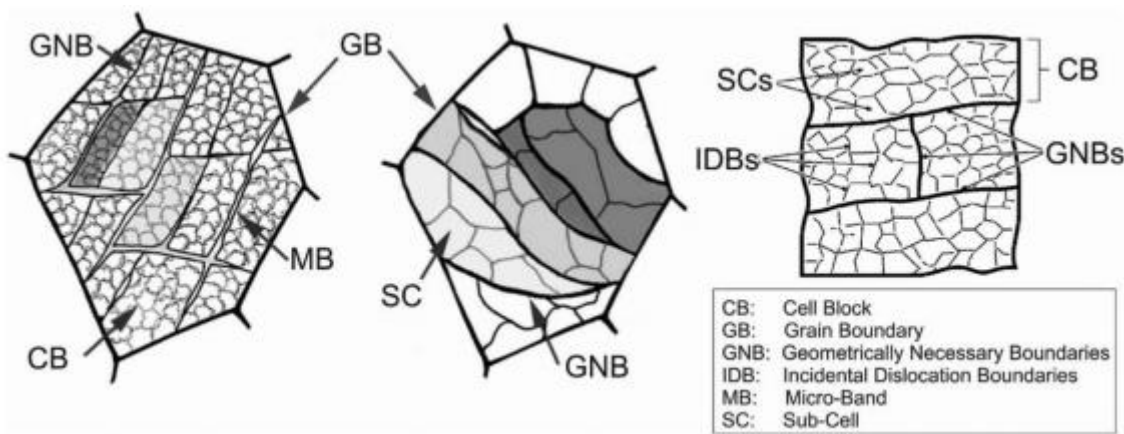


Figure 2.6: Schematic of grain microstructural subdivision during plastic deformation ([Amir & Prahla, 2019](#)).

- **Micro-shear bands:** are thin features of intense shear within grains.
- **Deformation and/or transition bands:** are regions of different slip activity within a grain which is formed from the subdivision of the grain into regions different orientations. This subdivision results from inhomogeneous stresses on the grain or instability of the grain. The grain size and grain orientation determine a grain's susceptibility to forming deformation bands.
- **Shear bands:** are macroscopic narrow features of intense shear on planes inclined to the rolling plane. They are non-crystallographic and typical extends across several grains. These features form in rolled materials at 35° to the rolling plane. Grain size and orientation, solutes, and deformation temperature are the influencing factors for the formation of shear bands.

Metals of low and medium stacking fault energy show twins in the deformed microstructure, while metals of high stacking fault energy show microbands. The deformed microstructural feature which appears during deformation is determined by the degree of macroscopic strain applied to the metal ([Humphreys & Hatherly, 2004](#)).

Chapter 3: Hardening

3.1: Classical Rate-Independent Hardening

As may be observed from the mechanical curve, after a metal yields and plastic strain starts to develop, increasingly higher stress is needed to continue plastic deformation i.e. the yield stress takes on different values as loading continues. This phenomena is described as strain or work hardening.

The hardening behaviour of materials is characterized by the stress-strain curve for proportional loading i.e. loading in which the components of the stress tensor increase proportionally ([de Jong, 1983](#)).

Early continuum mechanics studies described hardening in materials with rate-independent macroscopic models, utilizing the Clausius-Duhem inequality derived from a thermodynamically consistent consideration of plasticity, and the yield function or criterion, to characterize plasticity ([De Rosa et al., 2013; Simo, 1998](#)). The yield function is formulated in terms of the components of the stress tensor applied (more precisely, the deviatoric part of the stress tensor), the yield stress of the material in simple uniaxial deformation expressed in terms of the evolving plastic strain, ε_{pl} or some internal variable (G. Dieter).

$$F(\sigma_{11}, \sigma_{22}, \sigma_{33}, \sigma_{12}, \sigma_{13}, \sigma_{23}) = K(\varepsilon_{pl}) \quad \text{Equation 3.1}$$

Here, F is some function of the 6 independent components of the stress tensor, and K is some material property which can be determined experimentally e.g. the yield stress. The yield function is typically plotted in a 2D or 3D stress space depending on the loading conditions i.e. either biaxial or triaxial load or stress state.

The state of the material is described based on the Karush-Kuhn-Tucker complementary and consistency conditions ([Simo, 1998](#)) as being elastic when either the yield function is evaluated as less than zero in a loading state (within the stress

space) or evaluated as zero in an unloading state, and plastic when the function is evaluated as zero in a loading state (on the stress space surface). The evaluation of the yield function as greater than zero is non-admissible.

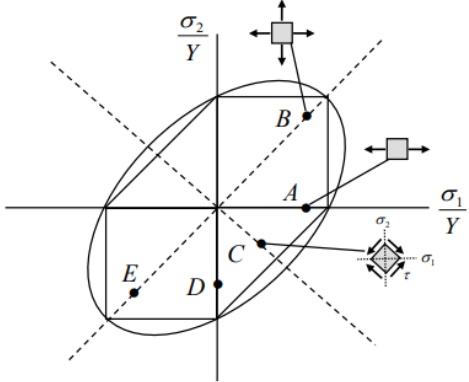


Figure 3.1: Yield loci in 2D principal stress space ([Dieter, 2011](#)).

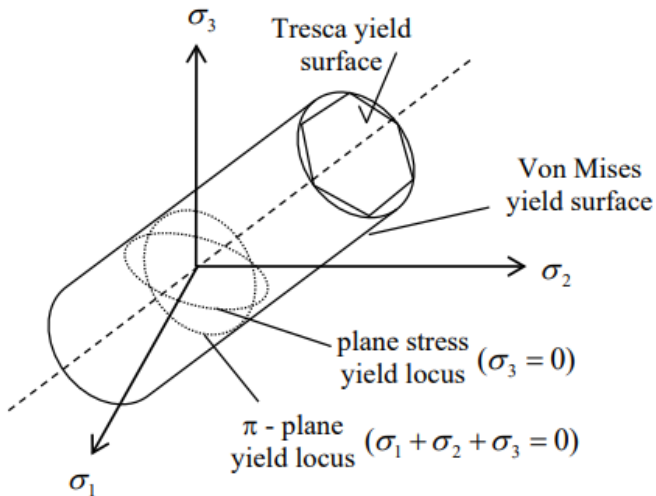


Figure 3.2: The Von Mises and Tresca yield surfaces in 3D space ([Dieter, 2011](#)).

The Von-Mises, Tresca and Maximum shear stress criteria are some of the yield criterions in use for ductile pressure insensitive yielding materials while the Drucker-Prager and Mohr-Coulombs criteria are applied for pressure sensitive yielding materials.

The associated flow rule which results from these complementary and consistency conditions is given as ([De Rosa et al., 2013; Simo, 1998](#));

$$\dot{\varepsilon}_{pl} = \dot{g}(\dot{\sigma}) = \dot{\lambda} \frac{\partial f}{\partial \sigma} \quad \text{Equation 3.2}$$

where $\dot{\varepsilon}_{pl}$, $\dot{\sigma}$, $\dot{\lambda}$, and f are the plastic strain rate, the stress rate, the plastic multiplier and the yield function respectively. The plastic multiplier is determined from the solution of the consistency condition;

$$\dot{f} = 0 \quad \text{Equation 3.3}$$

The nature of hardening is very important for consideration of the cyclic and reversed plastic deformation conditions, and has led to a classification of basic hardening as isotropic, kinematic, rotation, and distortion ([Xiao & Chen, 2009](#));

- Isotropic hardening: refers to the isotropic expansion or contraction of the initial yield surface in the stress space without a change in shape and position of the stress space. It is represented as a scalar variable addition to the initial yield stress part of the yield function.
- Kinematic hardening: refers to the shift of the yield surface without change in shape or size of the yield stress space. It is represented as a tensor variable subtraction to the applied stress part of the yield function. Linear, double yield surface, multiple yield surface, and non-linear kinematic hardening are specific types used to approximate the shape of the mechanical stress-strain curve.
- Rotation Hardening: refers to hardening where the direction of the yield function is rotated, howbeit without shape change.

Further classifications are typically a combination of these basic types.

Obviously, the isotropic hardening is unable to handle anisotropy in the yield behaviour of material as it assumes isotropy of yielding for which experimental measurements of single crystals show that anisotropy is most likely the observed

yielding behaviour of materials ([Ledbetter & Reed, 1973](#)). Also, the phenomena of the Bauschinger effect (decrease in the yield stress in the reverse strain path) evident in the reversal of strain is unable to be accounted ([Kassner et al., 2013; Mughrabi, 1983](#)). Complicated loading conditions such as cyclic loading are also unable to be properly described by the isotropic hardening model. These incapacities are typically addressed by the kinematic hardening model although not completely since the kinematic model underestimates the amount of work hardening with continued reversed loading. A combined hardening model of the isotropic and kinematic kind yields much better and satisfactory results for reversed loading howbeit not for cyclic loading conditions. Other models developed include distortional hardening, fraction model and extensions of the kinematic hardening model, these models incorporate effects of such phenomena as anisotropy and the Bauschinger effects. In many of these models, the yield surface changes in size and/or in stress space. Due to large strain effects, the stress-strain response depends strongly on the type of hardening law.

3.2: The Mechanism of Deformation and Strain/Work Hardening

X-ray diffraction investigation on single crystals of metals show that most metals possess a crystalline structure i.e. the constituting atoms are arranged in a periodic fashion. Three types of crystalline structure for most metals have been identified, these are; body-centred cubic, *BCC*, face-centred cubic, *FCC*, and hexagonal closed packed, *HCP* ([Gottstein, 2004](#)).

Bulk metals comprise a huge amount of single crystal-like units called grains. In this state they are polycrystalline. Under applied stress, the mechanisms for plastic deformation within and across these grains which are dependent on the stacking fault energy of the metal are shown from experiments to be mainly slip, twinning, grain-boundary sliding, diffusional creep, and displacive phase transformation ([Abbaschian](#)

et al., 2009; Gottstein, 2004; Humphreys & Hatherly, 2004). While slip occurs at both low and high temperatures, twinning mostly at low temperatures and/or high strain rate deformation, grain-boundary sliding and diffusional creep occurs only at elevated temperature (Abbaschian et al., 2009).

Since the work of Orowan and Polyani in developing the idea of line defects called dislocation whose behaviour facilitates the response of metals to deformation, the mechanisms for plastic deformation has been recognised and experimentally verified, using different methods of metallography and electron microscope, to be facilitated by the movement these line defects (slip) at low and medium temperatures, additionally by the interaction of dislocations and point defects/vacancies at high temperatures (Abbaschian et al., 2009; Gottstein, 2004).

Inelastic deformation of metals at temperatures less than about 40% to 50% of the melting point is governed primarily by the generation and crystallographic glide of dislocations i.e. deformation by slip (McDowell, 2000).

Slip deformation occurs by the movement/glide of dislocations on specific crystal planes called the slip planes, and in specific crystal directions on these planes, called the slip directions. These dislocations may be of the screw, edge or mixed type configuration. The slip planes and slip directions together form the slip system.

For most metals, the slip planes and directions are the planes and direction of highest atomic density. The slip system is determined by the type of crystallinity.

For the face-centered-cubic, *FCC*, structure, it is the $\{111\} \langle 101 \rangle$, for the body-centered-cubic, *BCC*, structure, it is the $\{110\} \langle 111 \rangle$, $\{112\} \langle 111 \rangle$, $\{123\} \langle 111 \rangle$ (collectively called pencil glide, also the *BCC* structure actually has no densely-packed lattice plane), and for the hexagonal-closed-packed, *HCP*, structure, it is $\{0001\} \langle 1120 \rangle$, $\{1010\} \langle 1120 \rangle$, and $\{1011\} \langle 1120 \rangle$ (Abbaschian et al., 2009; Gottstein, 2004;

Humphreys & Hatherly, 2004). The cumulative effect of glide of dislocations results in the macroscopic observable plastic strain or deformation.

The dislocation density in well annealed crystal i.e. crystals heated for a long time at temperatures close to their melting point, is usually about 10^{10} per meter square (Hull, 1975). Thermodynamically, the lowest energy state of a material would be one where all dislocations are eliminated, however such elimination process is not spontaneous at low temperature only at high temperature and with decreasing driving force as the density of dislocation reduces such that at densities within the range stated above for annealed materials, the driving force is so low that such state can be assumed to be in metastable equilibrium. These dislocations distribute themselves in the crystals on the slip planes where they can be identified as forest and/or parallel dislocations (Ma et al., 2007).

During plastic deformation of metals, the grains of polycrystalline metals change their shape in a manner that corresponds with the macroscopic shape change. Some of the deformation energy (howbeit a relatively small amount) is stored in the metals via the accumulation of point defects and dislocations, and an increase in dislocation/grain-boundary area i.e. creation of new dislocation/grain boundary (Humphreys & Hatherly, 2004). The increase in these defects particularly dislocations and dislocation boundary area also leads to an increase in the energy state of the metal. Continual increase in the dislocation density with deformation results in the development of characteristic microstructural features consequent on the trapping and clustering of dislocations. The slip processes and its variations within and between grains largely determine the deformation's microstructural features.

Several important dislocation processes which lead to initial homogenous and progressively heterogeneous dislocation substructures, and which facilitate and

determine the nature of work hardening behaviour of materials have been extensively documented. Such processes are ([Hull, 1975](#); [Nabarro et al., 1964](#));

1. Mobile dislocation generation by Frank-Read sources, multiple cross glide mechanism, prismatic loops mechanism, and Bardeen-Herring source.
2. Dislocation dissociation into Shockley and Frank partials forming extended dislocation depending on the stacking fault of the material.
3. Dislocation intersections which results in the formation of glissile or sessile jogs, and the formation of vacancy loops as these jogs travel along with the dislocations.
4. Dislocation reactions leading to the formation of attractive or repulsive junctions, Lomer-Cottrell locks, Hirth locks.

These processes occur as deformation progresses with the transformation of the annealed homogeneous distribution of dislocation into progressively heterogeneous structures depending on the process conditions and material parameters (stacking fault energy and solid solution content) ([Darcy A. Hughes et al., 2003](#)). Structures which have been identified via electron microscopy at low strain include ([Darcy A. Hughes et al., 2003](#); [Kuhlmann-Wilsdorf, 1999](#)); Taylor lattice, dislocation dipoles and multipoles, dipolar mats, dipole walls, dislocation prismatic loops, parallel dislocation walls, pile-ups, tangles, clusters, cell walls or incidental dislocation boundaries, IDBs (low angle boundaries). These are arrangements which do not give rise to significant rotation of the lattice, that is, they exhibit practically a net burgers vector of zero.

With larger strain, a progression into extensive appearance of dislocation feature i.e. geometrical necessary dislocations and boundaries, *GNDs*, which accommodate relatively large misorientation across strain gradient regions and the reorientation of the lattice, ensuring continued congruency and contiguity (difference in operating slip system or difference in partitioning of slip activity on the same slip systems), are

observed. Storage of *GNDs* can be a uniform distribution of dislocations or into boundaries. *GNBs* can develop into high angle boundaries equivalent to original grain boundaries (D. A. Hughes & Hansen, 2018; Darcy A. Hughes et al., 2003; Li et al., 2004). Density of non-redundant dislocation in *GNBs* is greater than that for redundant density. The redundant dislocations are arranged in dipolar and multipolar structures so their net burgers vector is zero while the non-redundant are so arranged to accommodate misorientation.

Identification of *IDBs* and *GNBs* are based on their different scaling behaviours and rate of increase in average misorientation angle across the boundaries with increasing strain, also, both entities show similitude with deformation (Gil Sevillano & Aernoudt, 1987; D. A. Hughes & Hansen, 2018; Darcy A. Hughes et al., 2003; Kuhlmann-Wilsdorf, 1999). Four parameters of the *IDBs* and *GNBs* i.e. average distribution of their respective boundary spacing, D^{IDB} and D^{GNB} , and the average distribution of the boundary misorientation angles, θ^{IDB} and θ^{GNB} , may be used to describe transition in hardening behaviour during work hardening since these parameters evolve with strain (parameters of *GNBs* evolve with strain much faster than those of *IDBs*) i.e. structural morphology and crystal orientation/textures. Ultimately, these parameters determine the interaction of these substructures with glide dislocations (glide dislocations pass through, bow out from, or are stored in *IDBs* while *GNBs* typically acts like original grain boundaries to glide dislocations), as well as correlate with the dislocation densities of these substructures, and together, consequently determine the flow stress of materials (D. A. Hughes & Hansen, 2018; Darcy A. Hughes et al., 2003; Li et al., 2004).

Other important structures at high deformation have already been mentioned in the foregoing sub-chapter on microstructural characterization of plasticity.

Two theories exist to explain the formation of these structures; the low energy dislocation structure, *LEDS*, model by (Kuhlmann-Wilsdorf, 1999; Kuhlmann-Wilsdorf, 1987) considers these structures to result from a driving force of energy minimization i.e. dislocations in these structures are spatially arranged such that the stress from them are screened to local influence (no long range stress), are not above the material internal resistance, alternating between areas with high and low dislocation densities, and also that a principle of similitude applies to the change in substructure. Studies published by (Mughrabi, 1987) where it is shown that heterogeneous structures are energetically favourable somewhat gives credence to this *LEDS* model. Other studies postulate a ‘kinetic’ statistical model of substructure formation which depends on the (random) distribution of forest dislocation and the formation of irregular self-organized cellular double-walled structures due to the looping around of these forest dislocation (hard obstacles) by the mobile dislocation in the course of deformation (Cottrell, 2002; Gil Sevillano & Aernoudt, 1987; Malygin, 1999). The statistical model only acknowledges metastable energy minimization at a local short range events i.e. within individual structures. Double-walled checker patterns of deformation structures which possess long range internal stresses observed by *TEM* studies, pile-ups and redundant dislocations support this model.

Traditionally, work hardening investigation divides the process into 3 stages, further experiments reveal 2 extra stages with distinct characteristics. The stages are summarized as thus (Cottrell, 2002; Gottstein, 2004; D. A. Hughes & Hansen, 2018; Kuhlmann-Wilsdorf, 1989, 1999; Mecking & Kocks, 1981; Rollett & Kocks, 1993; Zehetbauer & Seumer, 1993);

- **Stage I:** Easy glide stage where the hardening rate is quite small. Early stages of deformation tends to confine dislocation to single set of parallel slip planes (single slip in single crystals) where the resolved shear stress has exceeded the

critical resolved shear stress, τ_{crss} . This early stage of deformation occur with rapid multiplication of dislocation resulting in the formation of dislocation structures such as dipoles, dipolar mats, tilt/dipolar walls, and Taylor lattice. The low work hardening rate is consequent on the accumulation of dislocation debris.

- **Stage II:** is an athermal linear hardening stage which occurs in both single and polycrystals, with high hardening rate, constant strain rate sensitivity and activation enthalpy. Change of orientation of slip planes as deformation continues results in double/multi- slip condition i.e. multiple activation of dislocations on the primary (highest resolved stress) and secondary slip system (conjugate, cross-slip and critical slip systems). This condition occurs with the interaction of dislocations on the primary and secondary slip planes where intersection and/or reaction of the dislocation and dislocation segments introduces products like glissile or sessile jogs, dislocation partials, Lomer-Cottrell and Hirth Locks, vacancy loops (at high temperatures) and other dislocation debris e.g. dislocation prismatic loops, dislocation dipoles, consequently statistical storage of dislocations (dislocation trapping and accumulation). Its extent of occurrence decreases with increasing temperature and stacking fault.
- **Stage III:** this is the stage more generally observed as the stress vs. strain behaviour for most ductile material at room temperature and above. It corresponds to steady decrease of work hardening rate (dynamic recovery process facilitated by extensive cross-slip of dislocations causing softening, i.e. screw dislocation controlled) which is sensitive to temperature and strain rate. Extensive forest-cutting or jog formation is necessary for extensive cross slip.

The temperature, T, dependence of the stress, σ_{III} , at which this stage starts is modelled as

$$\log \sigma_{III} = a - bT \quad \text{Equation 3.4}$$

where a, b are material specific constants.

The strain hardening in this stage is calculated by considering the dislocation storage in stage II to continue and adding to it, the term for thermal activated dynamic recovery rate. The falling hardening rate implies an ever increasing dynamic recovery rate i.e. the rate of dislocation density change is proportional to the density of dislocation. At large strains, the stage appears to have an asymptote to a saturation stress determined by the character of the dislocation tangles and debris (due to the imperfect nature of the dynamic recovery process) in the cell walls (the hard spots) i.e. the evolution of the dislocation structure, therefore is dependent on strain rate and temperature (exponential dependence). Studies have shown that saturation is not attained rather the start of stage IV is observed. Cellular structures in stage III incorporates a huge amount of redundant dislocations in their 3D walls and a non-negligible density of near-randomly distributed dislocations in the cell interiors.

- **Stage IV:** this stage is typically obtained in rolling and torsion mode deformation. Classical tensile test is unable to reach such strain degree because of necking. The hardening here is only significant at low homologous temperature and of a small value just as obtained in stage I. Stage IV strain hardening is also observed to have little changes with respect to the strain rate and temperature i.e. constant strain rate sensitivity and activation enthalpy such as in stage II, and its extent to be shortened by temperature. The work hardening rate, θ_{IV} , and stress, σ_{IV} , at which a transition to stage IV is observed

decline with increasing temperature. Both are also observed to bear a mathematical relationship;

$$\theta_{IV} = c\sigma_{IV} \quad \text{Equation 3.5}$$

where **c** is a material constant.

Models to describe hardening in this stage are; extra elastic misfit or back stresses in the structure, extra dislocation storage due to deterministic lattice rotations, irrecoverable dislocation debris models. The latter model is developed by considering the rate of accumulation, and rearrangement in cell walls, of dislocation monopoles in tangles and cell walls, and dislocation debris such as dipoles and loops resulting from the continued thermal activated dynamic recovery. A constancy in cell size or a markedly reduced cell shrinking rate is observed in this stage.

- **Stage V:** the features in stage V are analogous to those of stage III i.e. increase of strain rate sensitivity and decrease of activation enthalpy. Thermal activated dislocation annihilation of built up dislocation debris in stage IV via climb facilitated by consumption of the saturated density of deformation induced vacancies (edge dislocation controlled). A decrease in growth rate of total density down to zero (approach of constant dislocation density) and a transformation from cell walls to sub-grain boundaries are observed.

At $0.5T_m$, where T_m is the melting temperature, a switch of the underlying mechanism between stage III and stage V is observed.

The difference in the stages of work hardening is not distinctively obtained from a correlation of the dislocation density but from a correlation of the type of obstacles (stage I to stage II) or the dislocation processes (stage II to stage III) in play.

All expression of the models of work-hardening i.e. long-range internal stress fields (Taylor lattice structure), operation of Frank-Read sources (dislocation bowing), cutting of forest dislocations, jog dragging, and attractive interactions of dislocation, exhibit the dependence on the square root of the density of dislocations ([Nabarro et al., 1964](#)).

Chapter 4: Models of Flow Stress (Rate-Dependent Plasticity)

Generally, the models developed to describe the flow behaviour of materials may be broadly classified as either engineering/empirical/semi-empirical/phenomenological models, or microstructural/physical based material model ([Amir & Prahla, 2019](#); [Domkin, 2005](#)). Engineering/empirical/semi-empirical models are purely mathematical description of the flow properties with no regard or little regard to the underlying process involved in the flow behaviour. Such models are typically explicit formulation of the yield stress based on strain and temperature. These models are expressed with empirical parameters used to fit the model to experimental data.

Experimental data obtained from two types of experiments, jump strain rate or temperature experiments and constant strain rate or temperature experiments, clearly reveal that the value of the flow stress depends on the strain rate, temperature, and strain rate and temperature histories i.e. the flow stress is not a unique value of the strain, strain rate and temperature as proposed by the engineering models ([J. Klepaczko, 1975](#); [J. R. Klepaczko & Chiem, 1986](#)).

Microstructural/physical based material model are models which consider the underlying dislocation process which determine the flow behaviour. In these models combination of the constitutive equations of single unit dislocation processes is the paradigm utilized, therefore, the capability of these models depend on accurate description of these unit processes.

Each class of model possess its advantages and drawbacks. For example, the fitting parameters of empirical models are few, easy to obtain and apply, and can accurately describe flow properties up to intermediate strains and temperatures, however, are unable to describe strain rate and temperature history dependent effects such as interrupted deformation and strain path changing deformation, or make any

prediction of flow properties outside the range of fitting. The physical based models on the other hand can very accurately describe or predict flow behaviour up to large strains, and wide strain rates and temperature range, account (to a good extent) history dependent behaviour. These models unfortunately require a large amount of experimental data set from precisely controlled experiments to obtain the substantial number of material parameters, are still limited in describing non-monotonic deformation conditions such as cyclic deformation, and require high computational efforts.

4.1: Engineering/Empirical/Semi-Empirical/Phenomenological Models

A huge amount of developed empirical models exist in literature and a few will be presented here without any discourse on the underlying principle of their development or how they compare amongst themselves. The models in this category are further divided into quasistatic and dynamic strain rate range classification, where quasistatic models only consider strain as variables while dynamic models are built on a quasistatic reference flow curve but incorporating dynamic effects in an additive or multiplicative manner i.e. consider strain, strain rate and temperature effects. Examples of quasi-static models are ([Paul, 2012](#); [Tang et al., 2020](#)); Hollomon, Ludwik, Swift, Voce, Hockett/Sherby, Gosh, Swift-Voce, Swift-Hockett/Sherby, El-Magd, Voce generalized, and Bergstrom models etc.

Table 4.1: Equations of Quasistatic Models.

Model	Equation
Hollomon	$\sigma(\varepsilon) = C_1 \cdot \varepsilon^{C_2}$
Ludwik	$\sigma(\varepsilon) = C_1 + C_2 \cdot \varepsilon^{C_3}$
Swift	$\sigma(\varepsilon) = C_1 \cdot (C_2 + \varepsilon)^{C_3}$
Voce	$\sigma(\varepsilon) = C_1 + (C_2 - C_1) \cdot \exp(-C_3 \cdot \varepsilon)$
Hockett/Sherby	$\sigma(\varepsilon) = C_2 - (C_2 - C_1) \cdot \exp(-C_3 \cdot \varepsilon^{C_4})$

Gosh	$\sigma(\varepsilon) = C_1 + C_2 \cdot (C_3 + \varepsilon)^{C_4}$
Swift-Voce	$\sigma(\varepsilon) = C_1 \cdot \sigma_{Swift}(\varepsilon) + (1 - C_2) \cdot \sigma_{Voce}(\varepsilon)$
Swift-Hockett/Sherby	$\sigma(\varepsilon) = C_1 \cdot (C_2 + \varepsilon)^{C_3} + C_4 \cdot \exp(-C_5 \cdot \varepsilon^{C_6})$
El-Magd	$\sigma(\varepsilon) = C_1 + C_2 \cdot \varepsilon + C_3 \cdot [1 - \exp(-C_4 \cdot \varepsilon)]$
Voce generalized	$\sigma(\varepsilon) = C_1 + (C_2 + C_3 \cdot \varepsilon) \cdot [1 - \exp(-C_4 \cdot \varepsilon)]$
Bergstrom	$\sigma(\varepsilon) = C_1 + C_2 \cdot [C_3 \cdot (C_4 + \varepsilon) + \{1 - \exp[-C_5 \cdot (C_4 + \varepsilon)]\}^{C_6}]$

The C-constants represent the fitting parameters of these models. The parameters are strongly dependent on the strain range for fitting. The models are able to predict experimental data accurately at tensile test range of uniform elongation. Extrapolation of results to higher strains results in different prediction for different models.

Examples of dynamic models are (Holmquist & Johnson, 1991; Huh et al., 2014; Khan & Liang, 1999; Liang & Khan, 1999; Paul, 2012; Salvado et al., 2017; Zerilli, 2004); Johnson-Cook, Zerilli-Armstrong, Khan-Huang, Preston-Tonks-Wallace, Modified Johnson-Cook, Modified Khan-Huang, Cowper-Symonds, El-Magd-Swift, El-Magd modified, Tanimura-Ludwik, Tanimura-Hockett/Sherby, Rusinek-Klepaczko, Parameter ‘BMW’, Corus, Molinari-Ravichandran, Lin-Wagoner, Zhao, Bodner-Partom etc. These models differ based on their validity domain. The complexity of a model depends on the validity range, where higher complexity corresponds to larger validity range of strain, strain rate and temperature. Their accuracy can be determined by their strain rate sensitivity and strain hardening behaviour.

4.2: Microstructural/Physical Based Material Model

Models under this category may be explicitly or implicitly formulated, which is determined by how the constitutive equations are setup. In explicit formulation, each process has a representative equation with its constitutive parameters while in implicit formulation, a grouping of similar processes under appropriate constitutive equation with a parameter to represent all the parameters of the constituting process is the

paradigm. Physical based models are usually derived from 3 approaches which represent the scale of interest. These are ([Amir & Prahl, 2019](#); [Domkin, 2005](#));

- **Discrete Dislocation Dynamics, DDD:** this approach utilizes the modelling and the simulation, on the basis of atomistic calculations, of the motion and interaction of individual dislocation lines in a huge assembly of dislocations of a very small representative volume element (*RVE*) to obtain the stress-strain response. *DDD* are typical used in problems concerning microplasticity i.e. micro-pillar compression, nano-indentations etc. Algorithms based on *DDD* are extremely computational demanding and therefore not readily implementable in standard engineering analysis.
- **Crystal Plasticity:** this approach studies plasticity at the crystal or grain scale. The foundation is based on the work of Asaro and Rice where principles of continuum mechanics is applied to slip mechanics, along with flow and evolutionary equations to describe plastic deformation. The overall polycrystalline properties are determined as an average of the constituent crystal slip behaviour by appropriate averaging procedures. Incorporation of finite element modelling in this approach extends the capability and applicability of the approach in plasticity problems.
- **Continuum Dislocation Mechanics, CDM, or Dislocation Density Based Models:** this approach models microstructure micro-level processes in an average sense with a representative volume element (*RVE*) which scales as an aggregate of grains.

The interest of this work is application of an already developed dislocation property based model.

4.2.1: Flow Stress Model Based on Microstructural Dislocation Mechanics

Physically based models of this type consider the mechanics of the mobile dislocations within the microstructure purely on the thermodynamics of rate theory. Foremost in this category of models is the description of flow stress by ([Follansbee & Kocks, 1988](#)) called the Mechanical Threshold Stress, *MTS*, model.

Under the action of stress, the movement of dislocations have been studied and found to be opposed by two main kind of barriers, these are the short and long range barriers ([Follansbee & Kocks, 1988](#); [Voyiadjis & Abed, 2005](#)). The short range barriers are obstacles which have localized and/or periodic effect that requires close contact of dislocations e.g. Pierel's barrier (resulting from the intrinsic lattice resistance), forest dislocations, Cottrell atmospheres etc. The importance of these barrier types depends on the crystal structure i.e. while all three barriers are important for the *BCC* structure, forest dislocation is of main importance for the *FCC* structure. The influence of the long range barrier on the other hand depends on distance between the barrier and the dislocations. Such barriers are for example long range internal or back stress (connected to the Bauschinger effect), coherent/semi-coherent grain boundaries, pile-ups at grain boundaries etc. ([Follansbee & Kocks, 1988](#); [Kassner et al., 2013](#); [Mughrabi, 1983](#); [Seeger, 2002](#); [Stainier et al., 2002a](#); [Voyiadjis & Abed, 2005](#)).

The nature of the interaction of these barriers with dislocation during glide determine the way of overcoming these barriers. Typically, barriers are overcome via thermal activation i.e. thermally assisted, or athermally i.e. no effect from thermal fluctuation due to thermal energy.

Following this classification, the flow stress is modelled as comprised of two components; a component which is influenced by thermal activation is regarded as the

thermal/viscous/friction stress, while the component which is not affected by thermal activation is referred to as the athermal stress.

4.2.1.1: Flow Stress Component Due to Thermally Overcome Barriers

The formalism in this group of models relies on the averaging of the physical quantities such as dislocation length pinned between obstacles, dislocation glide velocity, free energy of activation to overcome the barrier, the effective stress, and the activation area in developing the constitutive relation ([J. Klepaczko, 1975](#)).

The description for the thermal stress component of the flow stress differ somewhat based on the crystal structure of the material. The dissociation of the core of screw dislocations into low-energy non-planar configurations in the slip system of the *BCC* structure results in a predominance of screw dislocations in the structure unlike the *FCC* structure where no dissociation into non-planar configurations occurs, and therefore no preference for screw dislocation is observed except as regards the mechanism of cross-slip since only screw dislocations can cross-slip. The effect of the foregoing is a high Pierel's barrier i.e. deep Pierel's energy valley in the *BCC* structure ([Seeger, 2002; Stainier et al., 2002b; Yalcinkaya et al., 2008](#)) while for *FCC* structure, the Pierel's energy is rather small (about 0.2 eV), much smaller than the measured critical resolved shear stress, and only of some significance at very low temperature ([Nemat-Nasser & Li, 1998](#)).

Glide of screw dislocation against the periodic Peierl's barrier/ lattice resistance is facilitated by thermal activated motion of kink pairs ([Butt, 2007; Seeger, 2002](#)) as shown in the figure below, whose travel apart results in the transition from one Pierel's valley to the next.

The applied stress, i.e. the viscous/friction stress, works to reduce the energy barrier effect while allowing the dislocation travel overall in the slip plane at a given velocity

which translates to a specific strain rate. The dislocation velocity depends on the applied shear stress, the purity of the material, temperature and type of dislocation (Hull, 1975).

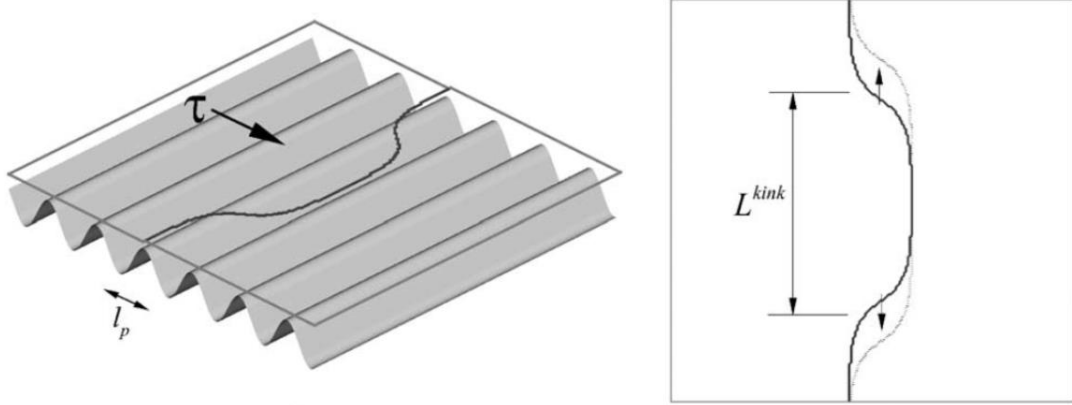


Figure 4.1: Schematic of the double-kink mechanism (Stainier et al., 2002b).

The model for the dislocation velocity assumes dislocation to travel between obstacles at very high velocity i.e. short time, dt_m , but waits in front of these obstacles i.e. long wait times, dt_w , for the thermal activation to overcome these obstacles (Gottstein, 2004; P. Larour et al., 2013). Expressions for the strain rate are obtained from consideration of transition state theory, activation volume of the dislocations and the Orowan's expression for average dislocation velocity (Zerilli, 2004), and are as given in the table below (Follansbee & Kocks, 1988; J. R. Klepaczko & Chiem, 1986; Stainier et al., 2002a).

Table 4.2: Table showing expression for dislocation properties.

Dislocation Velocity	$v_D = \frac{s^*}{\Delta t_w + \Delta t_m} = \frac{s^*}{\Delta t_w} = s^* \cdot v_0 \cdot \exp\left[\frac{-\Delta G(\sigma^*)}{kT}\right]$	(P. Larour et al., 2013)
	$v = 2l_p v_D e^{-\beta E^{\text{kink}}} \sinh\left(\beta E^{\text{kink}} \frac{\tau}{\tau_0}\right)$	(Stainier et al., 2002b)
	$v^\alpha = \lambda^\alpha v_{\text{attack}} \exp\left(-\frac{Q_{\text{slip}}}{k_B T}\right) \sinh\left(\frac{\tau_\text{eff}^\alpha V^\alpha}{k_B T}\right) \text{sgn}(\tau^\alpha)$	(Roters et al., 2010)

Orowan's strain rate	$\dot{\varepsilon} = \frac{\rho_m \cdot b \cdot v_D}{M_T}$	(P. Larour et al., 2013; Zerilli, 2004)
Strain rate expressions	$\dot{\varepsilon}(T, \sigma^*) = \dot{\varepsilon}_0 \cdot \exp\left[-\frac{\Delta G(\sigma^*)}{k \cdot T}\right]$	(Follansbee & Kocks, 1988; P. Larour et al., 2013; Nemat-Nasser et al., 1998; Zerilli, 2004)
	$\dot{\gamma} = \gamma_0^{\text{kink}} e^{-\beta E^{\text{kink}}} \sinh\left(\beta E^{\text{kink}} \frac{\tau}{\tau_0}\right)$	(Stainier et al., 2002b)

(* Please see corresponding literature for the definition of terms)

(Schulze & Vöhringer, 2000) has investigated the effect of most alloying element in iron based alloys to be an increase of the Peierl's energy barrier.

Expressions for the activation energy of formation of the kink-pair can be developed considering a line tension, LT , or an elastic interaction, EI , approximation models in the evaluation of the Pierel's energy potential, where the appropriate model is dependent on the temperature regime i.e. LT and EI model at lower and higher temperatures respectively (Brunner & Diehl, 1991b; Lim et al., 2015; Seeger, 2002).

While the expression for the Pierel's potential based on the LT or EI approximations have been shown to give correct description, most models at the continuum scale prefer to utilize phenomenological approximation of the barrier potential such as given in the table below (Cai et al., 2010; Follansbee & Kocks, 1988; Salvado et al., 2017; Voyadjis & Abed, 2005). The combination of the expressions for the dislocation kinematics as presented in the immediate forgoing table and the expressions for the activation energy results in different expressions for the thermal stress which are as presented in the table below.

Table 4.3: Table showing different expression for the activation energy and resulting thermal stress.

Activation Energy Expression	Expression of Thermal/Viscous/Friction Stress	Reference
$\Delta H_{kp}^* = 2H_k - 2\sqrt{\frac{\mathcal{T}bh^3}{2}\tau^*}$ (EI approx.)	$\tau^* = \tau_p^{El} \left(1 - \frac{k_B T \ln(\dot{\gamma}_0/\dot{\gamma})}{2H_k} \right)^2 = \tau_p^{El} \left(1 - \frac{T}{T_c(\dot{\gamma})} \right)^2$ $\tau_p^{El} = 2H_k^2/\mathcal{T}bh^3$ $T_c(\dot{\gamma}) = 2H_k/k_B \ln(\dot{\gamma}_0/\dot{\gamma})$	(Brunner & Diehl, 1991a; Lim et al., 2015)
$G = G_0 \left(1 - \left(\frac{\sigma_{th}}{\hat{\sigma}} \right)^p \right)^q$ (Kock's approx.)	$\sigma_{th} = \hat{\sigma} \{ 1 - [-(kT/G_0) \ln(\dot{\varepsilon}/\dot{\varepsilon}_0)]^{1/q} \}^{1/p}$	(Balasubramanian & Anand, 2002; Cai et al., 2010; Follansbee & Kocks, 1988; Rusinek et al., 2007)
$G = G_0 - \tau_{th} V$	$\sigma_{th} = \frac{G_0}{V_0} \exp(-\beta T), \quad \beta = \beta_0 - \frac{k}{G_0} \ln \frac{\dot{\varepsilon}}{\dot{\varepsilon}_0}$	(Cai et al., 2010; Voyadjis & Abed, 2005)
$G(\sigma_{th}) = G_0 \left\{ 1 - \frac{\ln[1+q(\sigma_{th}/\hat{\sigma})^p]}{\ln(1+q)} \right\}$ (Cai approx.)	$\sigma_{th} = \hat{\sigma} \langle (q^{-1} + 1)(\dot{\varepsilon}/\dot{\varepsilon}_0)^{(kT/G_0)\ln(1+q)} - q^{-1} \rangle^{1/p}$	(Cai et al., 2010)
	$\frac{\tau_p}{\tau_0} = \frac{1}{\beta E^{\text{kink}}} \operatorname{asinh} \left(\frac{\dot{\gamma}}{\dot{\gamma}_0^{\text{kink}}} e^{\beta E^{\text{kink}}} \right)$	(Kuchnicki et al., 2008; Stainier et al., 2002b)

(* Please see corresponding literature for the definition of terms)

Other expressions for the thermal stress which considers expressions for the thermal activation differently than those already stated i.e. thermal activation based on; purely thermodynamic quantities (Testa et al., 2020) or on evolution of mobile and forest dislocation densities as well as the mean free path of dislocation travel (Voyadjis & Abed, 2005), result in different expressions for the thermal stress as presented in the following table.

Table 4.4: Table showing other expressions for the thermal stress.

Expression of Thermal/Viscous/Friction Stress	Reference
$\sigma^* = \frac{cT_m}{v_0^*} \Delta_1 \Delta_2 \left\{ 1 + \frac{k}{c} \ln\left(\frac{\dot{\epsilon}}{\dot{\epsilon}_0}\right) \left[m \left(\frac{T}{T_2}\right)^m + \frac{T}{T_1} \left(1 - \frac{1}{\Delta_1}\right) \right] \right\}$ $\Delta_1 = 1 + A \exp\left(-\frac{T}{T_1}\right)$ $\Delta_2 = \exp\left(-\left(\frac{T}{T_2}\right)^m\right)$	(Testa et al., 2020)
$\sigma_{\text{th}} = \hat{Y} \left(1 - (\beta T)^{1/q}\right)^{1/p}$ $\beta = \beta_1 - \beta_2 \ln \dot{\epsilon}_p$ $\beta_1 = \frac{K}{G_0} \ln \left(\frac{\tilde{m} b \rho_m v_0}{1 - \tilde{m} l \lambda_1 / b + \tilde{m} b l \lambda_2 \rho_m + \tilde{m} l \lambda_3 \sqrt{\rho_f}} \right)$ $\beta_2 = \frac{K}{G_0}$	(Voyadjis & Abed, 2005)

(* Please see corresponding literature for the definition of terms)

Experimental investigations of the thermal stress have shown that the thermal stress increases with strain rate but decreases with temperature as shown in the figures 4.2 and 4.3.

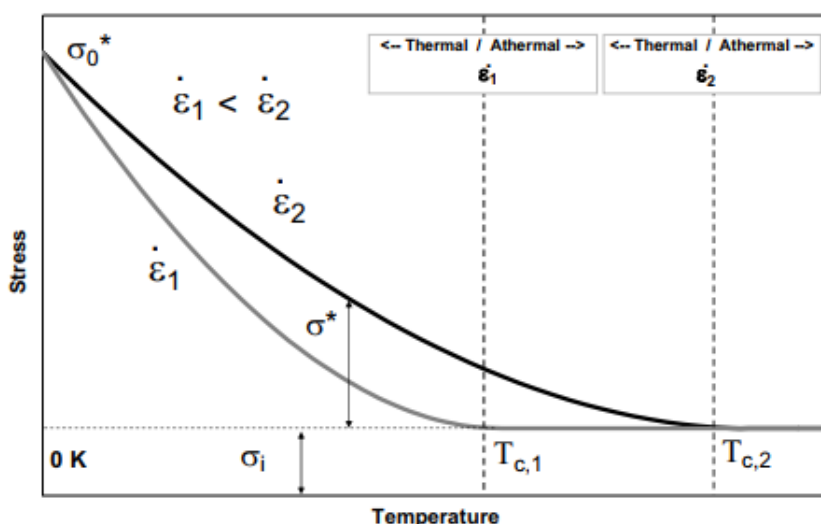


Figure 4.2: The variation of the viscous/thermal/friction stress with temperature at constant strain rates (P. (RWTH A. / I. Larour, 2010).

These expressions proposed to describe the Pierel's/thermal stress for *BCC* materials may be used to describe the stress required to activate mobile dislocation motion against the statistically distributed short range barrier of the forest dislocation in *FCC* crystals, however, with appropriate modifications which accounts for the change in the

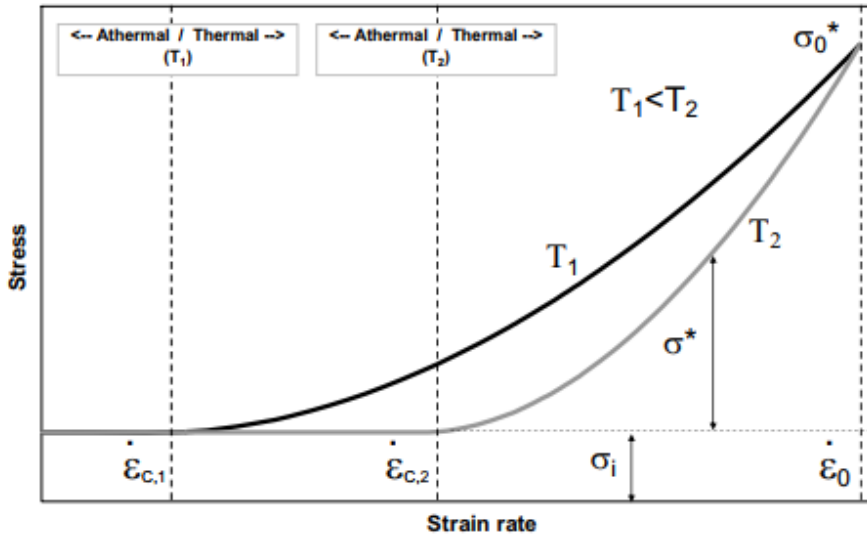


Figure 4.3: The variation of the viscous/thermal/friction stress with strain rate at constant temperatures (P. (RWTH A. / I. Larour, 2010).

density of the forest dislocation and invariably takes care of the evolution of the activation volume of the mobile dislocation due to the evolution of the forest dislocation as deformation progresses i.e. although the activation volume for *BCC* materials is constant with strain ([Butt, 2007](#); [Voyiadjis & Abed, 2005](#)), that for the *FCC* evolve with plastic strain. Therefore, some of the constants in the thermal stress expression for *BCC*, depending on what expression is used, become variables which evolve with plastic strain ([J. Klepaczko, 1975](#); [J. R. Klepaczko & Chiem, 1986](#); [Nemat-Nasser & Li, 1998](#)). Example expression of two such models are as shown in the following table.

Table 4.5: Table showing other expressions for the thermal flow stress for FCC materials.

Expression of Thermal Flow Stress	Reference
$\tau(\dot{\gamma}, \gamma, T) = \tau^o \left\{ 1 - \left[-\frac{KT}{G_0} \left(\ln \frac{\dot{\gamma}}{\dot{\gamma}_0} + \ln (1 + a(T)\gamma^{\frac{1}{2}}) \right) \right]^{\frac{1}{2}} \right\}^{\frac{3}{2}} [1 + a(T)\gamma^{\frac{1}{2}}]$ $\tau^o = \frac{G_0}{b\lambda l_0}, \quad \dot{\gamma}_0 = b\rho_m \omega_0 l_0, \quad a(T) = a_0 [1 - (T/T_m)^2]$	(Nemat-Nasser & Li, 1998)
$\sigma_{th} = \hat{\sigma} \left(1 - (\beta T)^{1/q} \right)^{1/p}$ $\beta = \beta_1 - \beta_2 \ln \dot{\epsilon}_p$ $\beta_1 = \frac{K}{G_0} \ln \left(\frac{\tilde{m}b\rho_m v_0}{1 - \tilde{m}l\lambda_1/b + \tilde{m}bl\lambda_2\rho_m + \tilde{m}l\lambda_3\sqrt{\rho_f}} \right)$ $\beta_2 = \frac{K}{G_0}$	(Voyiadjis & Abed, 2005)

(* Please see corresponding literature for the definition of terms)

4.2.1.2: Flow Stress Component Due to Athermally Overcome Barriers

For the *BCC* structured material, the lattice/Pierel's resistance usually determines the initial yield stress attained, while the strain hardening is primarily accomplished by long-range barriers (Lennon & Ramesh, 2004). Since the activation volume of mobile dislocation in *BCC* materials are relatively smaller than the spacing of the forest dislocations, (Stainier et al., 2002b) proposes the interaction of mobile dislocation and forest dislocations (athermal bowing out, and bypassing by the formation of Orowan loops around forest dislocation by the mobile dislocations) as an important part of the strain hardening. Some description of the athermal stress component in models based on mobile dislocation mechanics rely on the phenomenological power law based on plastic strain for the strain dependent athermal barrier such as the internal stress while the Hall-Petch relation describes the pile-up and/or grain boundary effects (Salvado et al., 2017; Voyiadjis & Abed, 2005). It is worth noting that the proposed description by

(Stainier et al., 2002b) has been shown by an earlier work of (Kuhlmann-Wilsdorf, 1989, 1999) to be relatable to the dislocation density of dislocations. The description of the athermal long range internal stress by (Mughrabi, 1983) also proposes a dislocation density based expression.

For the *FCC* structured material, the athermal contribution to flow stress is obtained from the effect of pile-up or grain boundary i.e. the Hall-Petch effect (Nemat-Nasser & Li, 1998).

A more elaborate equation which includes dislocation density evolution in the expression for the flow stress has been fully developed and presented in an early work by (J. Klepaczko, 1975). (Nemat-Nasser et al., 1998) has also applied the description of the thermal flow stress based on dislocation mechanics in developing an efficient and accurate computational algorithm for incremental calculation of the crystal deformation and stress state of polycrystalline Tantalum, a *BCC* material.

4.2.2: Flow Stress and Strain Hardening Models Based on Microstructural Dislocation Density

Models in this category are pioneered by the work of G. I. Taylor who first showed experimentally that there existed a relationship between the density of dislocation and the flow stress (Jiang et al., 2013). The first empirical expression showing this relationship was derived by Bailey and Hirsch based on the Frank-Read stress, τ , of supercritical bowing of dislocation (Kuhlmann-Wilsdorf, 1999) which relates the glide dislocation obstacle spacing to the supercritical bowing stress, and shows the obstacle spacing to scale with the inverse of the square root of the total dislocation density;

$$\tau = \tau_0 + \alpha G b \sqrt{\rho} \quad \text{Equation 4.1}$$

where τ_0 is the friction stress, G is the shear modulus, b is the Burger's vector, ρ is the forest dislocation density, and α is the constant.

The formalism of models in this group is a description of the form of the macroscopic plastic response of the flow stress by microscopic mechanical mechanisms associated with dislocation multiplication and reduction, by the statistics of mobile dislocation populations, by the nature of the obstacles and the statistics of obstacle distributions, and by the relationship between the externally imposed plastic strain rate and the dislocation kinetics.

The foremost in this category of models are the models proposed by the works of Kocks, Mecking and Estrin ([Y. Estrin & Mecking, 1984; Mecking & Kocks, 1981](#)).

The proposition by Kocks uses a power law to describe the associated flow which shows rate dependence of the flow stress;

$$\dot{\varepsilon}_{pl} = \dot{\varepsilon}_0 \left(\frac{\sigma}{\hat{\sigma}} \right)^m \quad \text{Equation 4.2.a}$$

$$\hat{\sigma} = M \alpha G b \sqrt{\rho} \quad \text{Equation 4.2.b}$$

where $\dot{\varepsilon}_{pl}$, $\dot{\varepsilon}_0$, σ , $\hat{\sigma}$, and m , are the plastic strain rate, a constant strain rate, the current flow stress, the flow stress at the constant strain rate, and the temperature dependent exponent.

In the proposition by ([Mecking & Kocks, 1981](#)), the kinetic equation is represented mathematically as;

$$\sigma = \alpha(\dot{\varepsilon}, T) \cdot \mu b \sqrt{\rho} + \sigma_0(\dot{\varepsilon}, T) \quad \text{Equation 4.3}$$

where α is a factor that represents the product of a factor which determines the dislocation interaction strength, and a factor which determines the thermal activation assistance in overcoming the barriers to dislocation motion at the current dislocation substructure, ρ is the total dislocation density, μ is the shear modulus, and σ_0 is an internal stress term which may represent the lattice resistance. The strain hardening in this model is evaluated to be due to the evolution of the total dislocation density with

plastic strain. This evolution rate is obtained as the sum of two opposing contribution from the storage rate of dislocation term and a dynamic recovery or annihilation rate facilitated by dislocation cross slip and climb at lower and higher temperatures respectively ([Chu & Morris, 1996](#); [Y. Estrin & Mecking, 1984](#); [Mecking & Kocks, 1981](#)) and results in a term which depends on the current total dislocation density, strain rate and temperature. This shows that the unit processes depend on one or a combination of these factors. Overall, the model predicts a linear decrease of strain hardening with respect to the applied stress, which only fairly represent experimental observation ([Barlat et al., 2002](#)). Modifications to a forest dislocation density dependence of the strain hardening predicts better results ([Chu & Morris, 1996](#)).

The model by Kocks and Mecking is classified as a one-parameter-internal-variable model as it considers only the total density of dislocation as the kinetic parameter for flow stress and the evolution rate. Other one-parameter-internal-variable evaluation of the evolution rate has been proposed by ([J. Klepaczko, 1975](#); [J. R. Klepaczko & Chiem, 1986](#)) where the rate is dependent on strain rate, temperature and mobile/total dislocation densities.

Another one-parameter-internal-variable model may be found in the work of ([Kuhlmann-Wilsdorf, 1999](#)) who developed an explicit flow stress expression in terms of the flow plastic strain however with accompanying equation consisting of an inverse temperature dependent dislocation retention factor resulting from the consideration of the generation and annihilation of dislocation, which relates the change in dislocation density to the change in flow strain, and invariably leads to an expression for the change in flow stress in relation to the dislocation density.

A recognition of the heterogeneous or cell forming nature of the microstructure during monotonic deformation has also seen a representation of the microstructure as a

composite, and the evaluation of the flow stress as a volume fraction sum of the local flow stress of the immobile dislocation density within the cell and the cell wall ([Mughrabi, 1983, 1987; Zehetbauer, 1993](#)), the so-called composite-one-parameter-internal-variable models.

One-internal-variable models are the simplest possible means of using the microstructural parameter to predict the flow stress. These models are sufficient for describing monotonic deformation without abrupt changes of the deformation rate or the deformation path but fail to account for transient and/or cyclic processes, or complex strain hardening behaviour at large strains, where multi-parameter-internal variable models are necessary ([Barlat et al., 2002; Y. Estrin, 1998; Sedláček & Blum, 2002](#)).

Early attempts at multi-parameter-internal-variable model is presented in the work of ([Bergström, 1970](#)). In this model the flow stress is presented as consisting of components from a thermal stress or friction stress, an athermal strain independent stress due to short range interaction with particles and an athermal long range stress due to the total dislocation density. In evaluating the strain hardening, the total dislocation density is shown to result from a transaction between the mobile and immobile dislocation densities. The dislocation transaction is rationalized to be the creation, immobilization, remobilization and annihilation of dislocations. The terms resulting from the analysis of each processes, which are dependent on one or a combination of strain rate, temperature and the immobile or mobile dislocation densities, are summed up to give the total dislocation density evolution rate. Experimental application of the model showed its descriptive capability which is dependent on the accuracy of certain microscopy measurements.

Extensive research undertaken by ([Y. Estrin, 1998](#); [Yuri Estrin, 1996](#)) first considered the effects of more microstructural features such as cell formation, geometric obstacles e.g. grain boundaries, phase boundaries, particle effects (both shearable and nonshearable particles) etc., Pierel's resistance, and solute drag effects (stationary solutes, and nonstationary solutes which lead to dynamic strain aging, *DSA*), on the Kocks_Mecking model for the evolution rate of the total dislocation density. Afterwards, an introduction of a two-parameter-internal-variable evolution rate equation based on the mobile, and relatively immobile or locally mobile forest dislocation densities. In this model the flow stress is derived to be related to the square root of the forest dislocation density and not the total dislocation density. Experimental validation was undertaken on an aluminium alloy. The model made good descriptions in monotonic deformations, and also good predictions in a transient deformation process.

([Barlat et al., 2002](#)) improved on the model by Y. Estrin in recognition of its inadequate prediction at low stresses. Using a three-parameter-internal variable evolution rate of the mean free path length of travel of the mobile dislocation, and the mobile and forest dislocation densities, accurate predictions at low and high stresses were obtained.

Extensive study by ([Y. Estrin et al., 1998](#)) of copper deformed by torsion to large strains resulted in a composite description of the flow stress due to the heterogeneous cell structure, and a dislocation based model for strain hardening for the cell wall and cell interior. The dislocation processes, within the cell interior and walls, considered were generation, annihilation and incorporation of cell interior dislocation into the cell wall. The resulting equations for the unit processes were shown to be functions of the densities of the cell interior and wall dislocations. The volume fraction of cell walls was

predicted to decrease with strain. The model showed good predictions of the earlier measured strain hardening of copper at different strain hardening stages.

([Roters et al., 2000](#)) utilizing a composite flow stress model based on the densities of the cell wall and immobile cell interior dislocation described the stress-strain curve for an aluminium alloy. The evolution rate was modelled as a three-parameter-internal variable equation based on the cell mobile, wall and interior dislocation densities. The dislocation processes considered in determining the evolution rates were the annihilation, formation of locks and dipoles, and incorporation of dipoles into cell wall, and all were in terms of the mobile dislocation density, which leads to a reduced optimization effort.

Collaborative efforts by ([Holmedal et al., 2005](#); [Nes et al., 2000](#)) has resulted in the development of a so-called Microstructure-based Metal Plasticity, *MMP*, model. Following the basic principle of dislocation storage and dynamic recovery, the model considers multiple parameters of the dislocation substructure i.e. the cell size, cell wall thickness, wall dislocation density, cell interior dislocation density, and the sub-boundaries misorientation. The evolution rate is derived as a set of differential equations of three parameters; the cell size, the cell interior dislocation density, and the sub-boundaries misorientation. The inclusion into the evolution rate of the mobile dislocation velocity in terms of the Orowan's strain rate makes the evolution rate sensitive to dislocation properties. The flow stress in this treatment is implicitly defined as a summation of contributions from an athermal and a thermal components, where the athermal component is explicitly a contribution from the density of cell interior dislocation, and sub-boundaries which has often been experimentally shown to be a predictor of flow stress ([D. A. Hughes & Hansen, 2018](#); [Li et al., 2004](#)). The *MMP* model has been shown to be able to predict flow curves for the entire temperature

range, large strain rates, creep, and strain-path change i.e. cross hardening and reversals, as well as stacking fault energy and dynamic-strain aging effects etc.

The thrust of this work is an application of the plasticity model developed by ([Amir & Prahls, 2019](#)).

4.3: Amir & Prahls Model

This model relies on describing plasticity at a nonlocal level i.e. the plastic behaviour at a material point is an average representation of all the plastic properties of an aggregate of material space, a so-called representative microstructural volume, RMV, shown in the figure below.

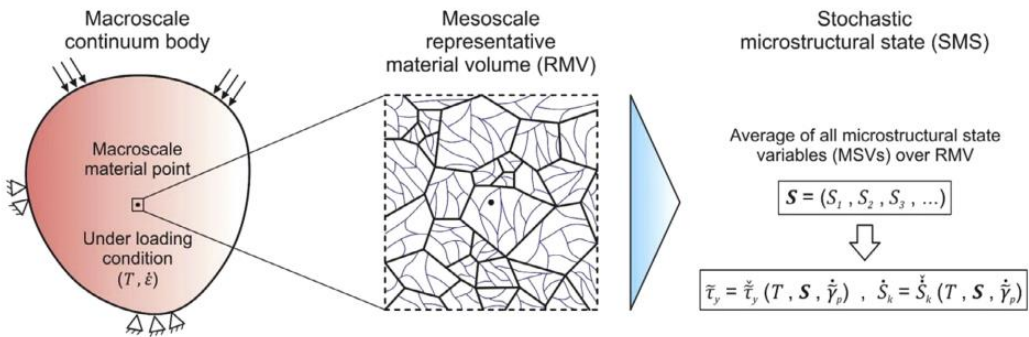


Figure 4.4: Schematic representation of the multiscale nature current model ([Amir & Prahls, 2019](#))

The model describes monotonic viscoplastic deformation, just as in other already discussed models, based on three-internal-variables i.e. the dislocation densities of the cell mobile, cell immobile and wall dislocations i.e. a three-parameter-internal-variable model.

The strength of this model is that it considers explicitly a wider range of unit dislocation processes under the grouping of athermal storage and thermal activated recovery in arriving at expressions for the flow curve during monotonic deformation.

The proposition and mathematical formulary of the model are summarized as follows;

- The microstructural state of a material can be represented by a set, \mathbf{S} , of non-local microstructural state variable, MSVs. The MSVs may be various dislocation density types, grain size, phase fractions, recrystallized fraction, precipitate size and concentration etc.

Equation P. 1

$$\mathbf{S} = \mathbf{S}(S_1, S_2, S_3, \dots)$$

- Dislocations are of three kinds; cell mobile, cell immobile and wall immobile dislocations. The sum of all three represents the total dislocation density.

$$S = S(\rho_{cm}, \rho_{ci}, \rho_{wi})$$

Equation P. 2

where cm , ci , and wi are the cell mobile, cell immobile, and wall immobile dislocations.

- The time rate of evolution of each MSV is a function of the thermo-mechanical loading and \mathbf{S} .

$$\dot{\mathbf{S}}_t = \dot{\mathbf{S}}_t(T, \mathbf{S}, \dot{\gamma}_p)$$

Equation P. 3

- The critical yield/shear stress at the slip systems is an implicit function of temperature, T , shear strain rate, $\dot{\gamma}_p$, and the statistical state of the microstructure, \mathbf{S} .

$$\tau_y = \tau_y(T, \mathbf{S}, \dot{\gamma}_p)$$

Equation P. 4

- The average macroscopic flow/yield stress, σ_y and plastic strain, ϵ_p of the RMV is related crystallographic critical shear stress, τ_y and shear strain, $\dot{\gamma}_p$ of the individual grains by the Taylor factor;

$$M = \frac{\sigma_y}{\tau_y} = \frac{d\gamma_p}{d\epsilon_p}$$

Equation P. 5

- The yield stress, τ_y is decomposed into the viscous stress contribution due to the lattice resistance, τ_v and the plastic stress contribution due to the deformation mechanisms at play, τ_p .

$$\tau_y = \tau_v + \tau_p \quad \text{Equation P. 6.a}$$

Following equation above, an average macroscopic relation may be derived;

$$\sigma_y = \sigma_v + \sigma_p \quad \text{Equation P. 6.b}$$

- The average macroscopic viscous stress, σ_v is a function of the average macroscopic plastic strain rate, $\dot{\epsilon}_p$ and the absolute temperature, T ;

$$\sigma_v = \sigma_{v00} [1 + r_v (\hat{T} - 1)^{s_v}] \dot{\epsilon}_p^{m_v}$$

$$\hat{T} = \frac{T}{T_0}; \quad \dot{\epsilon}_p = \frac{\dot{\epsilon}_p}{\dot{\epsilon}_0}; \quad \text{Equation P. 7}$$

$$r_v < 0; \quad 0 < s_v \leq 1;$$

where r_v , s_v , m_v , σ_{v00} , and T_0 are the temperature sensitivity coefficient, exponent, strain rate sensitivity parameter, strain rate and temperature reference viscous stress, and absolute reference temperature respectively. The reference temperature and strain rate are the lowest temperature and strain rate in the investigated regime. The strain rate sensitivity parameter is also proposed to be a function of strain rate and temperature, as shown below;

$$m_v = m_{v0} \left[1 + r_v^m (\hat{T} - 1)^{s_v^m} \right] \dot{\epsilon}_p^{m_v^m} \quad \text{Equation P. 8}$$

$$r_v^m, s_v^m \geq 0;$$

where m_{v0} , r_v^m , s_v^m , and m_v^m are the reference strain rate and temperature strain rate sensitivity parameter, the temperature coefficient and exponent associated with the reference strain rate sensitivity parameter, and strain rate sensitivity parameter of the strain rate sensitivity.

- Mobile dislocations are the main carriers of plastic strain and their interactions, driven by the stress applied result in the progressive formation of heterogeneous dislocation substructure i.e. the cell structure, and the hardening of the substructure, of which the wall immobile contributes the most.
- The plastic stress, τ_p is proportional to the average spacing of immobile dislocations, and the latter is also proportional to the density of the immobile dislocations as proposed by Taylor, Bailey and Hirsch. The plastic stress may be decomposed into contributions from different entities of the heterogeneous structure i.e. the immobile cell wall, τ_{pw} and immobile cell interior, τ_{pc} of the cell structure;

$$\tau_p = \tau_{pc} + \tau_{pw} \quad \text{Equation P. 9.a}$$

$$\tau_{px} = MbG\alpha_x\sqrt{\rho_{xi}} ;$$

$$G\alpha_x = G_0\alpha_{x0}[1 + r_{ax}^G(\hat{T} - 1)^{s_{ax}^G}]; \quad \text{Equation P. 9.b}$$

$$r_{ax}^G < 0; s_{ax}^G > 0;$$

$$x = c (\text{cell}), w (\text{wall});$$

where G_0 , α_{x0} , r_{ax}^G and s_{ax}^G are the reference shear modulus, reference interaction strength, and temperature sensitivity coefficient and exponent respectively.

- The static and dynamic evolution of the dislocation density in a representative volume is an algebraic addition of the rate processes of dislocation increase and decrease within such volume i.e. athermal storage and recovery.
- 6 main types of dynamic dislocation processes ([Davoudi & Vlassak, 2018](#); [Shanbhag & Zikry, 2011](#); [Stainier et al., 2002a](#)) are considered as most important i.e. generation/multiplication of mobile dislocation, **gn**, annihilation of mobile and/or immobile dislocation, **an**, accumulation of immobile

dislocations, **ac**, trapping of mobile dislocations (locking and pinning of mobile dislocation by interstitial/impurity solutes), **tr**, nucleation of wall dislocations, **nc**, remobilization of immobile dislocations, **rm**, etc. Two types of static dislocation processes on the other hand are considered i.e. static pinning by impurity/solute atoms and static remobilization (junction dissociation and dislocation climb).

- The time rate of evolution of the dislocation densities, ρ_{xy} are given as;

$$\hat{\rho}_{xy} = \frac{\rho_{xy}}{\rho_0}; \quad \begin{cases} x = c, w \\ y = m, i \end{cases} \quad \text{Equation P. 10.a}$$

$$\dot{\hat{\rho}}_{wi} = \dot{\hat{\rho}}_{wi}^{nc} + \dot{\hat{\rho}}_{wi}^{ac} - (\dot{\hat{\rho}}_{wi}^{an} + \dot{\hat{\rho}}_{wi}^{rm}) \quad \text{Equation P. 10.b}$$

$$\dot{\hat{\rho}}_{ci} = \dot{\hat{\rho}}_{cm}^{tr} + \dot{\hat{\rho}}_{ci}^{ac} - (\dot{\hat{\rho}}_{ci}^{an} + \dot{\hat{\rho}}_{ci}^{rm} + \dot{\hat{\rho}}_{wi}^{nc}) \quad \text{Equation P. 10.c}$$

$$\dot{\hat{\rho}}_{cm} = \dot{\hat{\rho}}_{cm}^{gn} + \dot{\hat{\rho}}_{ci}^{rm} + \dot{\hat{\rho}}_{wi}^{rm} - (2\dot{\hat{\rho}}_{cm}^{an} + \dot{\hat{\rho}}_{ci}^{an} + \dot{\hat{\rho}}_{wi}^{an}) \quad \text{Equation P. 10.d}$$

$$+ \dot{\hat{\rho}}_{ci}^{ac} + \dot{\hat{\rho}}_{wi}^{ac} + \dot{\hat{\rho}}_{cm}^{tr})$$

$$\dot{\hat{\rho}}_{cm}^{gn} = Mc_{cm}^{gn} \frac{\hat{\rho}_{cm}}{\sqrt{\hat{\rho}_{ci} + \hat{\rho}_{wi}}} \dot{\epsilon}_p \quad \text{Equation P. 10.e}$$

$$\dot{\hat{\rho}}_{xy}^{an} = Mc_{xy}^{an} \hat{\rho}_{cm} \hat{\rho}_{xy} \dot{\epsilon}_p; \quad \text{Equation P. 10.f}$$

$$xy = cm, ci, wi;$$

$$\dot{\hat{\rho}}_{xi}^{ac} = Mc_{xi}^{ac} \hat{\rho}_{cm} \sqrt{\hat{\rho}_{xi}} \dot{\epsilon}_p \quad \text{Equation P. 10.g}$$

$$\dot{\hat{\rho}}_{xi}^{rm} = Mc_{xi}^{rm} \hat{\rho}_{xi} \dot{\epsilon}_p \quad \text{Equation P. 10.h}$$

$$\dot{\hat{\rho}}_{wi}^{nc} = Mc_{wi}^{nc} \hat{\rho}_{cm} \hat{\rho}_{ci}^{3/2} \dot{\epsilon}_p \quad \text{Equation P. 10.i}$$

$$\dot{\hat{\rho}}_{cm}^{tr} = Mc_{cm}^{tr} \hat{\rho}_{cm}^{3/2} \dot{\epsilon}_p \quad \text{Equation P. 10.j}$$

where c_{xy}^z is the material constants/parameters of the dislocation of type xy associated with the dislocation process z . The constitutive parameters, except those for generation and accumulation which are athermal, also depend on the strain rate and temperature as shown below;

$$c_{xy}^z = c_{xy0}^z [1 + r_{xy}^z (\hat{T} - 1)^{s_{xy}^z}] \dot{\epsilon}_p^{m_{xy}^z}$$

Equation P. 11

$$m_{xy}^z = m_{xy0}^z [1 + r_{z_{xy}}^m (\hat{T} - 1)^{s_{z_{xy}}^m}]$$

r_{xy}^z	> 0	$z = an, tr, rm, spn, srm$
	<, =, or > 0	$z = nc$
	= 0	$z = gn, ac$

s_{xy}^z	> 0	$z = an, tr, nc, rm$
	= 0	$z = gn, ac$

m_{xy}^z	< 0	$z = an, tr$
	<, =, or > 0	$z = nc, rm$
	= 0	$z = gn, ac$

where c_{xy0}^z , r_{xy}^z , s_{xy}^z , and m_{xy}^z are the reference material constant, temperature coefficient, exponent, and strain sensitivity parameter associated with the material constant of the dislocation of type \mathbf{xy} associated with the dislocation process \mathbf{z} . m_{xy0}^z , $r_{z_{xy}}^m$, and $s_{z_{xy}}^m$, are the reference strain rate and temperature strain rate sensitivity parameter of the dislocation of type \mathbf{xy} associated with the dislocation process \mathbf{z} , the temperature coefficient and exponent associated with the reference strain rate sensitivity parameter of the dislocation of type \mathbf{xy} associated with the dislocation process \mathbf{z} .

- The dissipation factor/Taylor-Quinney coefficient which expresses the efficiency of conversion of plastic work into heat is expressed as;

$$\beta = \left[\frac{2(\dot{\rho}_{cm}^{an} + \dot{\rho}_{ci}^{an} + \dot{\rho}_{wi}^{an})}{\dot{\rho}_{cm}^{gn}} \right]^k; \quad \text{Equation P. 12}$$

$$k > o;$$

where k is the material constant associated with the dissipation factor.

- The strain hardening, θ , is obtained as a summation of the contributions from the cell and wall immobile dislocation;

$$\theta = \theta_c + \theta_w$$

$$\theta_x = \frac{d\hat{\rho}_{xi}}{2\hat{\rho}_{xi} d\epsilon_p} \sigma_{px}; \quad \text{Equation P. 13}$$

$$x = c, w$$

- The strain-rate hardening, φ , is also a summation of hardening contributions from the viscous and the plastic stress;

$$\varphi = \varphi_v + \varphi_{pw} + \varphi_{pc}$$

$$\varphi_v = \frac{m_v}{\dot{\epsilon}_p} [1 + m_v^m \ln \dot{\epsilon}_p] \sigma_v \quad \text{Equation P. 14}$$

$$\varphi_{px} = \frac{d\hat{\rho}_{xi}}{2\hat{\rho}_{xi} d\dot{\epsilon}_p} \sigma_{px};$$

$$x = c, w$$

Chapter 5: Experiments

5.1: Chemical Composition

The chemistry of the S700 steel sheets were measured on a Spectrometer machine, which employs the principle of spectroscopy i.e. characteristic wavelength emission of elements, to determine the chemical composition of materials. Extensive experimental use of this principle has given credence to the reliability of this test method for determining chemical composition.

5.2: Preparation of Sheet Specimen

The as-received S700 single phase steel sheets of 2mm thickness were prepared for tensile test by wire-cutting the sheets to a geometry specified by the ASTM E8 ([ASTM E8, 2010](#)) recommendations for tensile test (gauge length of 30mm), after which the cut samples surfaces were water-jet milled and then polished to remove all surface groove and macro-surface-defects since these surface defects have been shown to encourage early onset of failure by crack ([Dieter, 2011](#); [Wagoner & Chenot, 2001](#)). Care is taken to cut the samples with the rolling direction of the sheet as the direction of the longest dimension of the specimens. In total 88 samples are prepared for tensile test, and other samples were prepared for microstructure measurements before and during interrupted tests.

5.3: Electron Back Scatter Diffraction, EBSD, Measurement

The EBSD is a versatile measurement technique for investigation of microstructure to obtain information about micro-texture, defect density, grain size, phase contents etc ([Field et al., 2012](#); [Jiang et al., 2013](#)). Samples for *EBSD* were prepared by standard mechanical polishing to 0.05 microns, followed by electro-polishing in a mixture of 5% perchloric acid and 95% acetic acid

solutions (volume ratios) with an applied voltage of 35V. Measurements are performed using a field emission gun scanning electron microscope (FEG-SEM), JOEL JSM 7000F, at 20 KeV beam energy, approximately 30 nA probe current, and 100-300 nm step size. A Hikari EBSD camera by Ametek-EDAX, in combination with the OIM software suite (OIM Data Collection and OIM Analysis V7.3) by EDAX-TSL, is used for data acquisition and analysis. Subsequently, at each point, GND density is calculated from kernel average misorientation (KAM) which is the average angular deviation between a point and its neighbors in a distance twice the step size as long as their misorientation does not exceed 5° . After mapping KAM values to GND density, over a representative area with the size of $100 \times 100\mu\text{m}$, the average GND density is calculated (Amir & Prahl, 2019).

5.4: Tensile Tests

Tensile test were performed using a servo-hydraulic MTS machine with a heating chamber for the strain rates $10^{-4}/\text{s}$, $10^{-3}/\text{s}$, $10^{-2}/\text{s}$, and $10^{-1}/\text{s}$, at 11 temperatures within the range $25^\circ\text{C} – 500^\circ\text{C}$ [25, 50, 100, 150, 200, 250, 300, 350, 400, 450, 500]. For each temperature and strain rate at least 2 tests are performed from which an average of the obtained tensile data is taken to represent the test result at that temperature and strain rate. Precautions were properly taken to mount the specimen in the machine such that no bending occurred. The chamber and the specimen mounted are allowed, as usual, a stable equilibrium heating time to reach the test temperature before the tests commences.

Chapter 6: Results, Discussion and Validation

6.1: Chemical Composition

The results of the chemical composition test on the material is as presented in the table below:

Table 6.1: Chemical Composition of the S700 single phase steel specimens.

Element	Test 1	Test 2	Average
Mn	1.911	1.9316	1.9213
Si	0.487	0.497	0.492
Mo	0.131	0.131	0.131
Ti	0.1255	0.1279	0.1267
Al	0.072	0.074	0.073
C	0.071	0.073	0.072
Nb	0.048	0.049	0.0485
Cr	0.044	0.044	0.044
Ni	0.035	0.036	0.0355
Cu	0.024	0.025	0.0245
W	0.012	0.014	0.013
Co	0.0086	0.0087	0.00865
P	0.0086	0.0086	0.0086
V	0.0065	0.0066	0.00655
Sn	0.005	0.005	0.005
N	0.004	0.0048	0.0044
As	0.0034	0.0036	0.0035
Zr	0.003	0.003	0.003
Ce	0.003	0.003	0.003
Zn	0.002	0.002	0.002
Ca	0.0014	0.0015	0.00145
Sb	0.001	0.001	0.001
Pb	0.001	0.001	0.001
Bi	0.001	0.001	0.001
Mg	0.0009	0.001	0.00095
Si	0.0007	0.0007	0.0007
La	0.0005	0.0005	0.0005
B	0.0001	0.0002	0.00015

From the chemistry as presented in the table, it may be observed that the steel is a low-Manganese interstitial free steel, since the presence of chromium, titanium and niobium are enough to bind the carbon content resulting in the formation of carbides. Other elements may be regarded as for substitutional hardening, while others are trace elements.

6.2: Tensile Test and Computational Curves.

6.2.1: Processing the Uniaxial Tensile Test Data

The results obtained from the tensile test experiment is the force applied, and the elongation of the material which is converted to the engineering stress, σ_e , and engineering strain, ε_e , by the relation;

$$\sigma_e = \frac{F \text{ (applied force)}}{A_0 \text{ (original area of specimen)}} \quad \text{Equation 6.1.a}$$

$$\varepsilon_e = \frac{u \text{ (elongation)}}{l_0 \text{ (original guage length of specimen)}} \quad \text{Equation 6.2.b}$$

The engineering stress and engineering strain data is converted to a true stress, σ_t , and true strain, ε_t , data by the relation;

$$\sigma_t = \sigma_e(1 + \varepsilon_e) \quad \text{Equation 6.3.a}$$

$$\varepsilon_t = \ln(1 + \varepsilon_e) \quad \text{Equation 6.3.b}$$

Only the data for the true stress and true strain will be presented in the subsequent sections. Also the curves are presented in 3 sets of low, medium, and high temperatures for each strain rate.

6.2.2: Obtaining the Constitutive Parameters

To obtain the computational curves, since there are no easily conceivable analytical solutions for the differential equation set up for the dislocation density i.e. *equations P. 10.a – P. 10.j*, in the postulates, a common method to get around this problem is to employ the numerical integration technique i.e. discretization of the differential equation into n steps. Mathematically this is presented as;

Let f represent any quantity which varies with time. The rate of variation may be approximated as thus;

forward/explicit Euler discretization method

$$\dot{f}(t) \approx \frac{\Delta f^{n+1}}{\Delta t^{n+1}} = y(f^n, t^n) \quad \text{Equation 6.4.a}$$

backward/implicit Euler discretization method

$$\dot{f}(t) \approx \frac{\Delta f^{n+1}}{\Delta t^{n+1}} = y(f^{n+1}, t^{n+1}) \quad \text{Equation 6.4.b}$$

$$\Delta f^{n+1} = f^{n+1} - f^n \quad \text{Equation 6.4.c}$$

Applying this concept, in our case, the forward/explicit Euler discretization method, to the differential equations for the dislocation density, the following relations are obtained;

$$\Delta \hat{\rho}_{xy}^n = \Delta t^{n+1} \dot{\hat{\rho}}_{xy}^n = \Delta \varepsilon_p^{n+1} \frac{\partial \hat{\rho}_{xy}^n}{\partial \varepsilon_p} \quad \text{Equation 6.5.a}$$

$$\hat{\rho}_{xy}^{n+1} = \hat{\rho}_{xy}^n + \Delta \hat{\rho}_{xy}^n \quad \text{Equation 6.5.b}$$

These relations are applied to *equations P. 10.b –P.10.d* to obtain the evolution of the internal variables i.e. **cm**, **ci**, and **wi** densities, where $\frac{\partial \hat{\rho}_{xy}^n}{\partial \varepsilon_p}$ are obtained from the *equations P. 10.e –P.10.j*, after which the results are applied appropriately to the *equations P. 7, P. 8, P. 9.a, and P. 9.b* such that at each **nth** step, the yield stress is calculated as given in *equation P. 6.b*.

Given the foregoing, to obtain the constitutive parameters, a point-wise parameter optimization of the error function obtained from a comparison between the computed curve and the processed tensile data as reference, is carried out using the optimization tool available on the MATLAB software, Global-Search optimization which employs the local minimization solver *fmincon* to determine the global minimum solution of the error function following the gradient based optimization method ([Pulkkinen, 2008](#)). The error function is given as;

$$\tilde{e}(C) = \sum_{j=1}^L \sum_{i=1}^M \frac{1}{N} \sum_{n=0}^N \frac{|\sigma_{num}^n(C, T_i, \Delta\epsilon_p^n, S^n, \dot{\epsilon}_j) - \sigma_{exp}^n(T_i, \epsilon_p^n, \dot{\epsilon}_j)|}{\sigma_{exp}^n(T_i, \epsilon_p^n, \dot{\epsilon}_j)} \quad \text{Equation 6.6}$$

where

- C is the set of constitutive parameters for fitting,
- L is the total number of strain rate,
- M is the total number of temperatures at a specific strain rate,
- N is the total number of steps/data points at a particular temperature, T_i , and strain rate, $\dot{\epsilon}_j$,
- S^n is the set of MSVs at a specific temperature and strain rate,
- $\Delta\epsilon_p^n$ is the step length which for our data is approximately equal to 0.001,
- σ_{exp}^n and σ_{num}^n are the yield stress and numerically computed stress at specific step or strain, temperature and strain rate.

Before the tensile data is used for the optimization procedure, the noise of the flow curves are removed by smoothing or fitting the experimental data with a smooth polynomial curve, then data from interpolation at a desirable step length is obtained. The strain rate dependency of the strain-rate-sensitivity parameters for the viscous stress, and the constitutive parameters is dropped based on the literature (P. Larour et al., 2013).

It is noteworthy to state that the optimization process which has a stochastic nature produces results which are dependent on the start guess-value of the optimization run as well as the bounds prescribed. Due to this, several trial runs will result in different result i.e. non-unique results, as has been noted by (Domkin, 2005). The choice result was determined by inspection of the prediction of the constitutive parameters and verification by simulation. After multiple optimization runs, the best error estimate obtained was 0.31 which is a 31% error.

Table 6.2: Reference constant and normalization parameters.

T_0 [°C]	G_0 [MPa]	M	ρ_0 [m^2]	b [m]	$\dot{\varepsilon}_0$ [s^{-1}]
25	81500	3.15	10^{12}	2.55×10^{-10}	0.0001

Table 6.3: Table of constitutive parameters determined from the optimization.

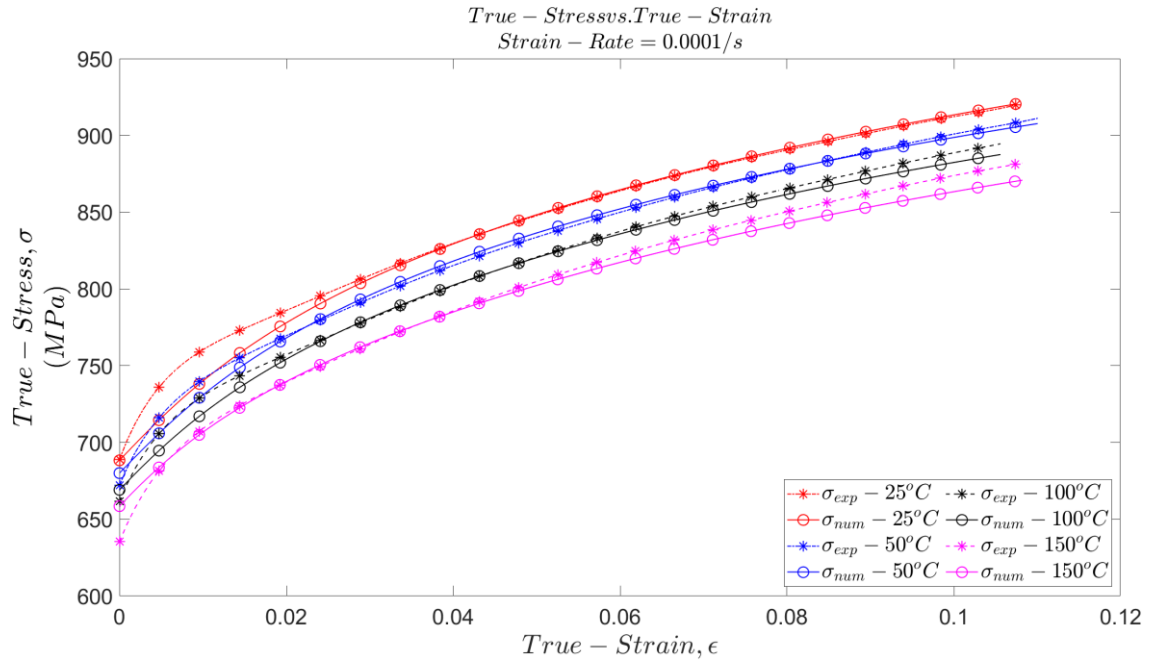
Dislocation Process/ Property	Material Coefficient/Parameter Value					
Generation	c_{cm}^{gn}					
	1581.9298					
Annihilation	c_{cm0}^{an}	r_{cm}^{an}	s_{cm}^{an}	m_{cm0}^{an}	$r_{an_{cm}}^m$	$s_{an_{cm}}^m$
	0.0670	2.6608	1.5463	0.2145	-7.9492	0.4537
	c_{ci0}^{an}	r_{ci}^{an}	s_{ci}^{an}	m_{ci0}^{an}	$r_{an_{ci}}^m$	$s_{an_{ci}}^m$
	0.0048	6.7067	5.2220	0.0827	-4.5127	9.0857
	c_{wi0}^{an}	r_{wi}^{an}	s_{wi}^{an}	m_{wi0}^{an}	$r_{an_{wi}}^m$	$s_{an_{wi}}^m$
	0.0701	-0.0625	3.3302	0.0299	1.2877	7.5921 e-05
Trapping	c_{cm0}^{tr}	r_{cm}^{tr}	s_{cm}^{tr}	m_{cm0}^{tr}	$r_{tr_{cm}}^m$	$s_{tr_{cm}}^m$
	9.2809	0.5242	4.6520	0.1674	-0.0765	5.6774
Nucleation	c_{wi0}^{nc}	r_{wi}^{nc}	s_{wi}^{nc}	m_{wi0}^{nc}	$r_{nc_{wi}}^m$	$s_{nc_{wi}}^m$
	0.0038	8.0685	7.7095	0.4485	-0.5942	1.6515
Remobilization	c_{ci0}^{rm}	r_{ci}^{rm}	s_{ci}^{rm}	m_{ci0}^{rm}	$r_{rm_{ci}}^m$	$s_{rm_{ci}}^m$
	0.1115	-0.9990	0.0022	0.3215	4.3838	0.4322
	c_{wi0}^{rm}	r_{wi}^{rm}	s_{wi}^{rm}	m_{wi0}^{rm}	$r_{rm_{wi}}^m$	$s_{rm_{wi}}^m$
	0.3092	0.4385	0.1011	0.3648	-0.2173	0.8996
Accumulation	c_{ci}^{ac}		c_{wi}^{ac}			
	0.3071		0.6403			
Interaction Strength	α_{c0}	r_{ac}^G	s_{ac}^G			
	0.1449	0.0535	6.1870			
	α_{w0}	r_{aw}^G	s_{aw}^G			
	0.5974	0.0637	2.8493			
Glide	σ_{v00}	r_v	s_v	m_{v0}	r_v^m	s_v^m
	113.7152	0.4511	0.7361	0.0542	0.3622	3.6393

Density	$\hat{\rho}_{cm}$	$\hat{\rho}_{ci}$	$\hat{\rho}_{wi}$			
	45.5407	40.0124	171.9600			

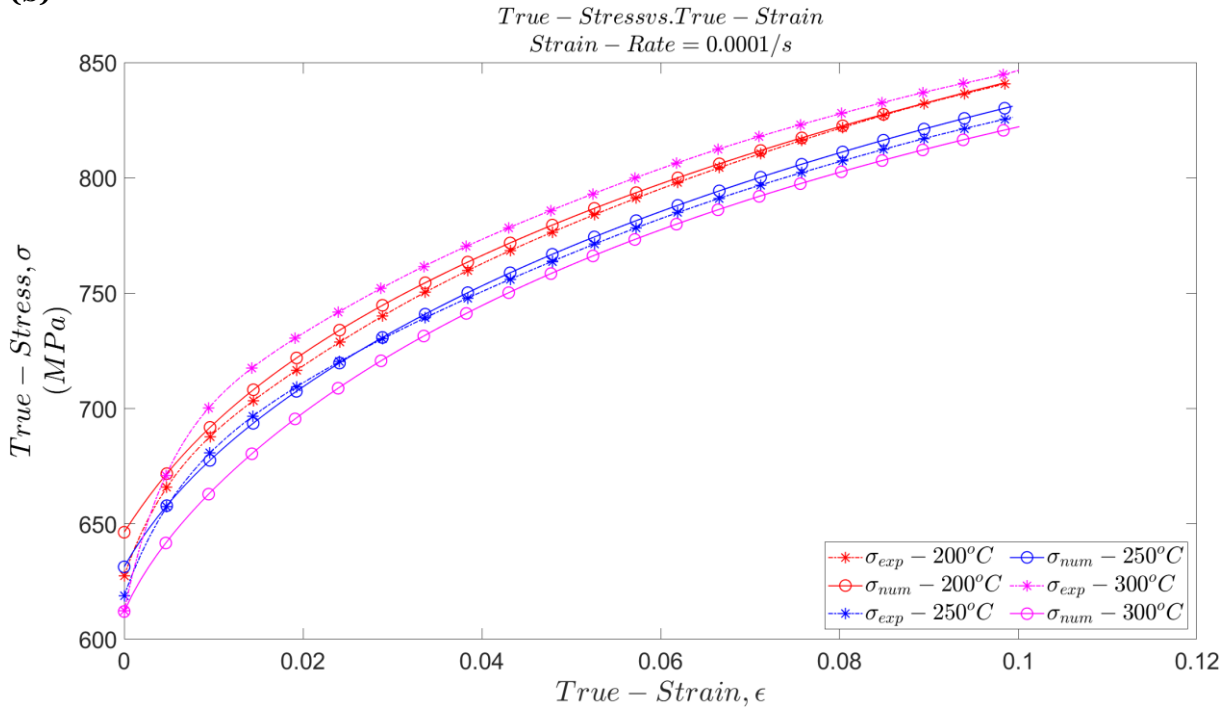
6.2.3: Experimental and Numerical Flow Curve at $0.0001/s$ (The Reference Strain Rate).

The experimental and numerical stress for the strain rate of $10^{-4}/s$ are as presented in the figure below.

(a)



(b)



(c)

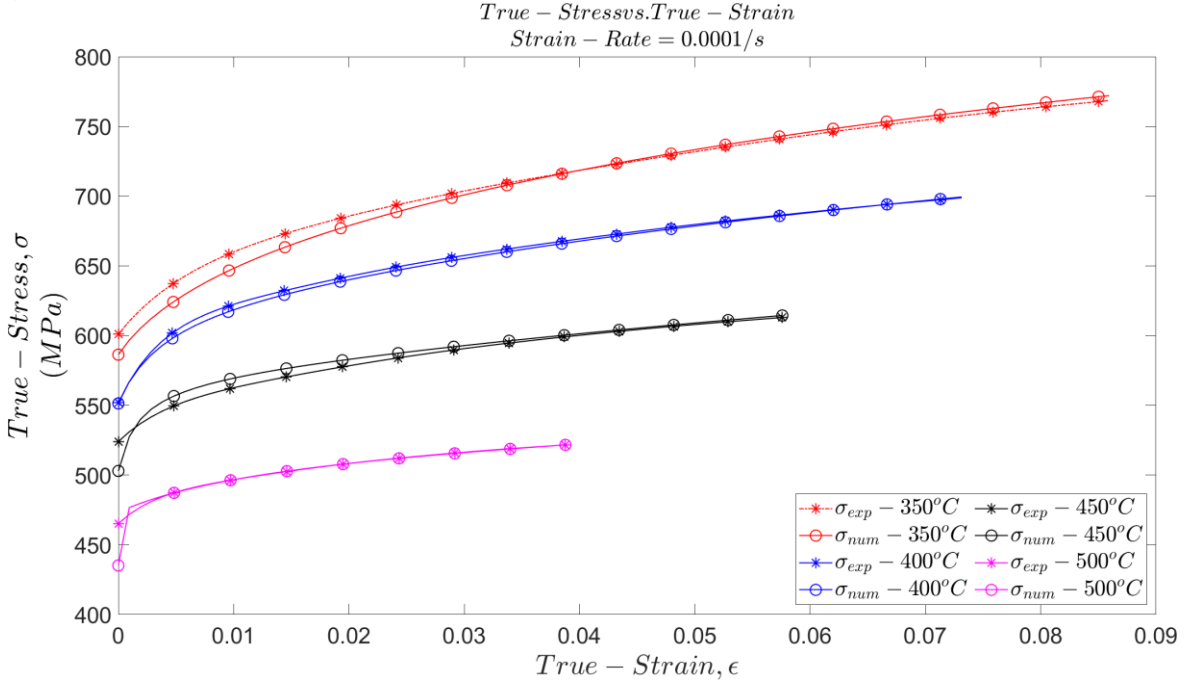
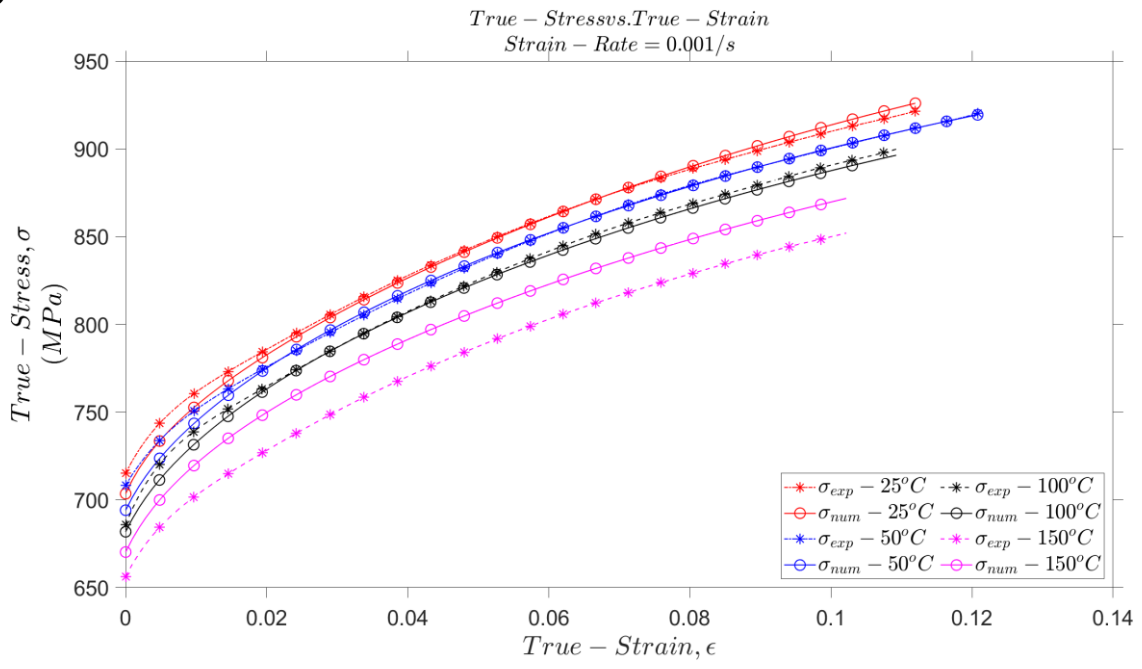


Figure 6.1: Comparative displays of test yield stress and computed stress for 0.0001/s strain rate at all test temperatures.

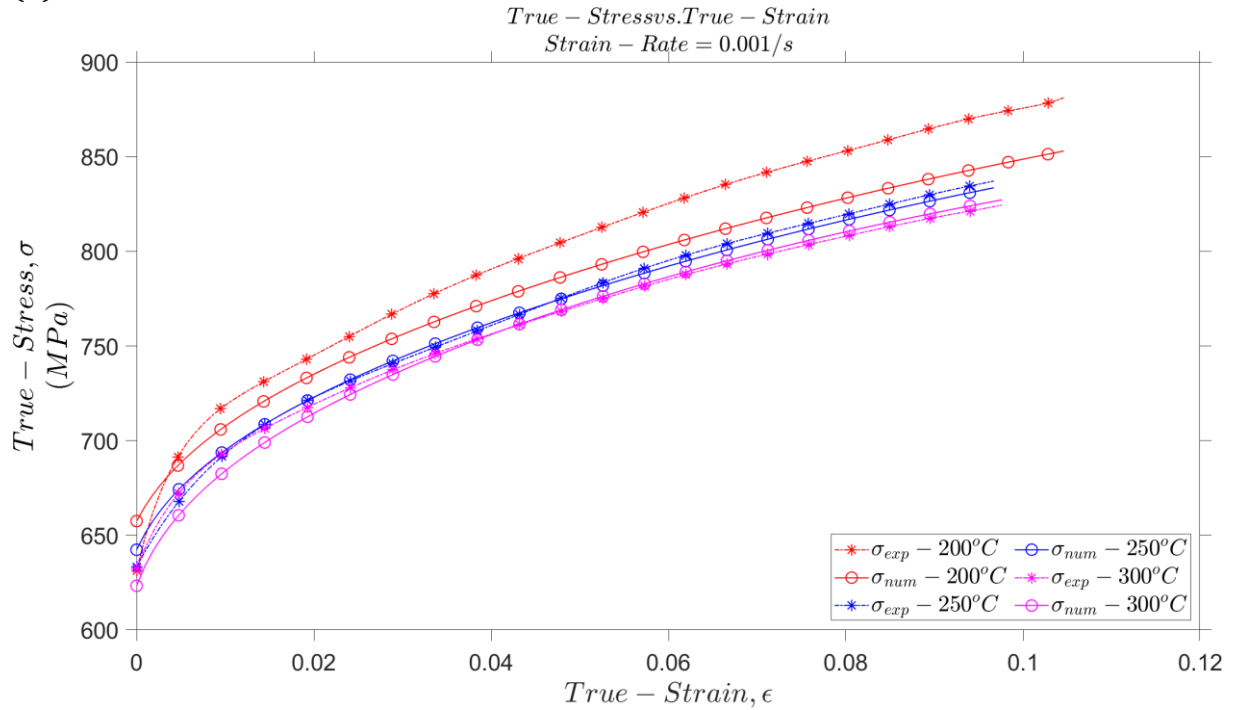
The choice of the division into regions of temperature range is self-evident based on the regularity of experimental results' trend. The same grouping is followed in subsequent curves at higher strain rates.

6.2.4: Experimental and Numerical Flow Curve at 0.001/s.

(a)



(b)



(c)

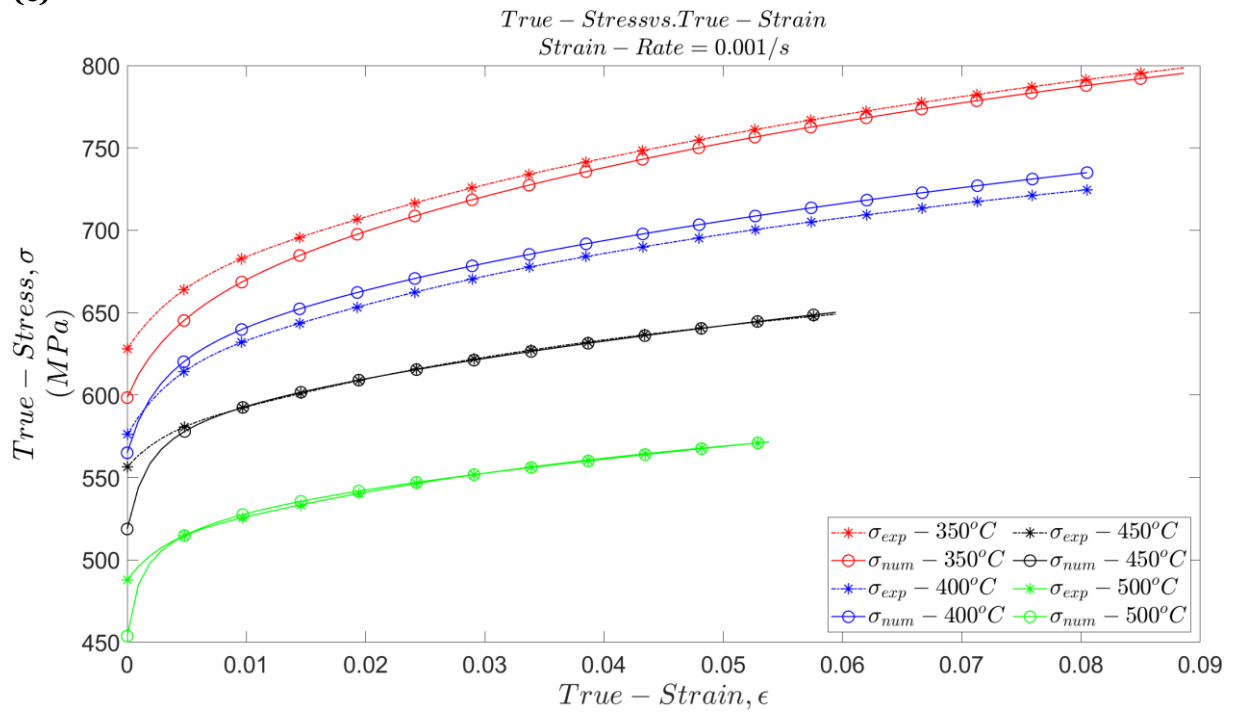
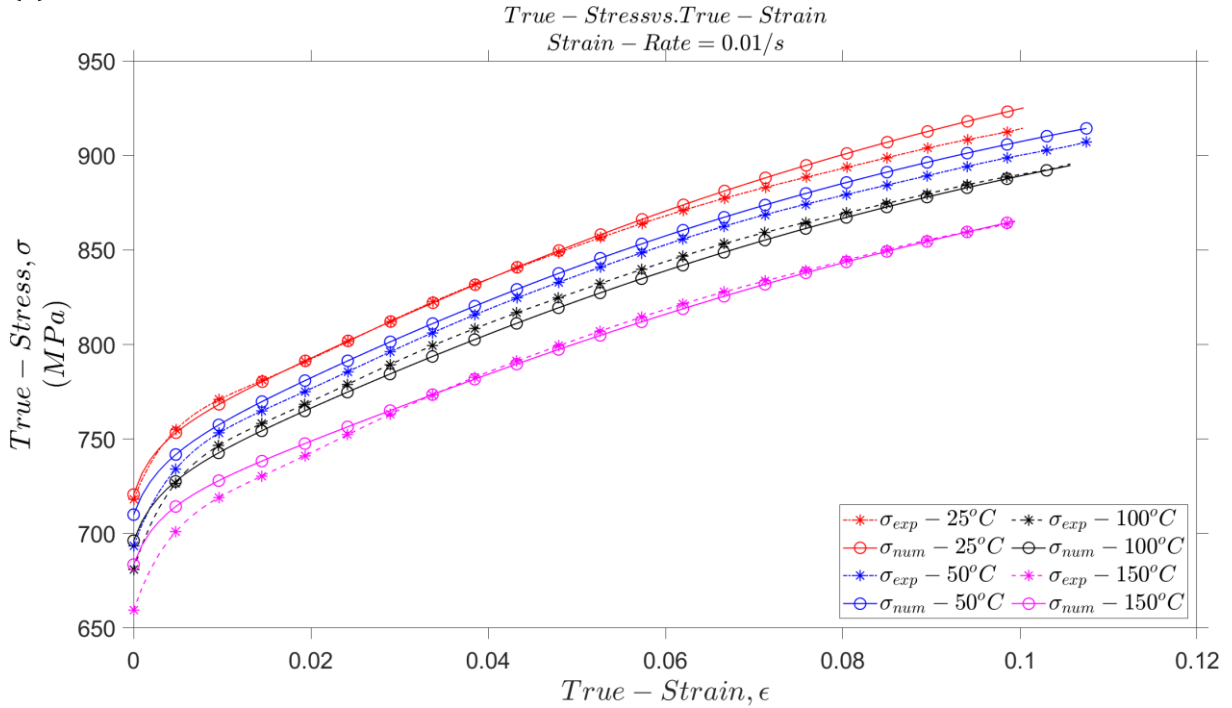


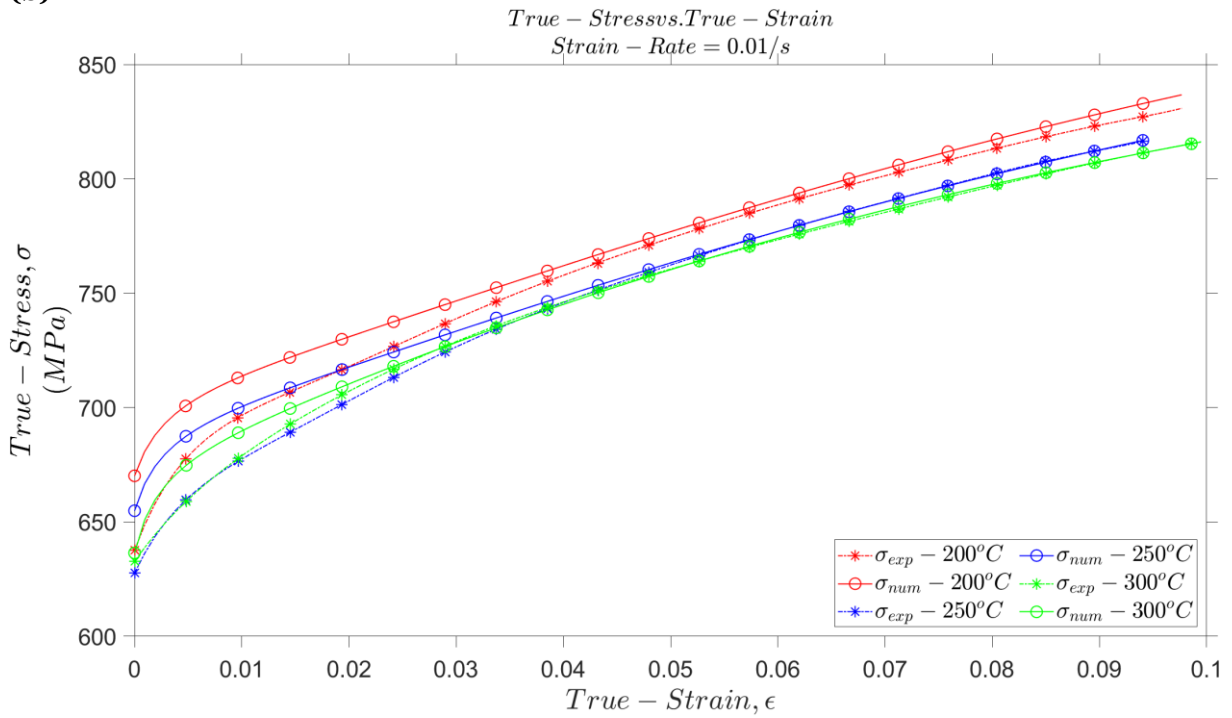
Figure 6.2: Comparative displays of test yield stress and computed stress for 0.001/s strain rate at all test temperatures.

6.2.5: Experimental and Numerical Flow Curve at 0.01/s.

(a)



(b)



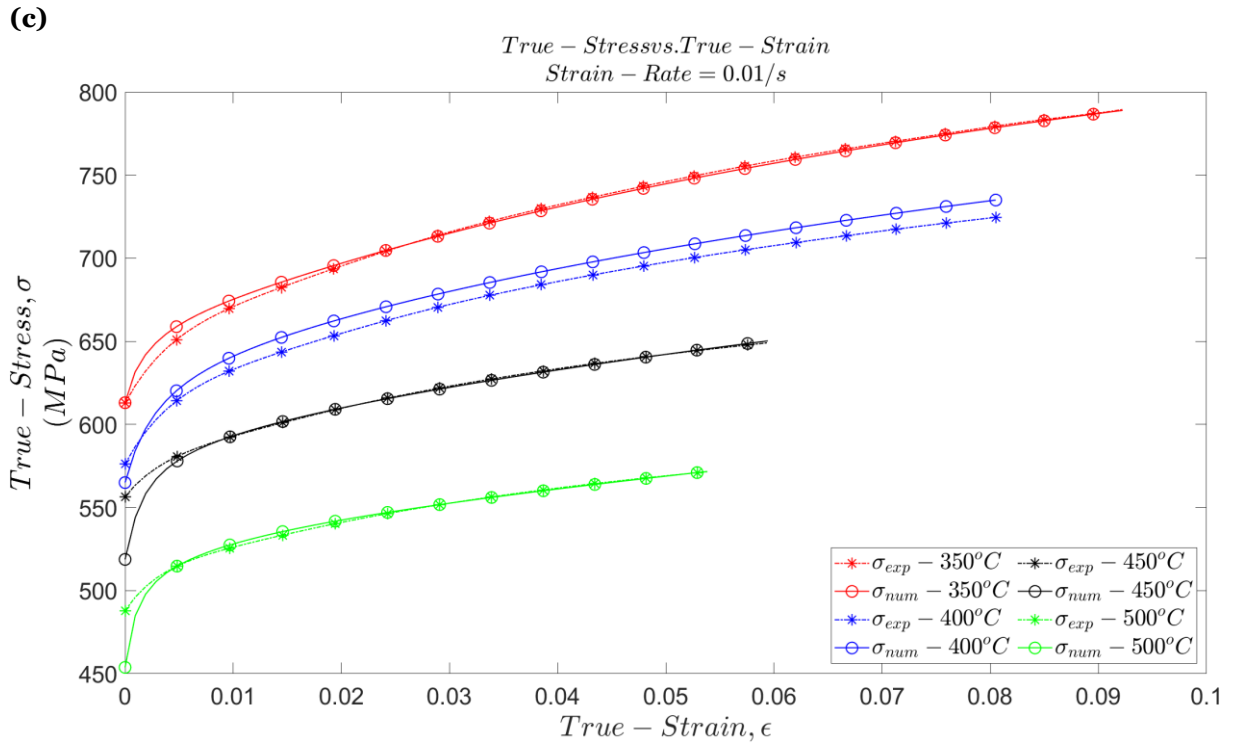
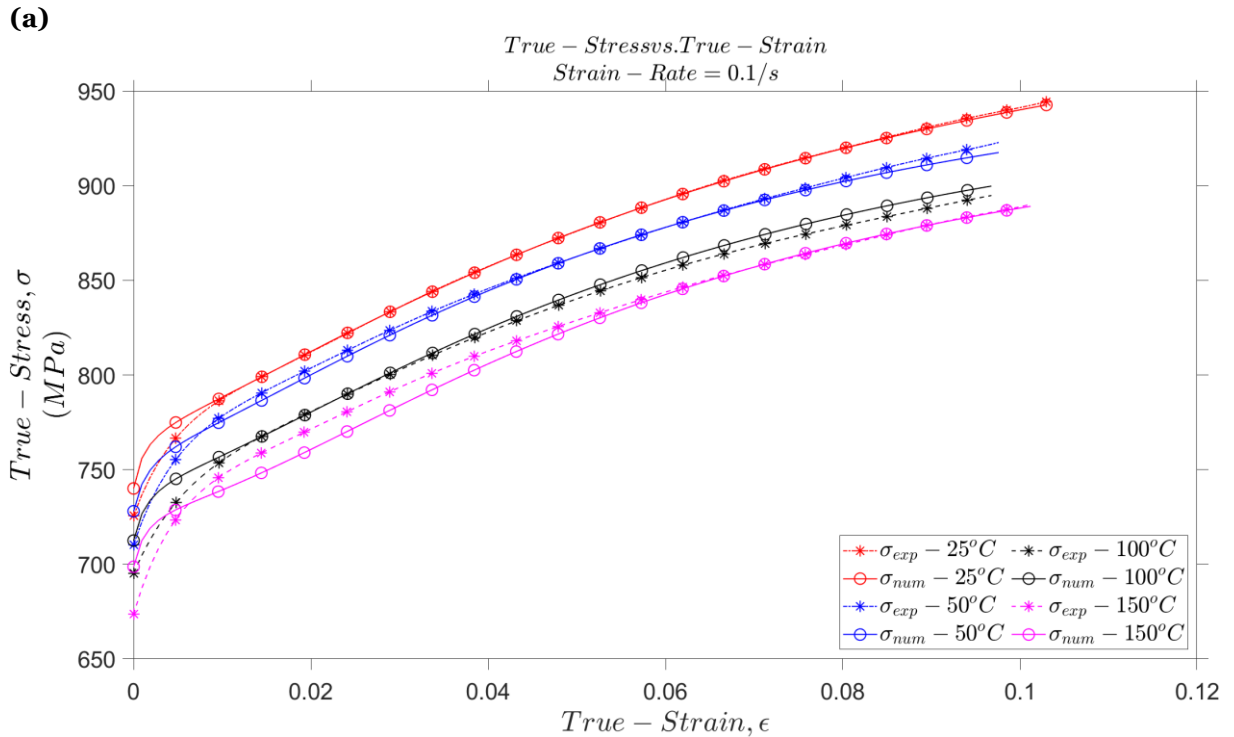
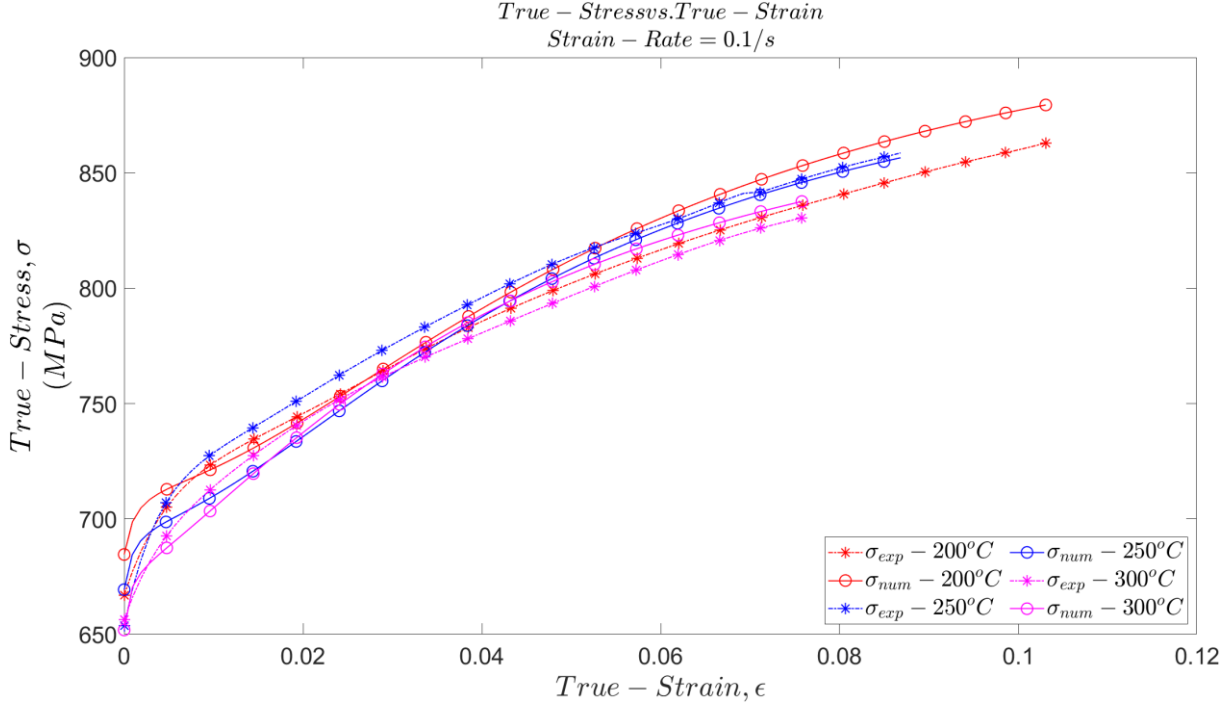


Figure 6.3: Comparative displays of test yield stress and computed stress for 0.01/s strain rate at all test temperatures.

6.2.6: Experimental and Numerical Flow Curve at 0.1/s.



(b)



(c)

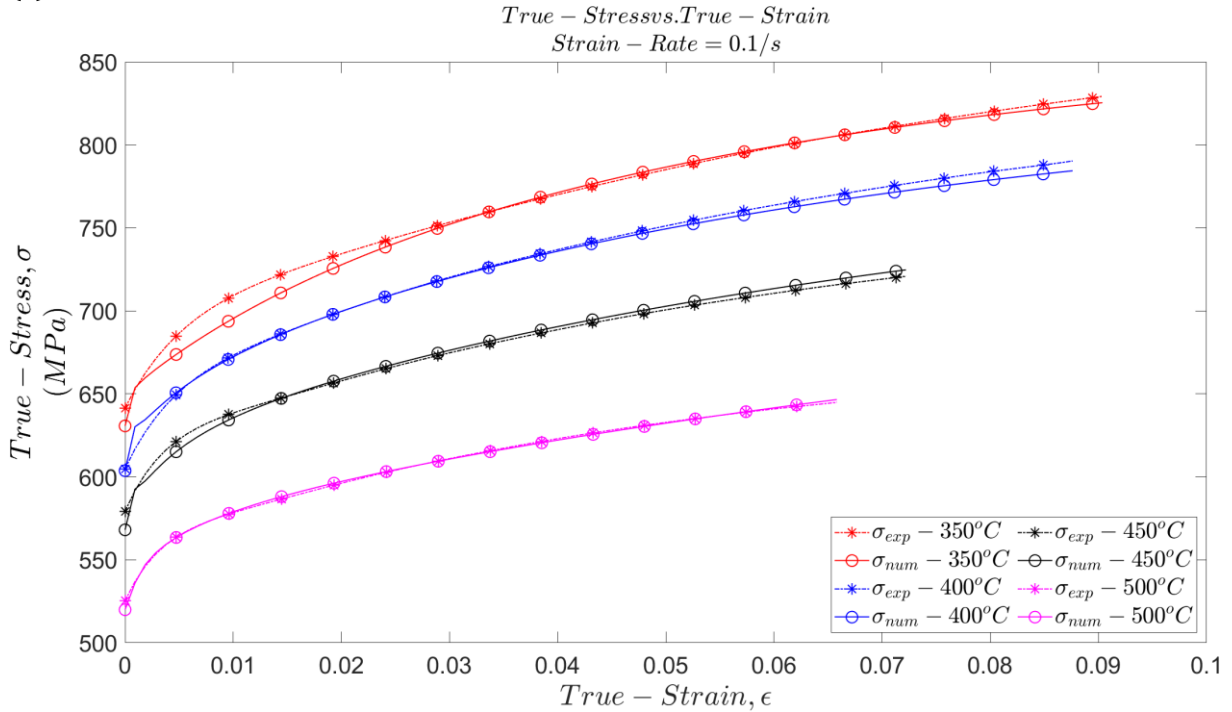


Figure 6.4: Comparative displays of test yield stress and computed stress for 0.1/s strain rate at all test temperatures.

The observed trend in the curves at all strain rate for both the experimentally measured flow stress and numerically obtained flow stress is an increase in the flow stress with

increase in strain i.e. as deformation progresses. The flow stresses also show an inverse variation with temperature at zero true plastic strain, as shown in the figure 6.5 and 6.6 below for the reference temperature. This is maintained, as deformation progresses, for the temperature range $25^{\circ}\text{C} - 150^{\circ}\text{C}$ and $350^{\circ}\text{C} - 500^{\circ}\text{C}$, i.e. conformation to the Cottrell-Stokes' law.

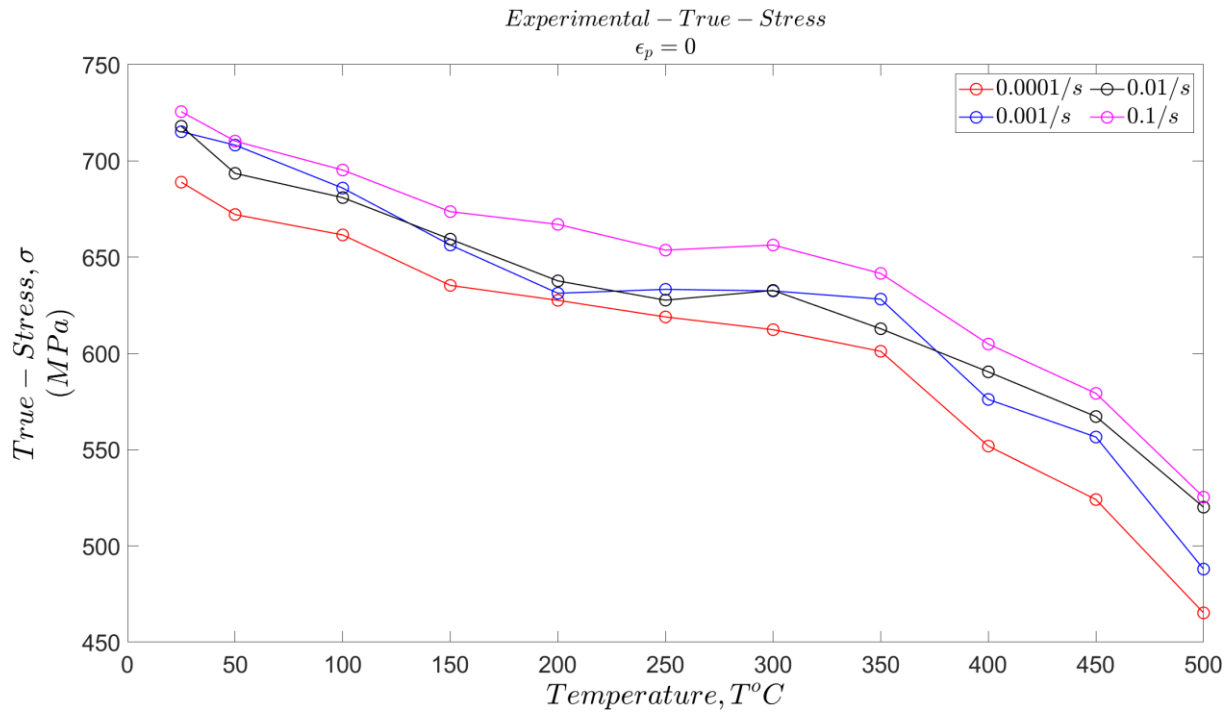


Figure 6.5: Experimental determined yield stress at zero plastic strain across all test temperature and strain rates.

The temperature range of $200^{\circ}\text{C} - 350^{\circ}\text{C}$ show deviation from this behaviour for some strain rates for the experimentally determined flow stress. The computational or numerical stress predicts conformity to Cottrell-Stokes law for all strain rate as shown in figure 6.6.

An observation of the flow curve reveals that at a strain rate of $0.0001/\text{s}$, the flow curve for 300°C is higher than that for 200°C , at a strain rate of $0.001/\text{s}$, the flow curve for 200°C is higher than that for 150°C , at a strain rate of $0.01/\text{s}$, the flow curve for 300°C is very close to that for 250°C , and at strain rate of $0.1/\text{s}$, the flow curve for 250°C is higher than those for 200°C , while the flow curve for 200°C and 300°C overlap. This is

behaviour is understood to be the dynamic strain aging effect (Mishra et al., 1989) resulting from higher concentration of interstitial solute element at dislocation cores and therefore an increase in the viscous stress value. This effect is shown to not influence the strain hardening behaviour. This behaviour is shown to wane with strain rate and strengthen with temperature, however an anomaly is observed in our experimental results since at the highest strain rate of i.e. 0.1/s, an intense effect is obtained while the most intense effect at a strain rate of 0.001/s occurs at lower temperature than for the lower strain rate of 0.0001/s. The effect at the strain rate of 0.001/s and 0.1/s seem to have a consistent interpretation.

The numerical obtained flow curve although captures some effect of the dynamic strain aging i.e. decreased distance between flow curves in the region 200°C – 350 °C, it did not replicate those obtained experimentally.

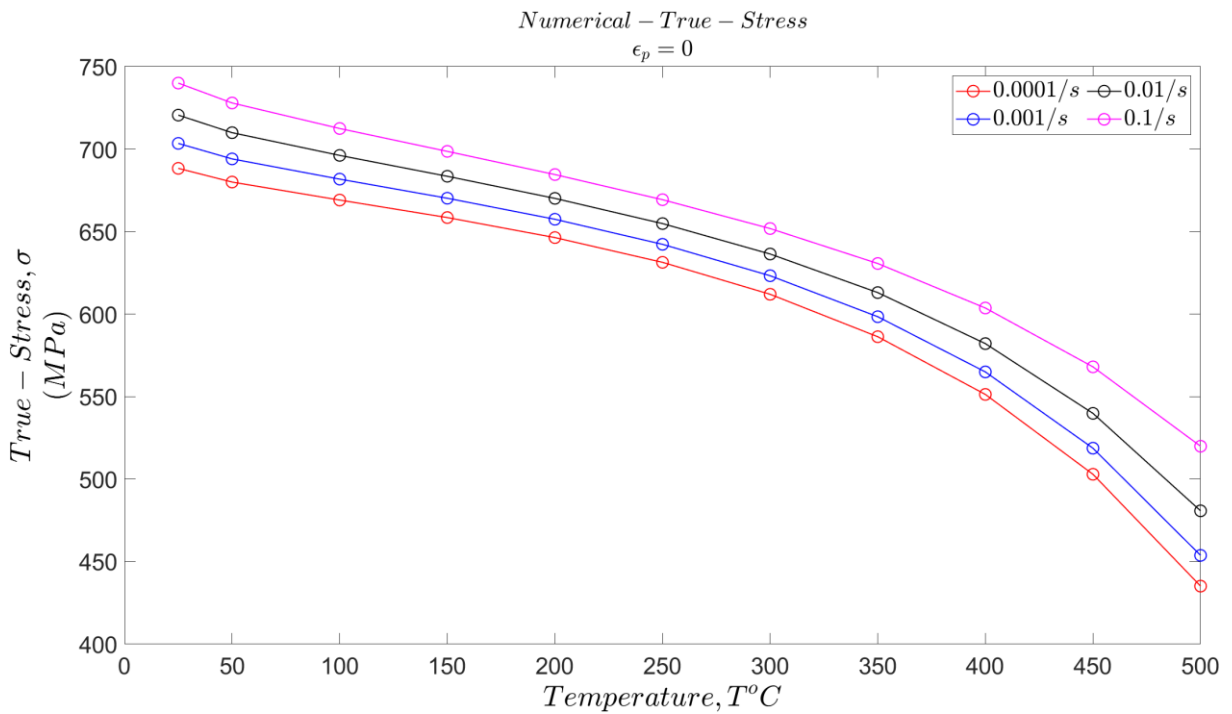


Figure 6.6: Numerically determined yield stress at zero plastic strain across all test temperature and strain rates.

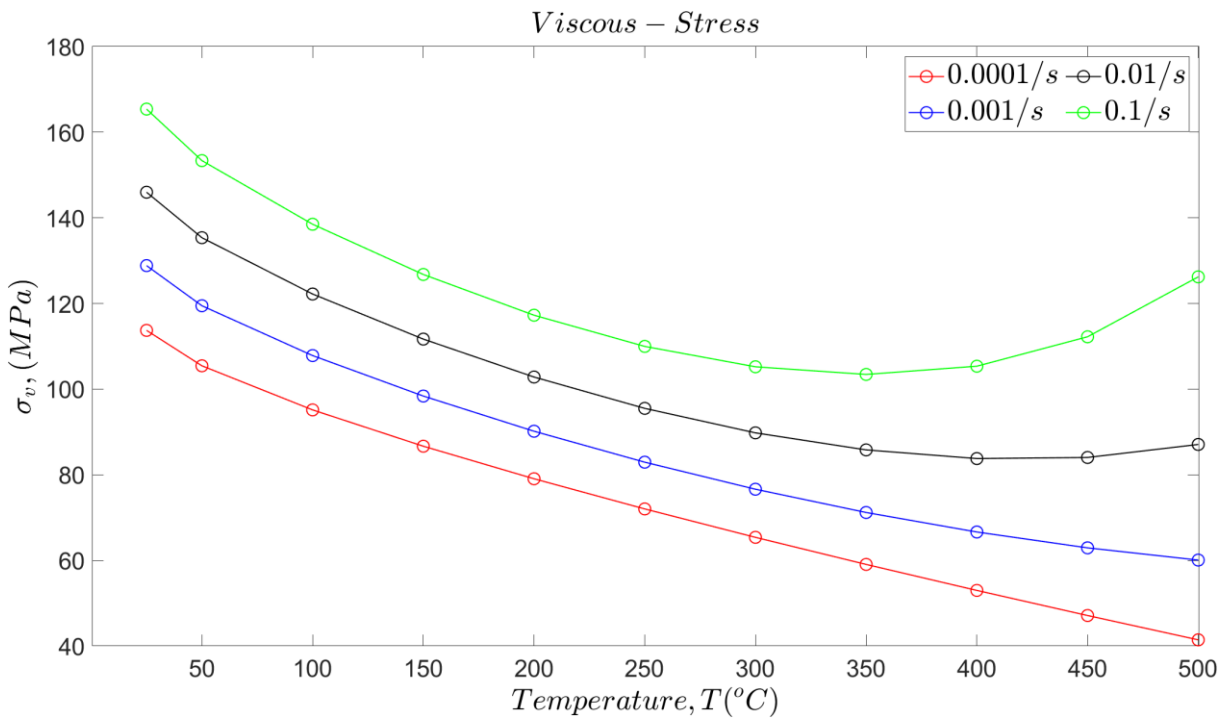


Figure 6.7: Viscous stress as a function of temperature at all test strain rate.

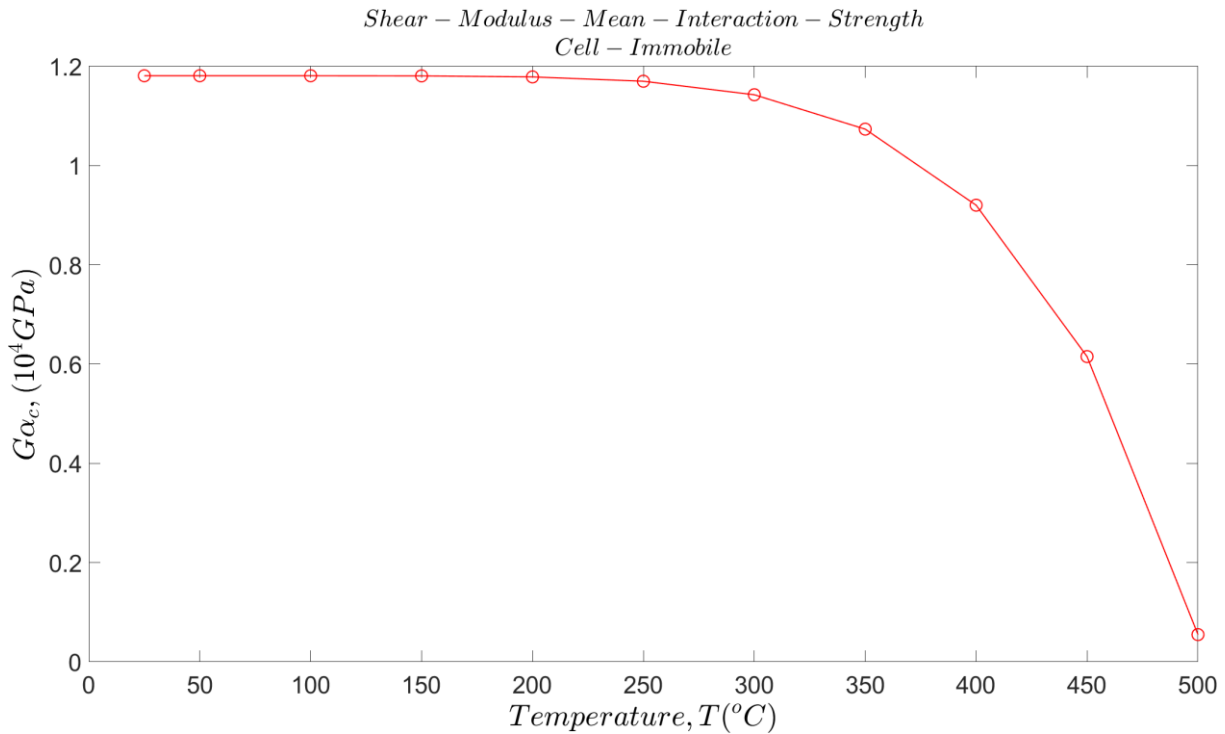


Figure 6.8: Shear-Modulus-Mean-Interaction-Strength for the cell immobile dislocation as a function of temperature.

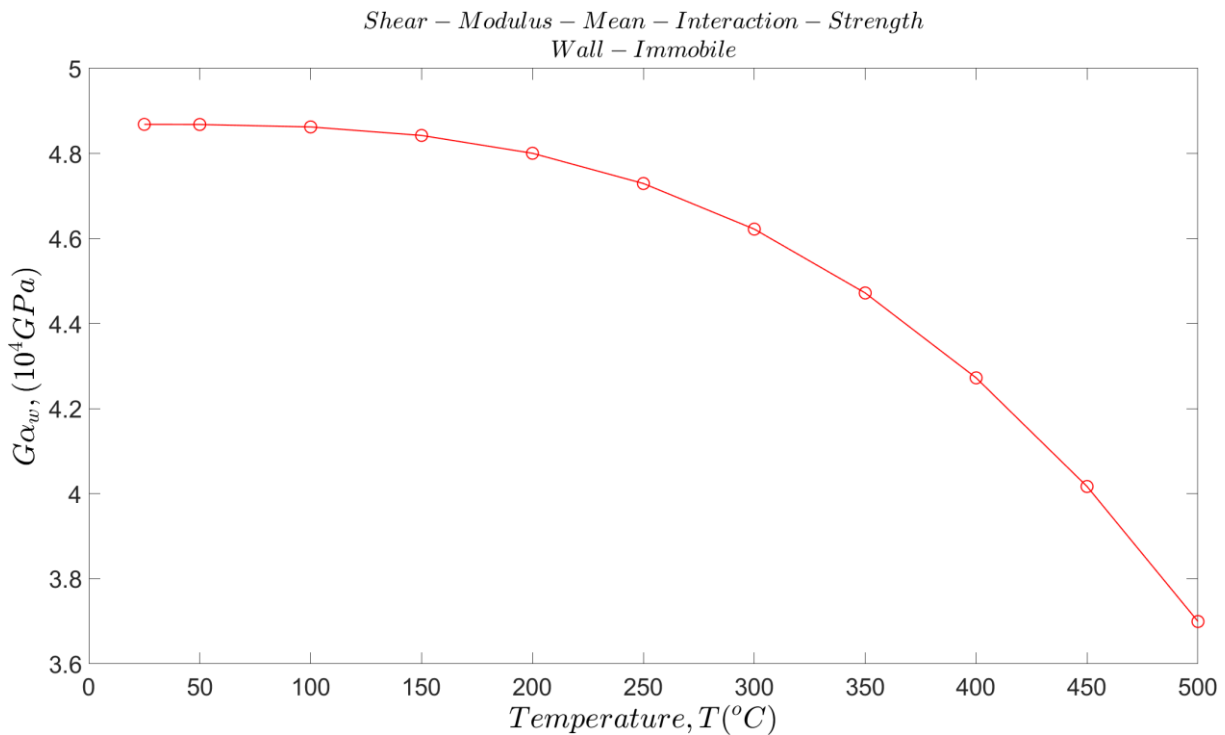


Figure 6.9: Shear-Modulus-Mean-Interaction-Strength for the wall immobile dislocation as a function of temperature.

The trend of decreasing flow stress at zero plastic strain with increasing temperature is ascribed to the viscous stress, which has been shown to decrease with temperature, and the effect of the decreasing interaction strength value with increasing temperature, since all the test material at different test temperature have the same starting dislocation density. Also the increased flow stress with strain rate is due to the viscous stress. The numerically obtained viscous stress and interaction strength as a function of temperature is shown in the diagrams figures 6.7, 6.8, & 6.9.

It is noteworthy to observe the trend in the viscous stress at strain rates of 0.01/s and 0.1/s, where the viscous stress curve show a minimum value at different temperature depending on the strain rate. Experimental determination of viscous stress has shown that this decreases to values close to zero at high and increasing high temperatures (Brunner & Diehl, 1991b; Dingley & McLean, 1967), since strain rate effects are involved in determining the viscous stress, the existence of a minimum at high strain

rate is consistent especially if the strain rate sensitivity parameter in figure 6.10 below is considered.

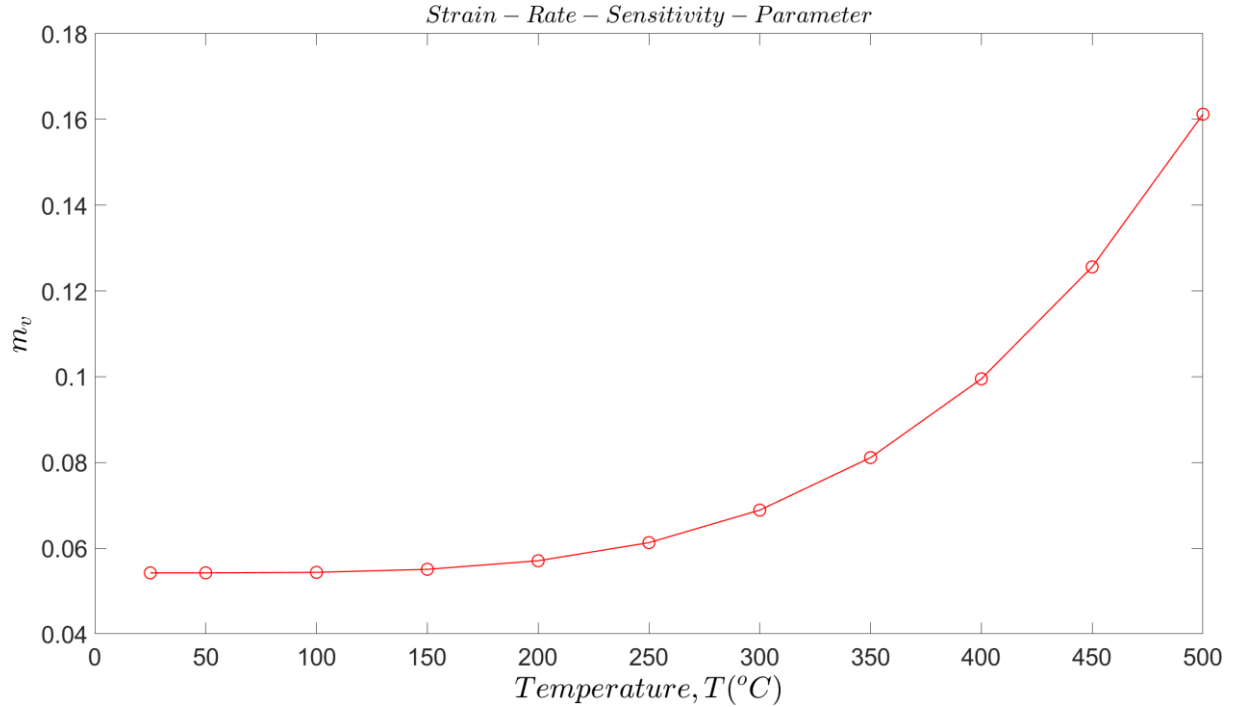


Figure 6.10: Strain rate sensitivity parameter of the viscous stress as a function of temperature.

Following figure 4.2 for the variation of the viscous stress with temperature at constant strain rates one may mathematically prove, using the Kocks power law proposition for the rate dependence of the flow stress, the increase in strain rate sensitivity by the consideration as given below:

$$\text{Let } \sigma_2(T^1, \dot{\epsilon}_2) > \sigma_1(T^1, \dot{\epsilon}_1) > \sigma_4(T^2, \dot{\epsilon}_2) > \sigma_3(T^2, \dot{\epsilon}_1)$$

$$\text{Where } \dot{\epsilon}_2 > \dot{\epsilon}_1 \text{ and } T^1 < T^2$$

Based on Kocks power law:

$$\sigma_2 = \sigma_1 \left(\frac{\dot{\epsilon}_2}{\dot{\epsilon}_1} \right)^{m_1}$$

$$\sigma_4 = \sigma_3 \left(\frac{\dot{\epsilon}_2}{\dot{\epsilon}_1} \right)^{m_2}$$

$$\frac{\log\left(\frac{\sigma_2}{\sigma_1}\right)}{\log\left(\frac{\sigma_4}{\sigma_3}\right)} = \frac{m_1}{m_2}$$

Based on the curves in figure 4.2

$$\sigma_2 > \sigma_1 > \sigma_4 > \sigma_3 \text{ And } (\sigma_2 - \sigma_1) < (\sigma_4 - \sigma_3)$$

Therefore

$$\frac{\sigma_2}{\sigma_1} < \frac{\sigma_4}{\sigma_3}$$

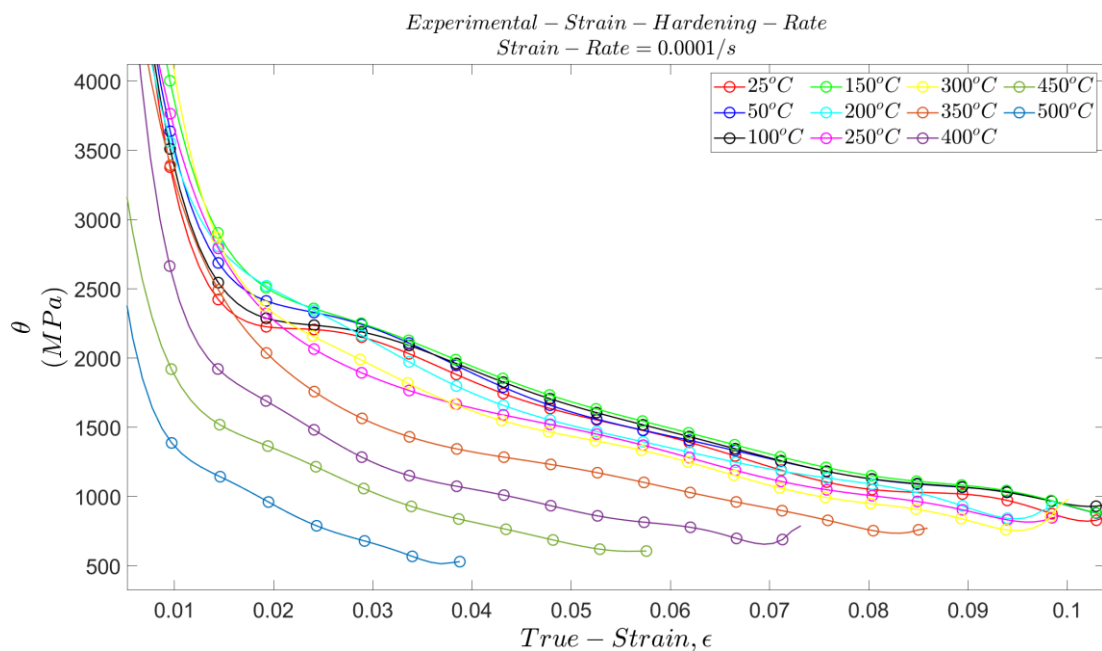
Which follows from preceding equations that

$$\frac{m_1}{m_2} < 1$$

6.3: Strain Hardening Rate at all Test Strain Rate & Temperatures.

Hardening is observed for all test temperature and strain rate as plastic strain develops and progresses as shown in the figures 6.11, 6.12, & 6.13, 6.14. This correlates with increasing density of the immobile dislocation densities whose evolution will be shown in subsequent chapters.

(a)



(b)

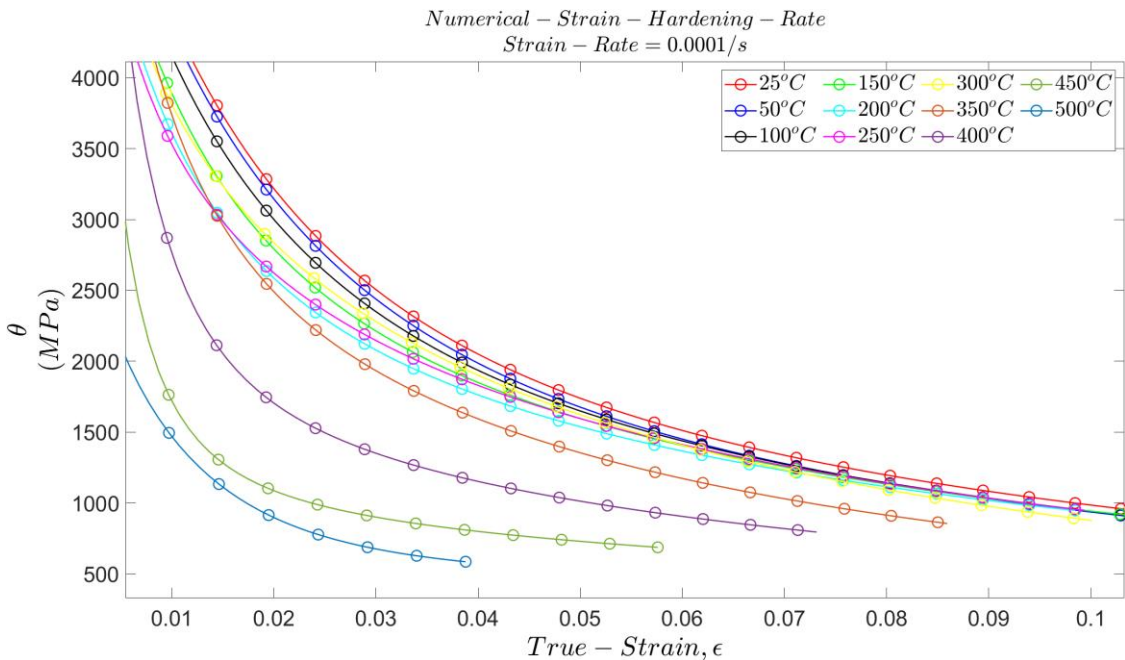
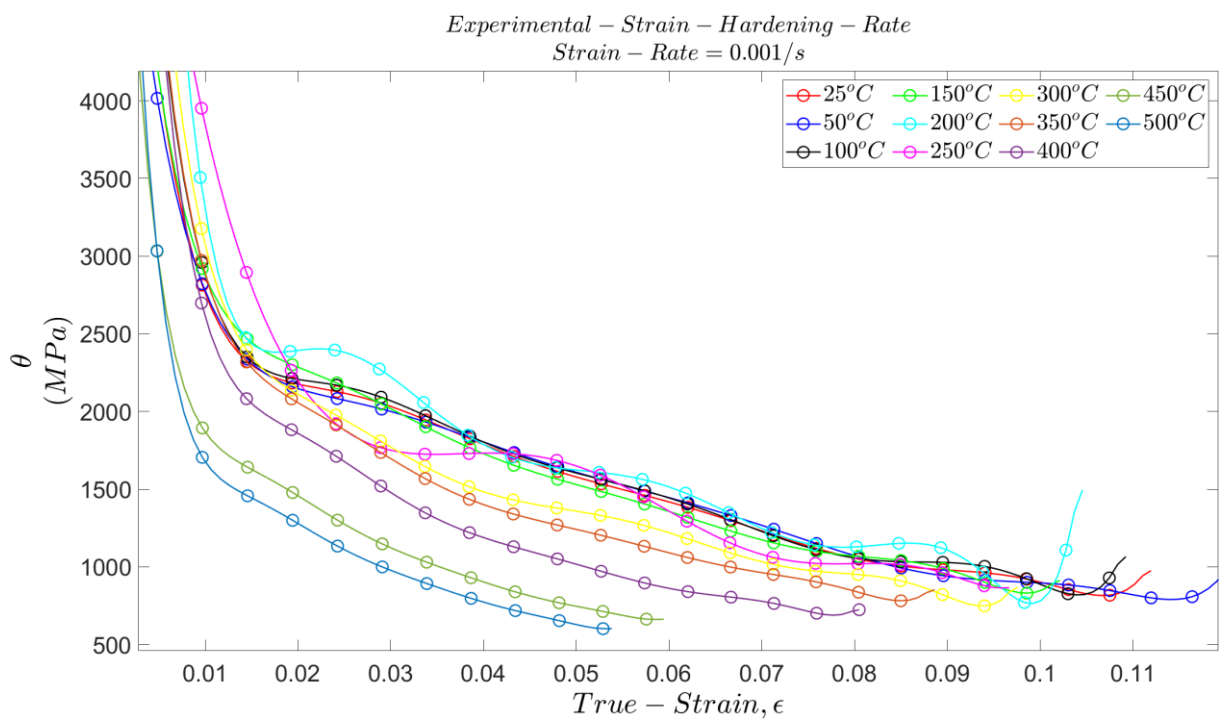


Figure 6.11: Experimental (a), and numerical (b), strain hardening rate for all temperatures at a strain rate of 0.0001/s.

(a)



(b)

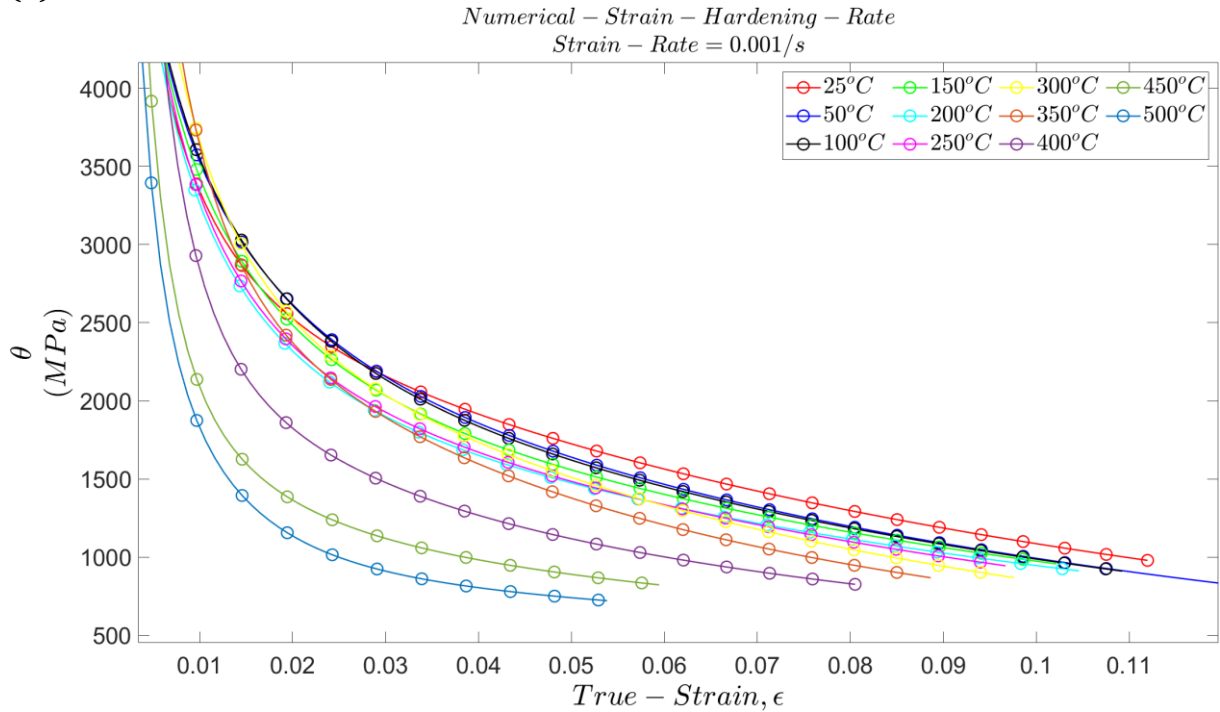
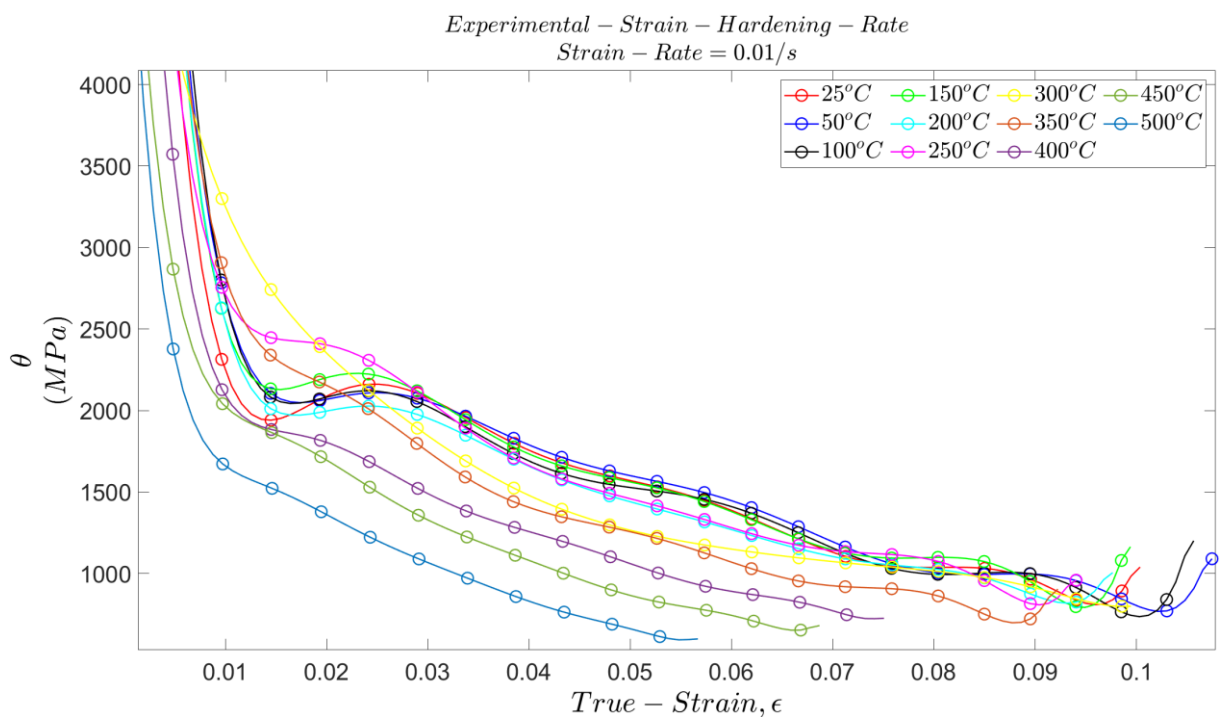


Figure 6.12: Experimental (a), and numerical (b), strain hardening rate for all temperatures at a strain rate of 0.001/s.

(a)



(b)

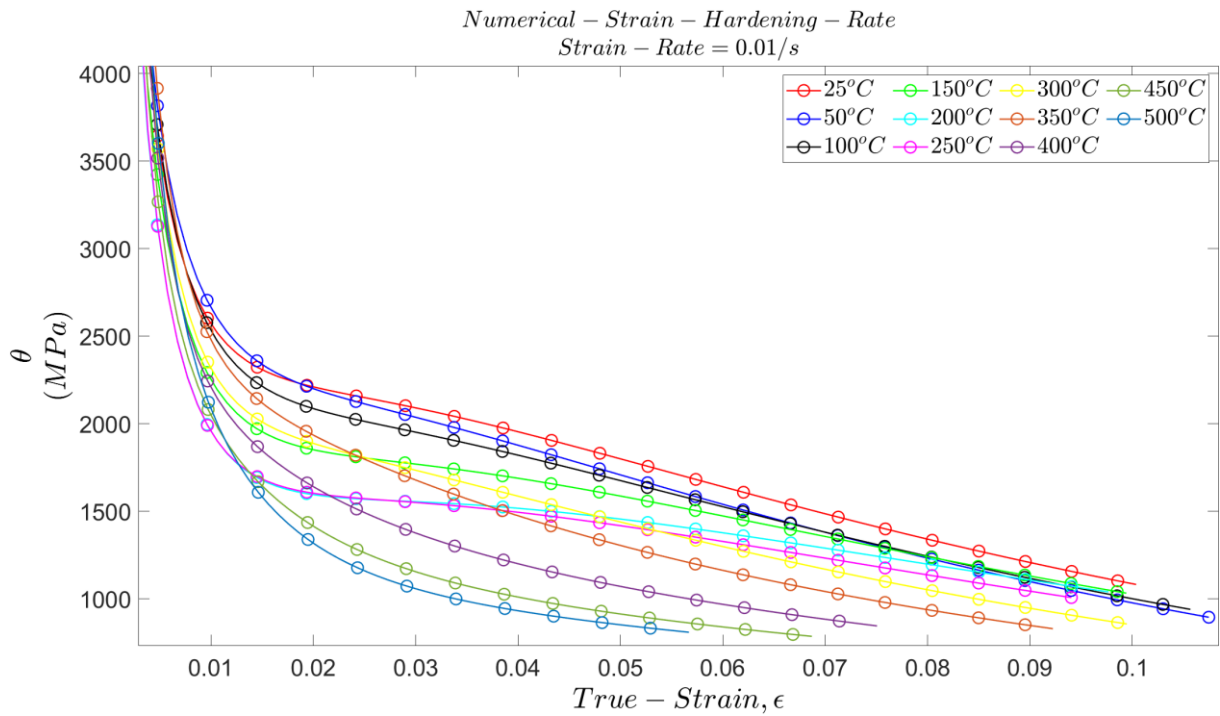
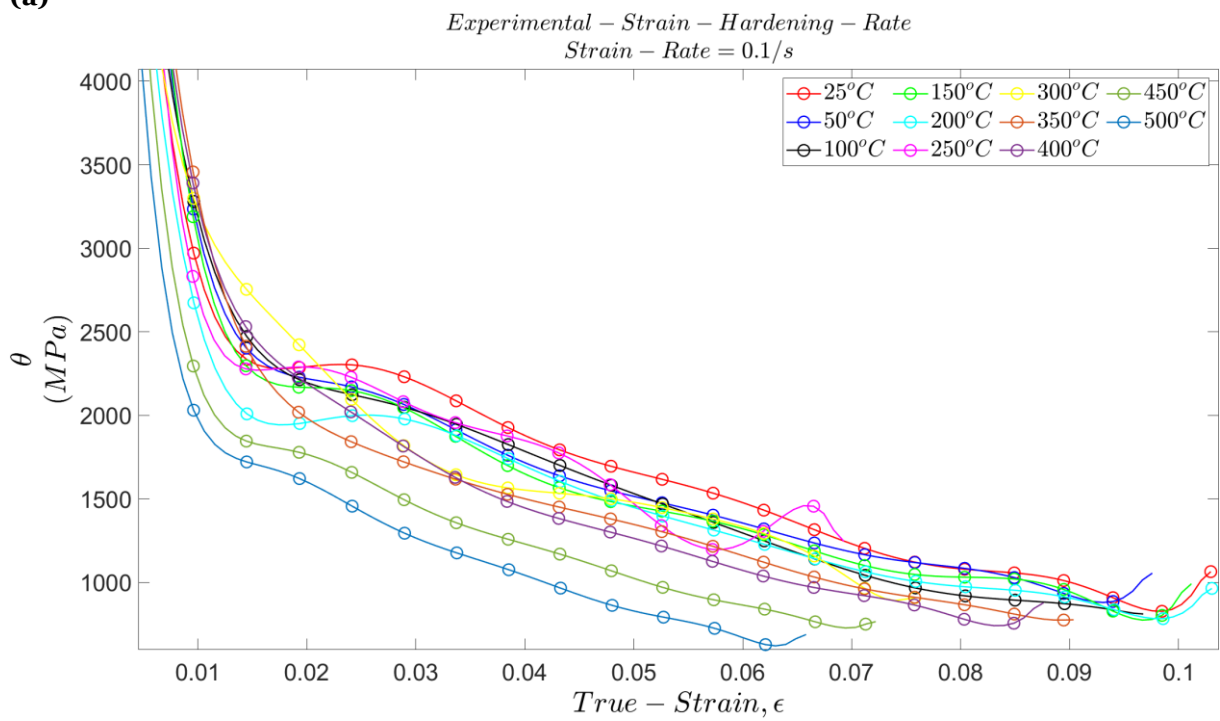


Figure 6.13: Experimental (a), and numerical (b), strain hardening rate for all temperatures at a strain rate of 0.01/s.

(a)



(b)

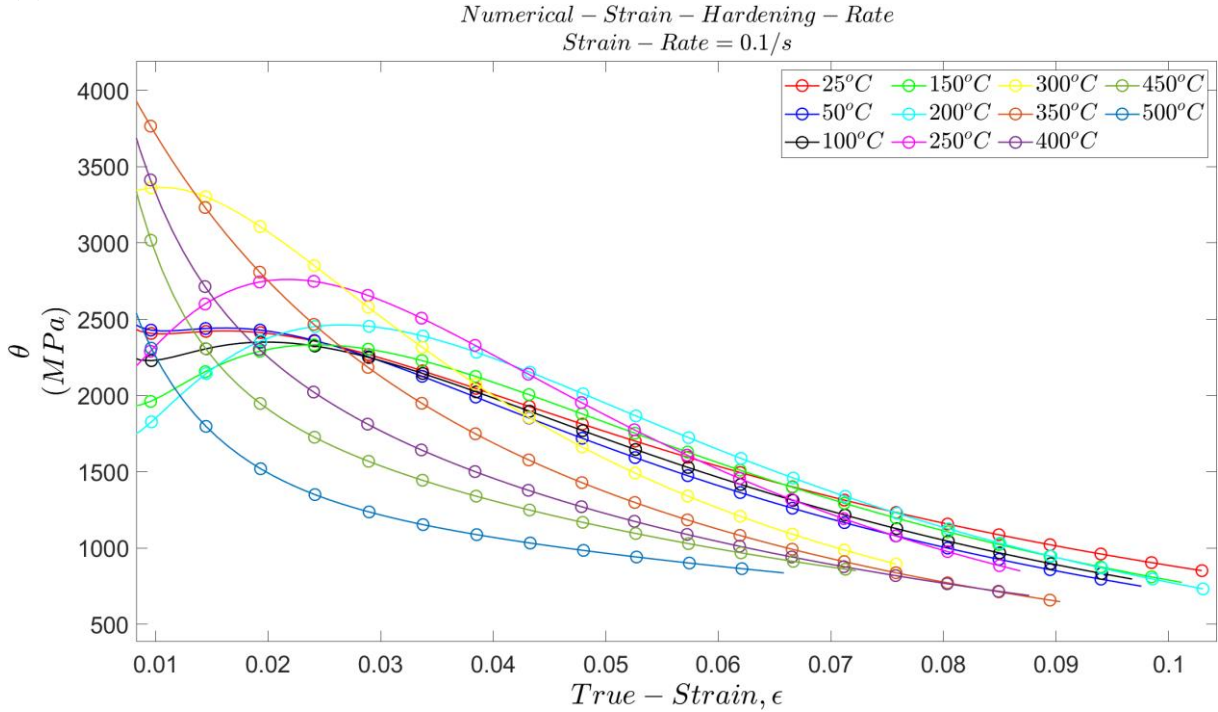


Figure 6.14: Experimental (a), and numerical (b), strain hardening rate for all temperatures at a strain rate of 0.1/s.

The experimentally determined and numerically obtained strain hardening rate drops off precipitously from an initial high value of the fresh material to low value which is maintained with a lower drop rate throughout the rest of the deformation. The stain hardening rate drops as plastic deformation progresses due to an increasing exhaustion of plastic potential of the material. This registers physical as a decreasing rate of increase of the total dislocation density as plasticity progresses.

In general, the experimental strain hardening rates at high temperatures are lower than those at low temperatures due to the increased occurrence of annihilation events/processes at higher temperatures (Rollett & Kocks, 1993). The clustering of experimental strain hardening rate at temperatures in the range of 25°C – 200 °C, where there is only little observable difference between higher and lower temperatures strain hardening rate shows that the material strain hardening behaviour may be quite stable within this temperature range i.e. the annihilation processes show no significant effect within the temperature range. Also it could mean that dynamic strain aging

processes are occurring fast enough to pin dislocation, forming dislocation generation effects which has a counter effect to increased annihilation events at higher temperature resulting in less decreased decrease in strain hardening.

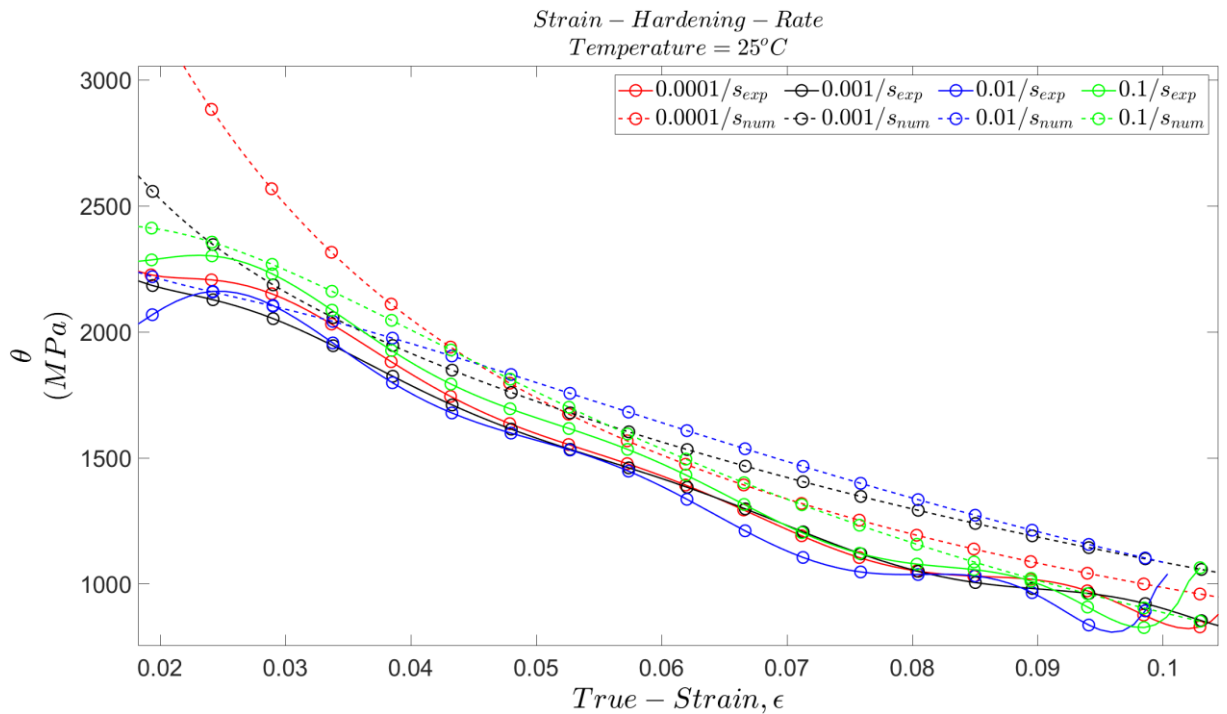
Various individual deviations from the generality occur especially for temperatures within the region $200^{\circ}\text{C} - 300^{\circ}\text{C}$, where in some cases the strain hardening rate within this region are found to be comparable or exceed those of the lowest test temperatures. If dynamic strain aging effects are optimal within these regions and the pinning effects lead well to generation of dislocations such that the annihilation events are largely overcome compared to those at lower temperatures, one may see why strain hardening within these regions are comparable or exceeding those at lower temperatures.

The numerical strain hardening rate (i.e. the model's prediction) on the other hand predicts somewhat a more uniform and consistent generality and distinguishable strain hardening rate behaviour across temperatures. It also captures some clustering at high strain, and some deviation in the same temperature range as already shown by the experimental values.

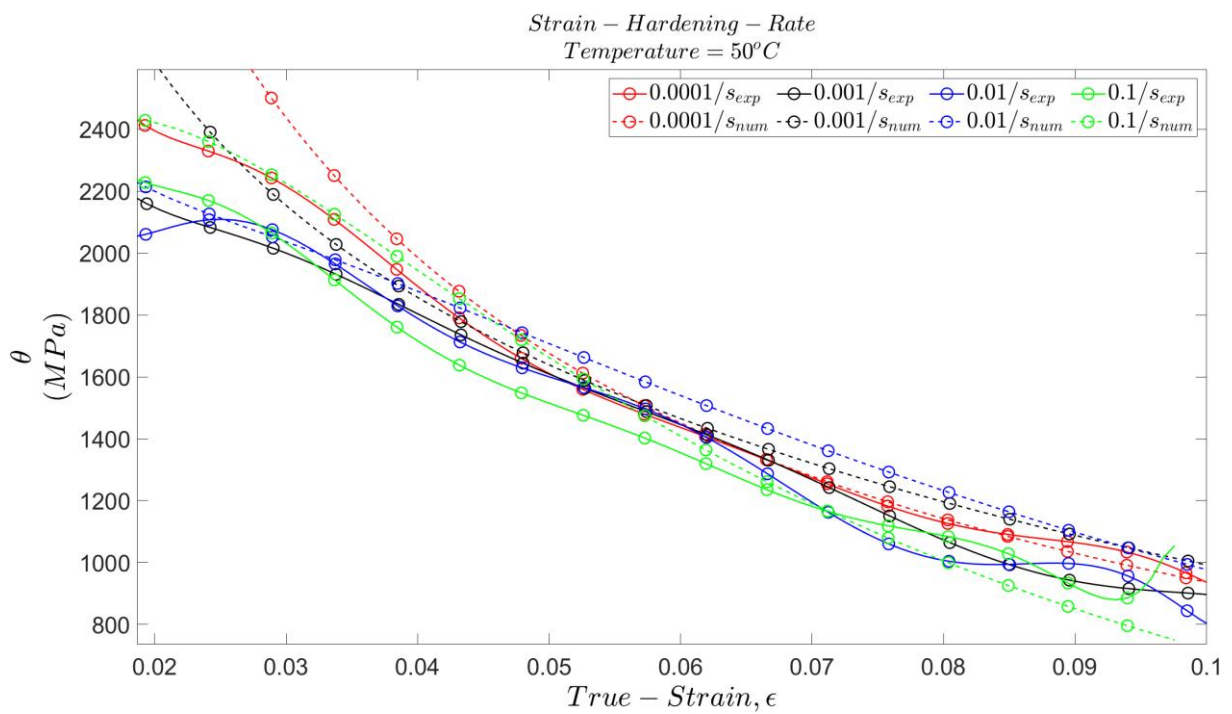
It is worth noting that the just described behaviour applies to plastic strains greater than 2%. For plastic strains less than 2%, no attempt is made to describe the behaviour because of the nature of the experimental values obtained from measurements.

To compare the strain hardening behaviour across strain rate only the data at specific temperatures are considered. From the constituent figures in figure 6.15, no observable consistency exist for the strain hardening rate at all test strain rates for the experimental values, also the numerical values show no consistent behaviour in relation to the strain rate and differs somewhat from the experimental values. This differs from what has been established in literature ([Lennon & Ramesh, 2004](#); [Rusinek et al., 2007](#)) where strain hardening rate is shown to increase with lower strain rate.

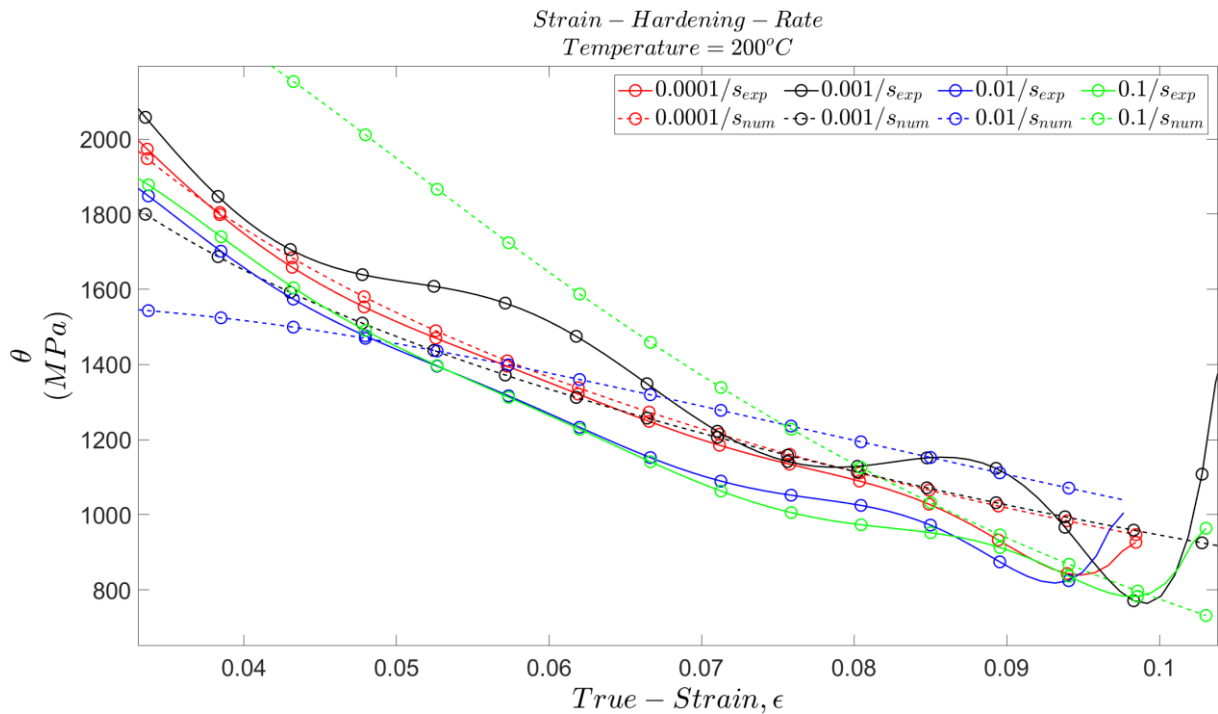
(a)



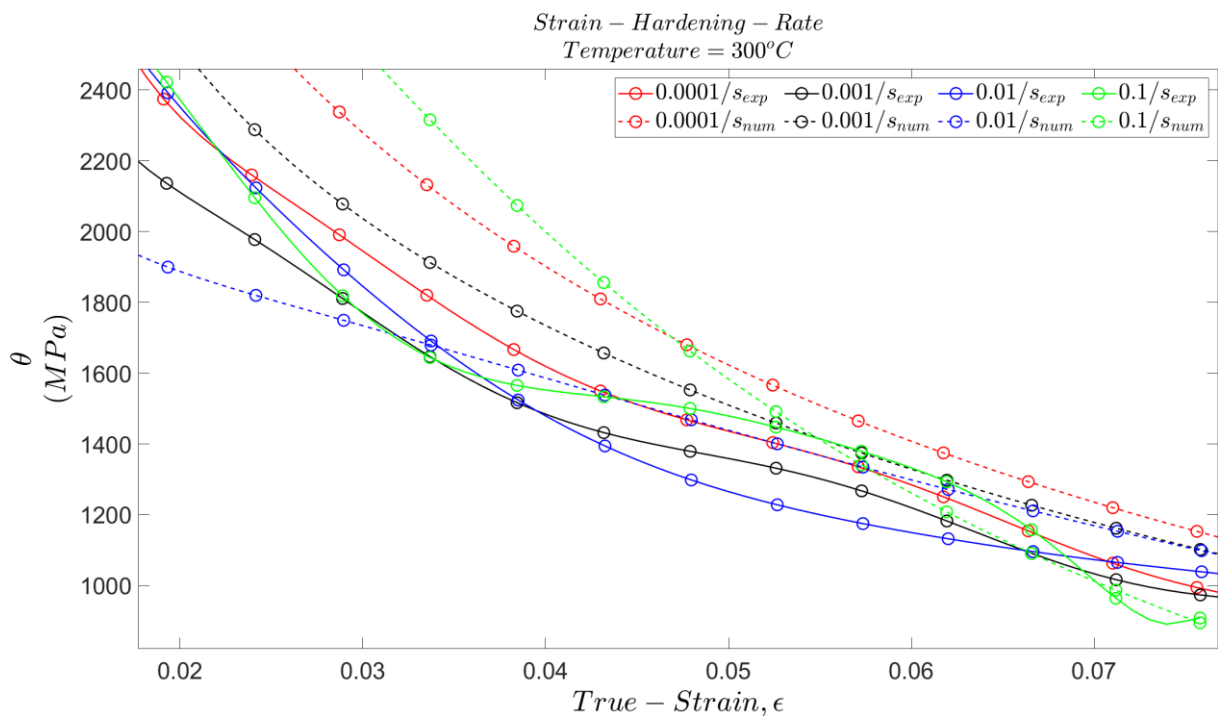
(b)



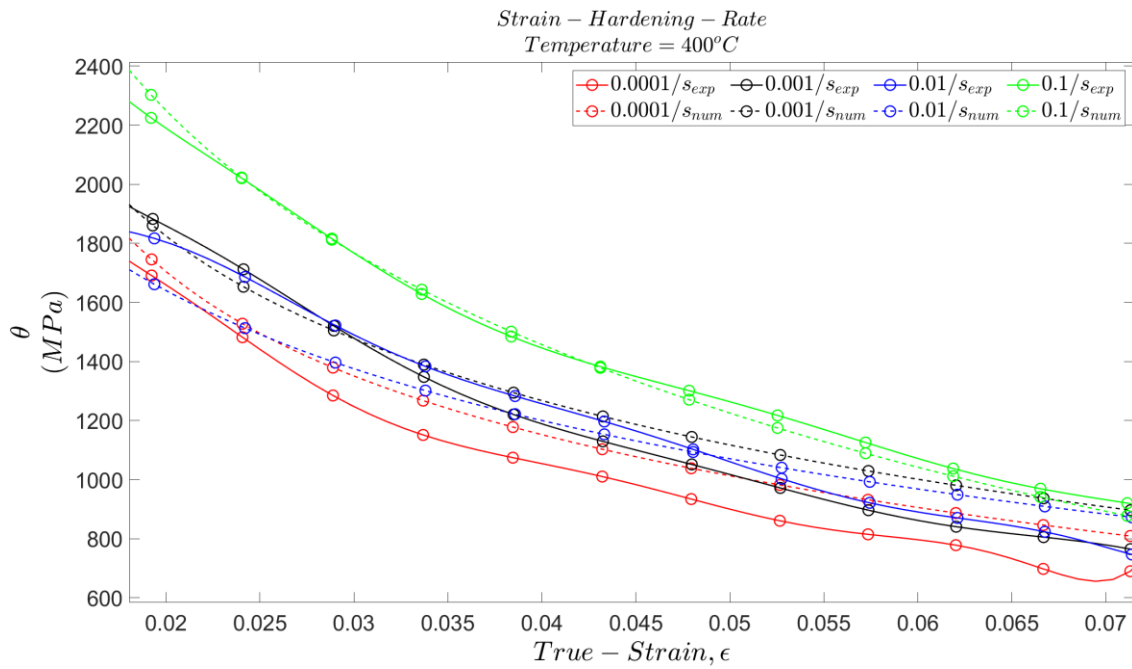
(c)



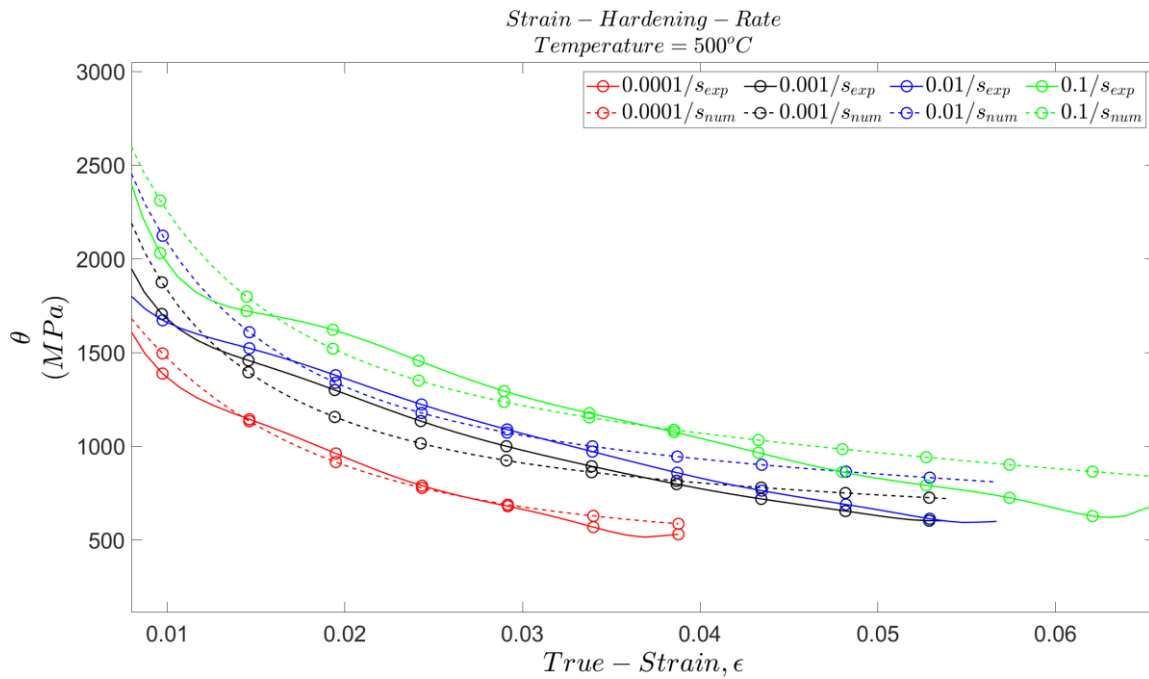
(d)



(e)



(f)

**Figure 6.15:** Strain hardening rate at all test strain rate and temperatures.

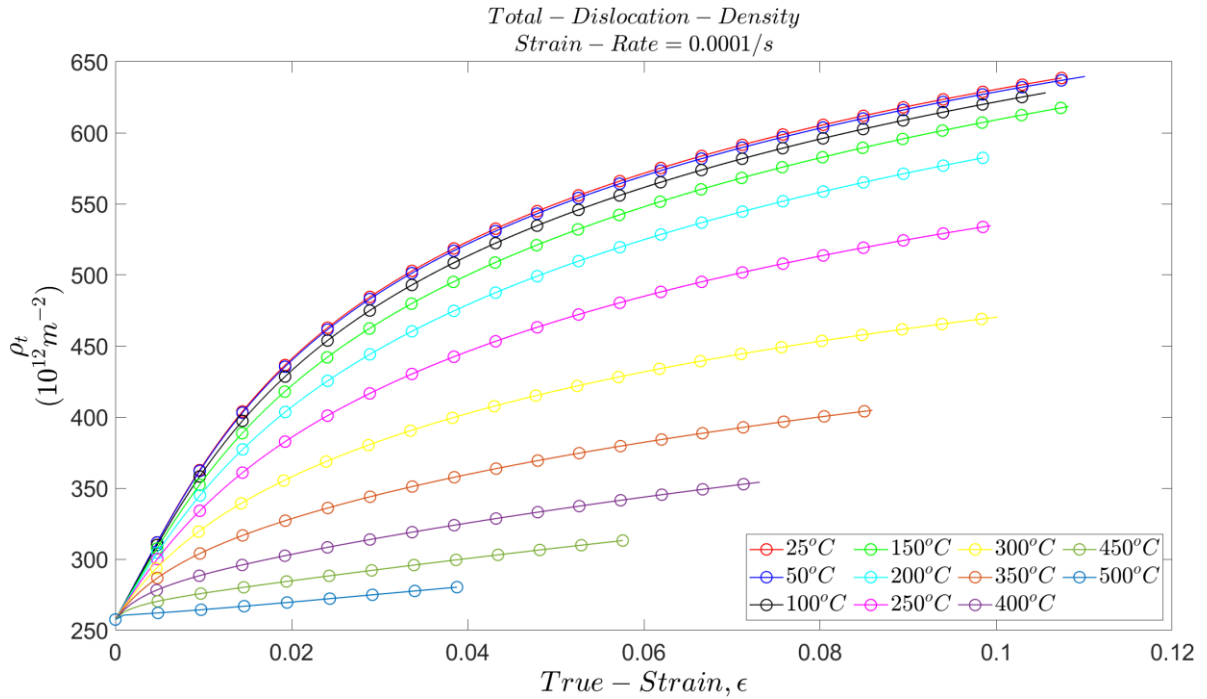
In some cases, figure 6.15e and f, where observable difference exist, strain rate is proportional to strain hardening rate, in opposition to established experimental knowledge of inverse proportionality between strain rate and strain hardening rate.

6.4: Dislocation Density Evolution

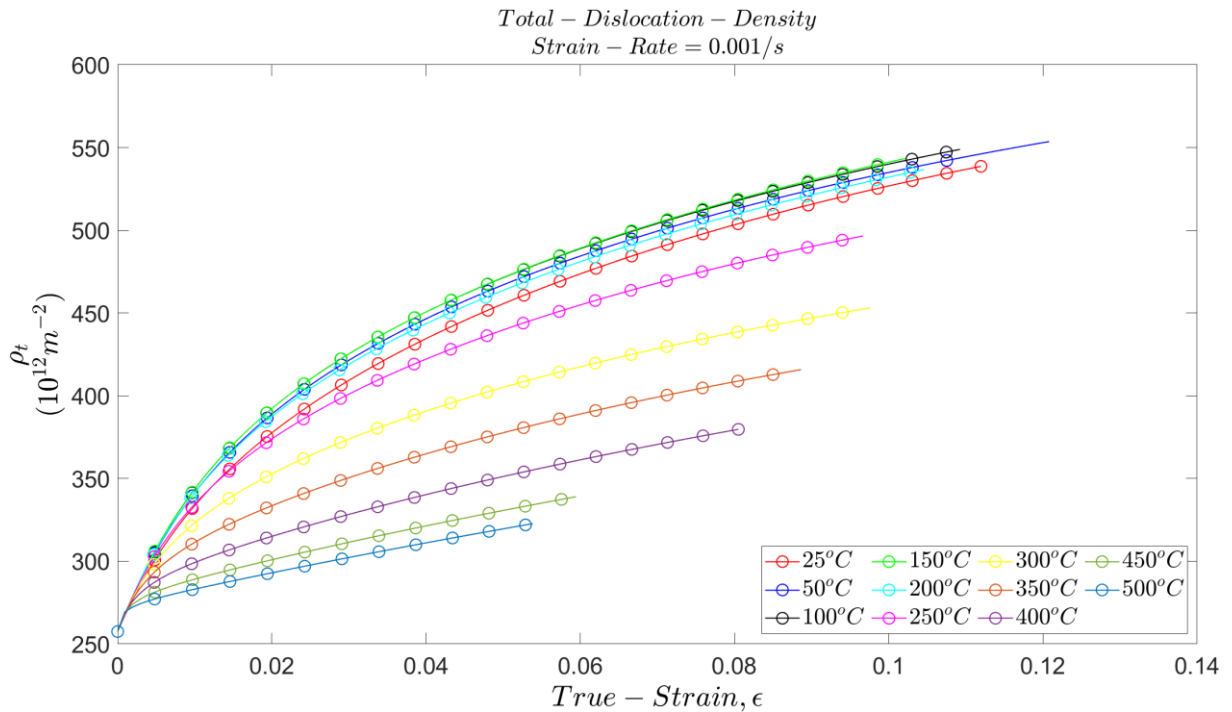
6.4.1: Total Dislocation Density

The numerical obtained total dislocation density at different strain rate for all test temperatures is as shown in the following figures below.

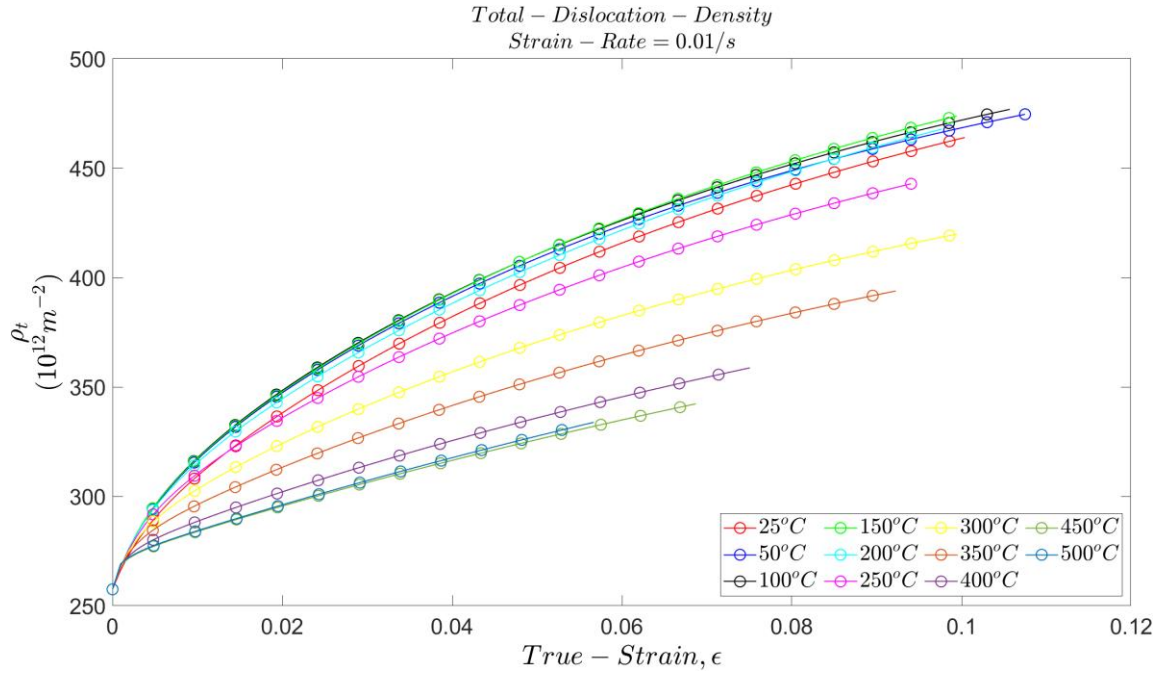
(a)



(b)



(c)



(d)

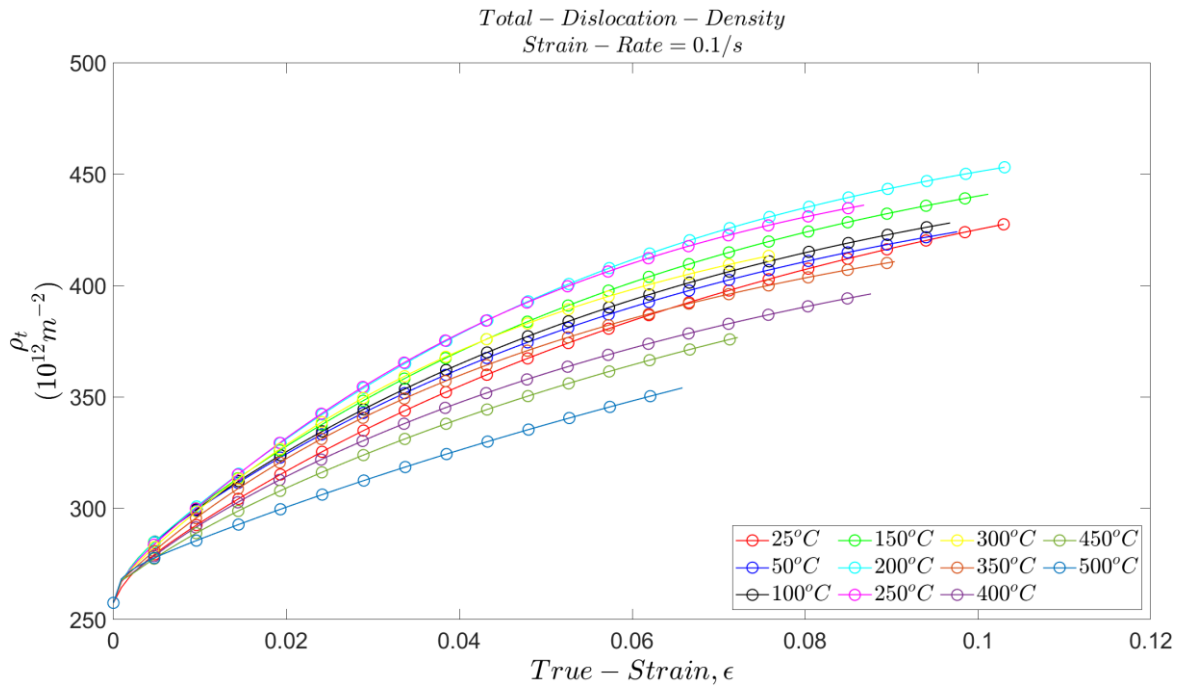


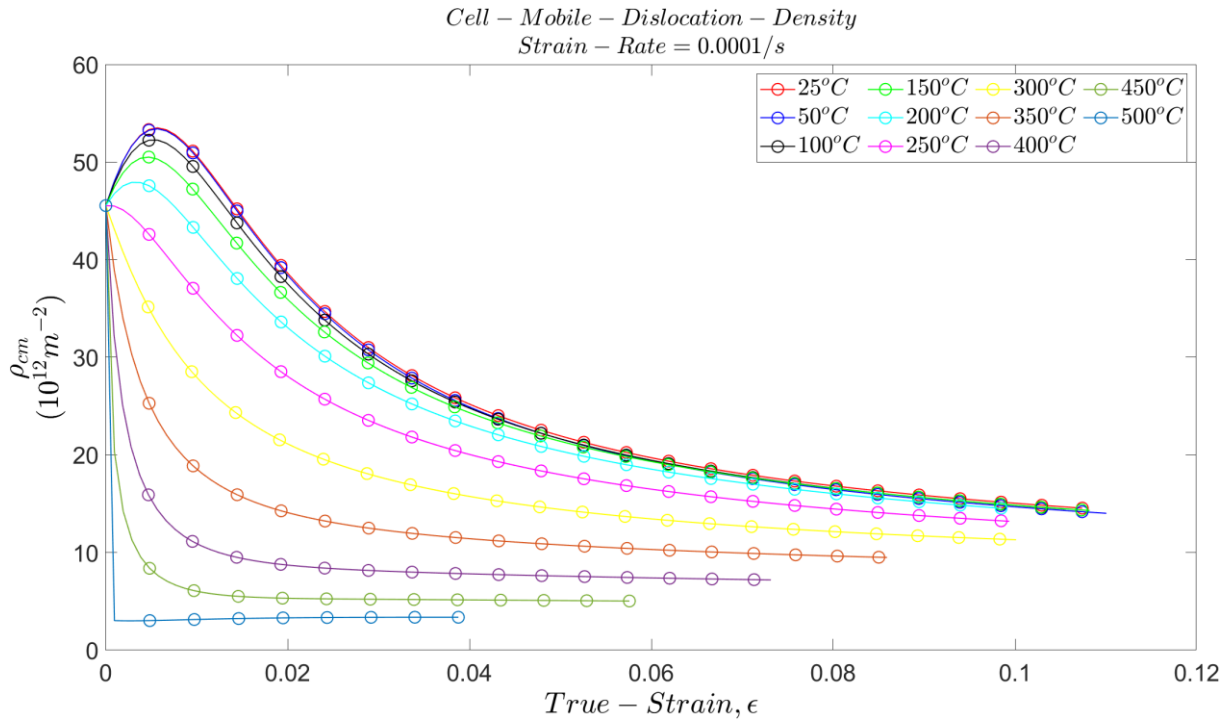
Figure 6.16: Total dislocation density as plastic deformation progresses at strain rates $0.0001/s$, (a), $0.001/s$, (b), $0.01/s$ (c), and $0.1/s$, (d).

The total dislocation density is seen to increase with plastic strain for all test temperature and at all test strain rates. This supports the hardening of the material at all test temperature and strain rate as plastic deformation develops. Across the strain rate, the total dislocation density decreases with increasing strain rate. This indicates

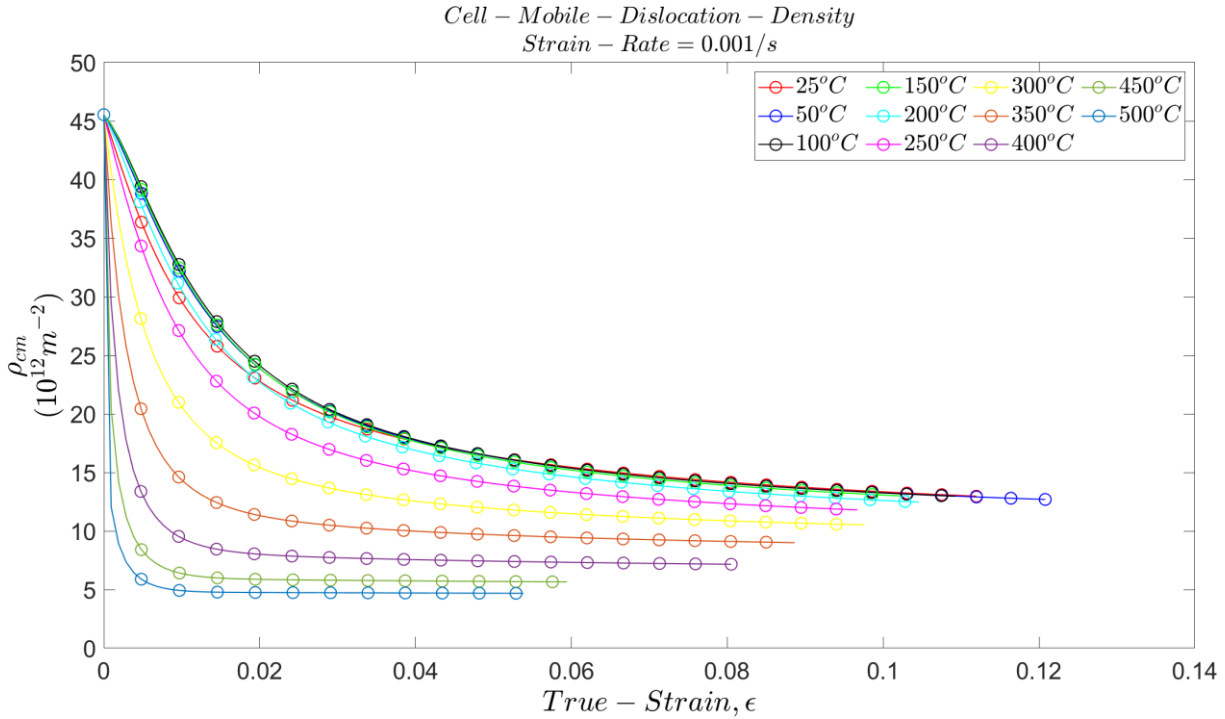
a decrease in plastic contribution to the flow stress with strain rate, therefore the higher flow stress at higher strain rate is consequent on the viscous stress contribution. Across the strain rate, a progressive maximum in total dislocation density in relation to temperature along with some clustering is observed for the temperature range 25°C – 300 °C. This is counterintuitive to the established understanding that higher temperature results in a lower dislocation density due to increased annihilation probability at higher temperatures. To rationalize this observation, one may consider that since generation of mobile dislocation is temperature independent, generation does not rationalize this, then the process of trapping by diffusion of interstitial solute atom to dislocation cores, a temperature and strain rate dependent process, which leads to storage may be likely responsible. The trapping process effect should wane at higher temperatures as annihilation or remobilization is enhanced leading to lowering of the total dislocation density at higher temperatures.

6.4.2: Cell Mobile Dislocation Density.

(a)

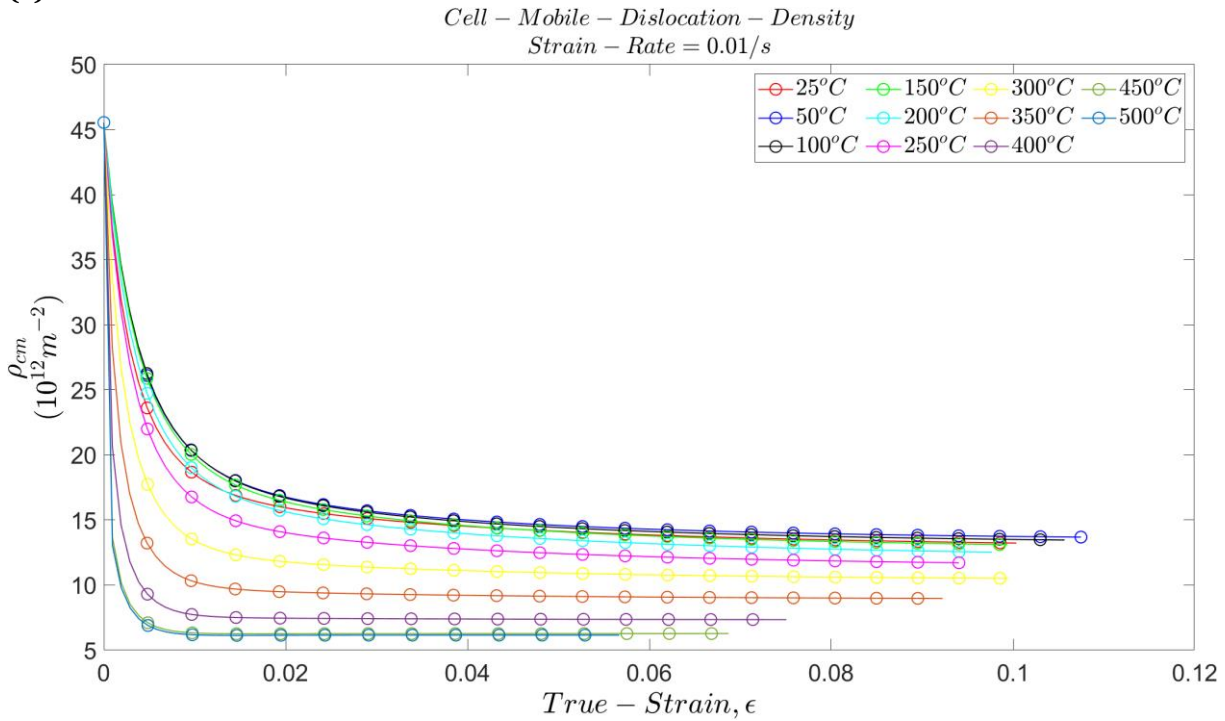


(b)



The cell mobile dislocation density as seen in the figures comprising the figure 6.16 decreases from a high value to a low constant/saturation value at higher plastic strain. Similar behaviour has been recorded in works by ([Amir & Prahl, 2019](#); [Bergström, 1970](#); [Roters et al., 2000](#)).

(c)



(d)

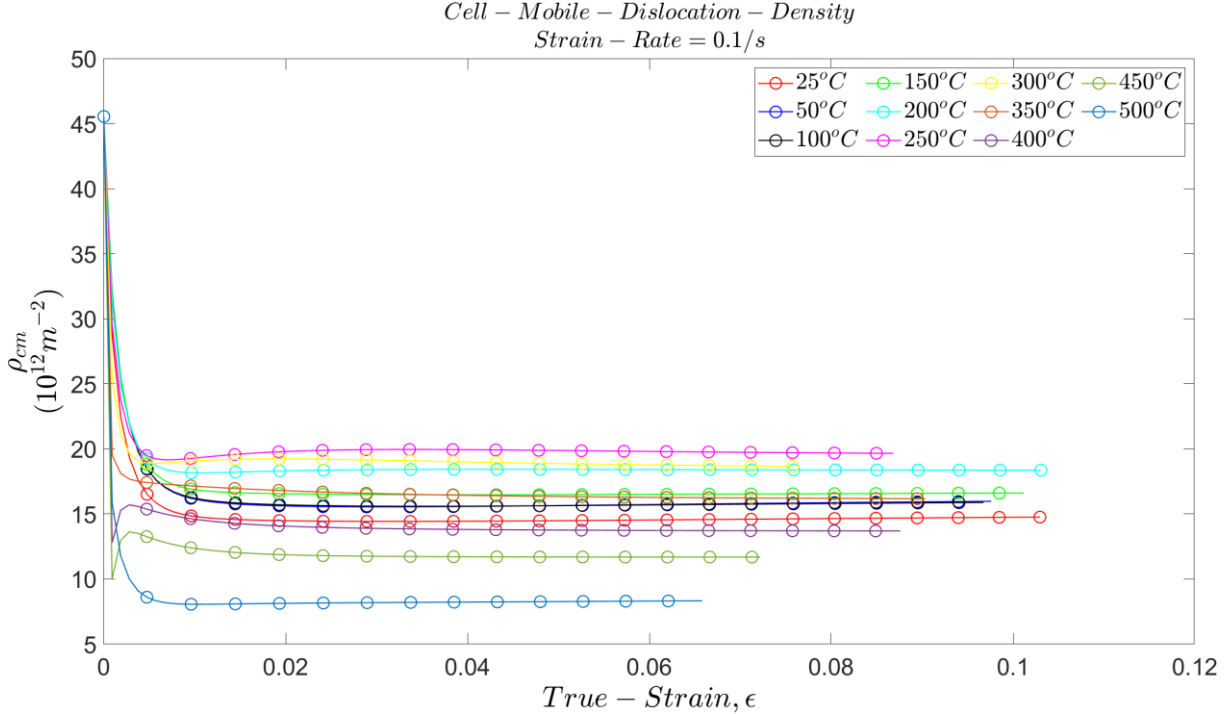


Figure 6.17: Cell mobile dislocation density at all test strain rate and temperatures.

The effect of temperature for all strain rate is a stronger decrease to a lower saturation value which is related to the increased annihilation probability at higher temperature. The steep decrease in cell mobile density may result from the rapid formation of the low energy dislocation heterogeneous cell structure. The constant cell mobile dislocation density as plastic strain is achieved is a stable state of cell mobile dislocation density required for the maintaining of similitude in the already developed heterogeneous cell structure.

The effect of the strain rate is seen to be a quicker transition to the cell structure i.e. increased descent to the saturation value of the mobile dislocation density. This behaviour is clearly understood to be due to the increased dislocation velocity due to higher strain rate which result in a quicker formation of the cell structure.

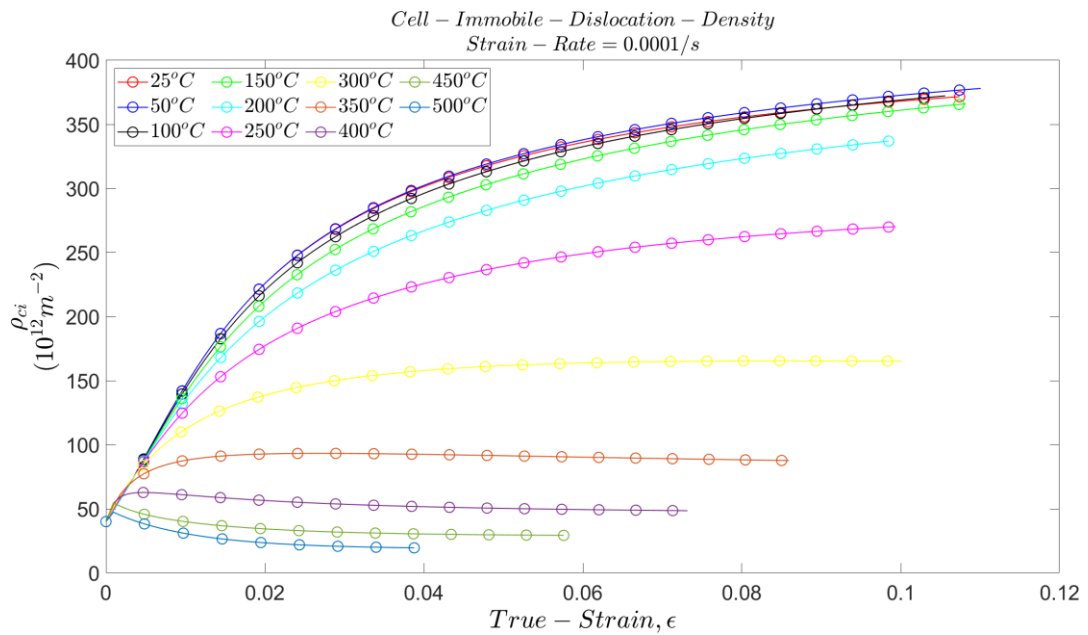
At the strain rate of 0.1/s, deviations in the general effect of the temperature is observed since higher saturation values than those for the lowest temperature are obtained at higher temperatures. Since annihilation probability which leads to

lowering of cell mobile dislocation density is increased at higher temperature, the only temperature dependent dislocation process which may cause an increase in mobile dislocation density is the remobilization dislocation process which has a higher probability with temperature. Also, at higher strain rate, since mobile dislocation are the carriers of plastic deformation, the remobilization probability is encouraged.

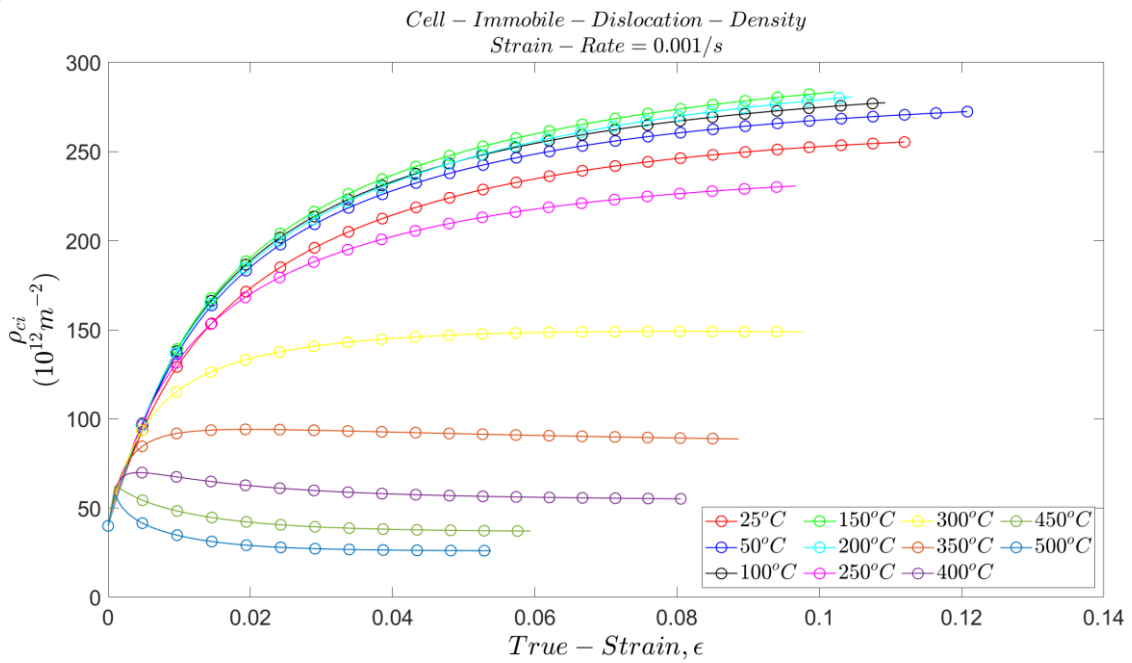
6.4.3: Cell Immobile Dislocation Density.

The cell immobile dislocation density seem to follow the same trend as found for the evolution of the cell mobile dislocation i.e. a decreasing density with temperature at the lowest strain rate, while at higher strain rates, a progressive inversion of dislocation density within the temperature range of 25°C – 250 °C figure 6.18 a, b, c, and d. The cell immobile dislocation density follows a progressive reduction across strain rates, with a saturation of its value with deformation progress.

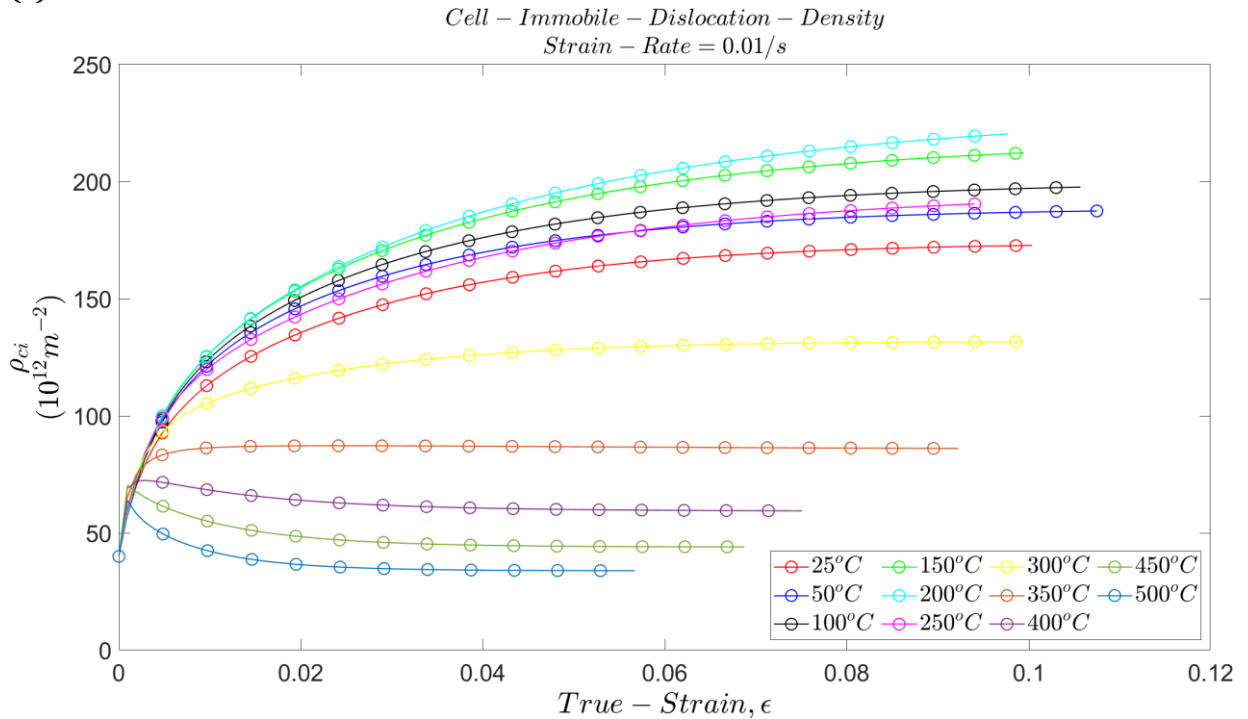
(a)



The temperature of 300 °C also looks to represent a defining/demarcating temperature. The saturation of the cell immobile dislocation density signifies just like the cell mobile

(b)

dislocation density saturation a formation and stabilization to a heterogeneous cell structure. The impact of temperature is connected to the probability of annihilation and/or remobilization (as seen at high temperature at and above 350 °C where cell immobile dislocation density slightly decreases) which decreases the cell immobile density.

(c)

(d)

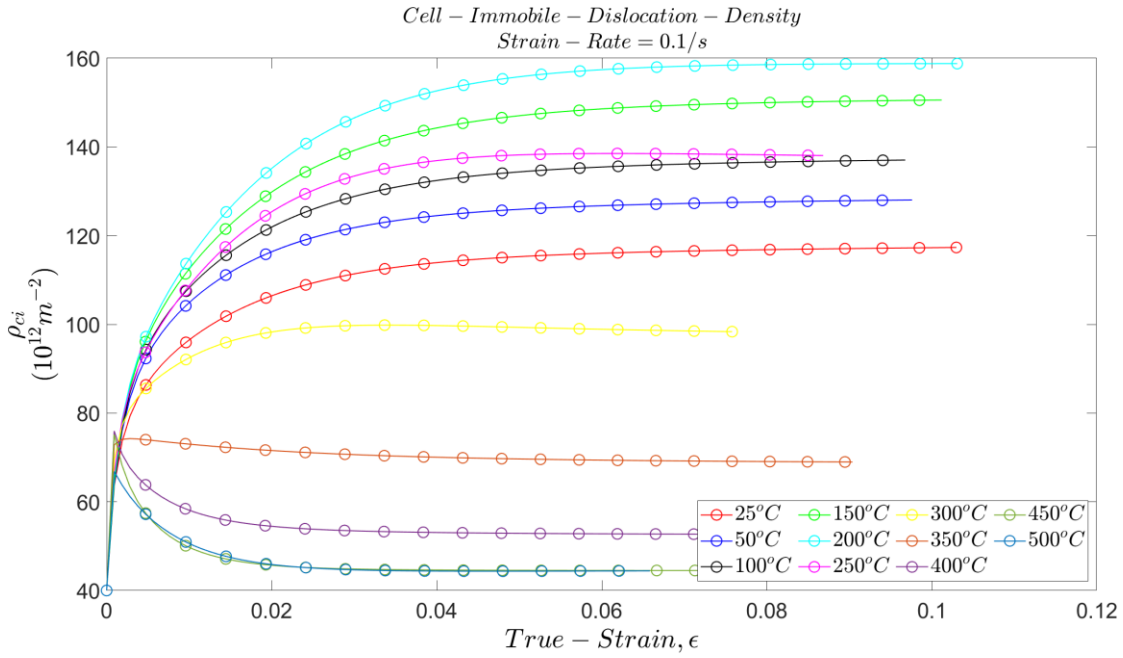
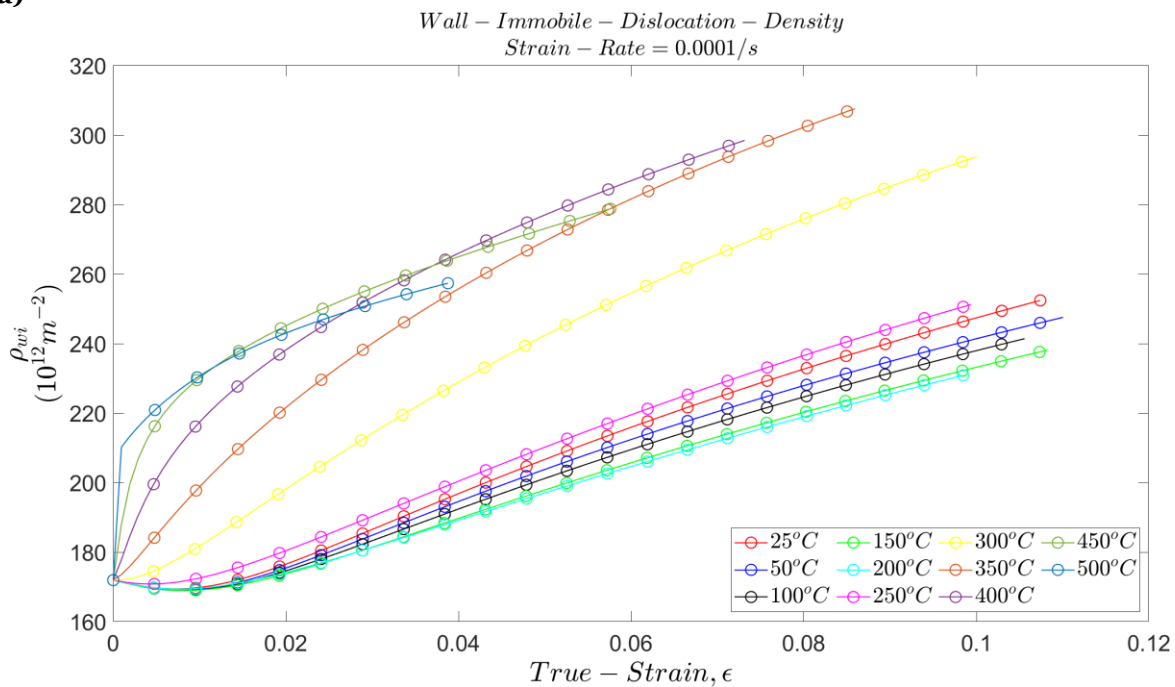


Figure 6.18: Cell immobile dislocation density for all test strain rates and temperatures.

6.4.4: Wall Immobile Dislocation Density.

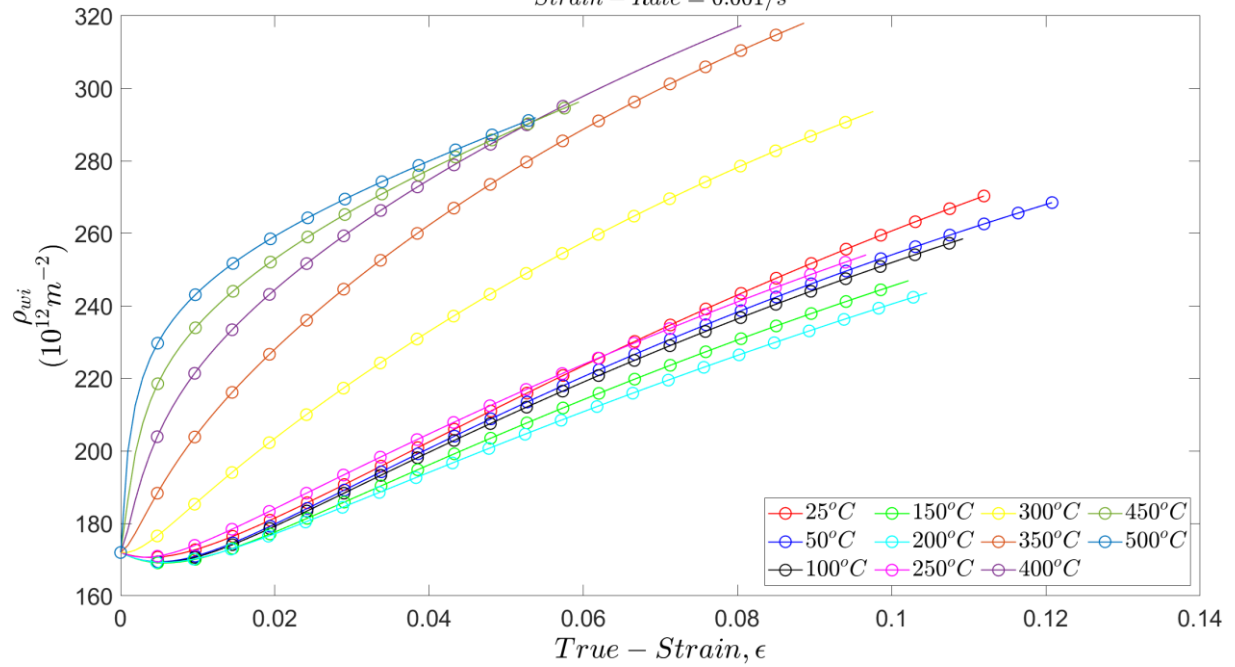
The wall immobile dislocation is predicted to show no saturation of the density with plastic strain. A demarcation of the dislocation density evolution is present with the temperature of 300 °C as the indicator as found in the evolution of cell immobile.

(a)

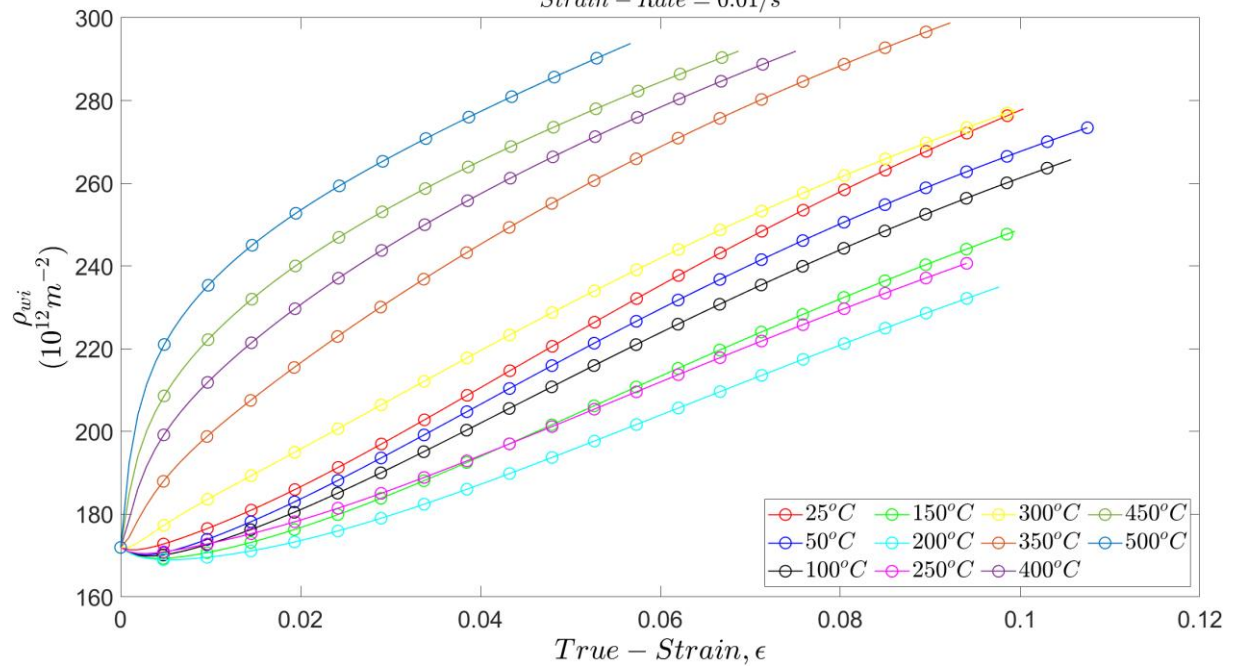


(b)

Wall – Immobile – Dislocation – Density
Strain – Rate = 0.001/s

**(c)**

Wall – Immobile – Dislocation – Density
Strain – Rate = 0.01/s



(d)

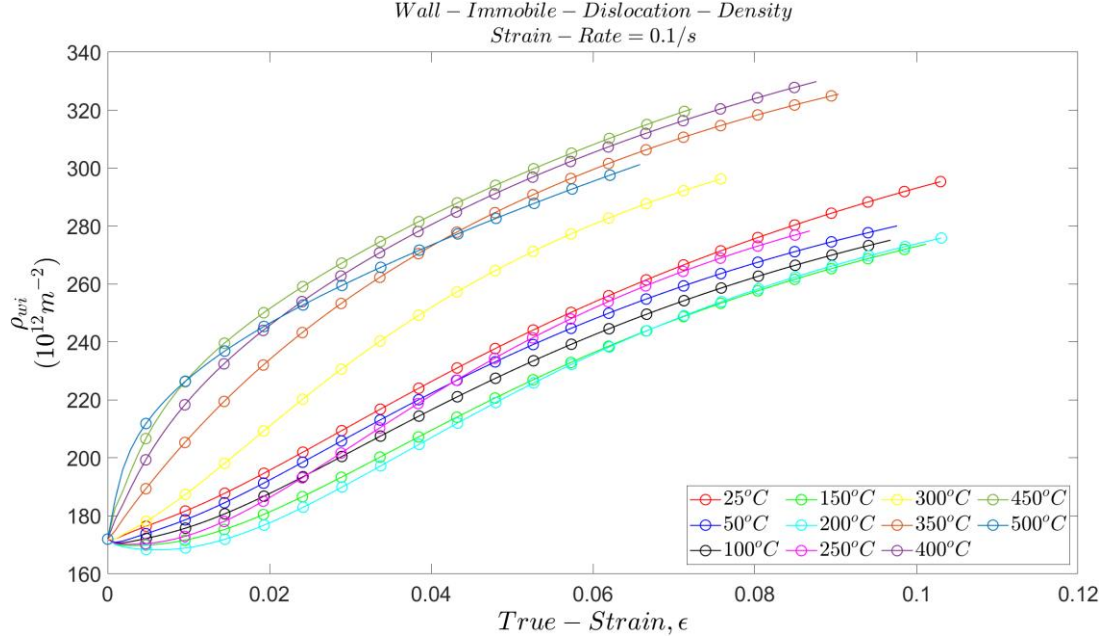


Figure 6.19: Wall immobile dislocation density for all test strain rates and temperatures.

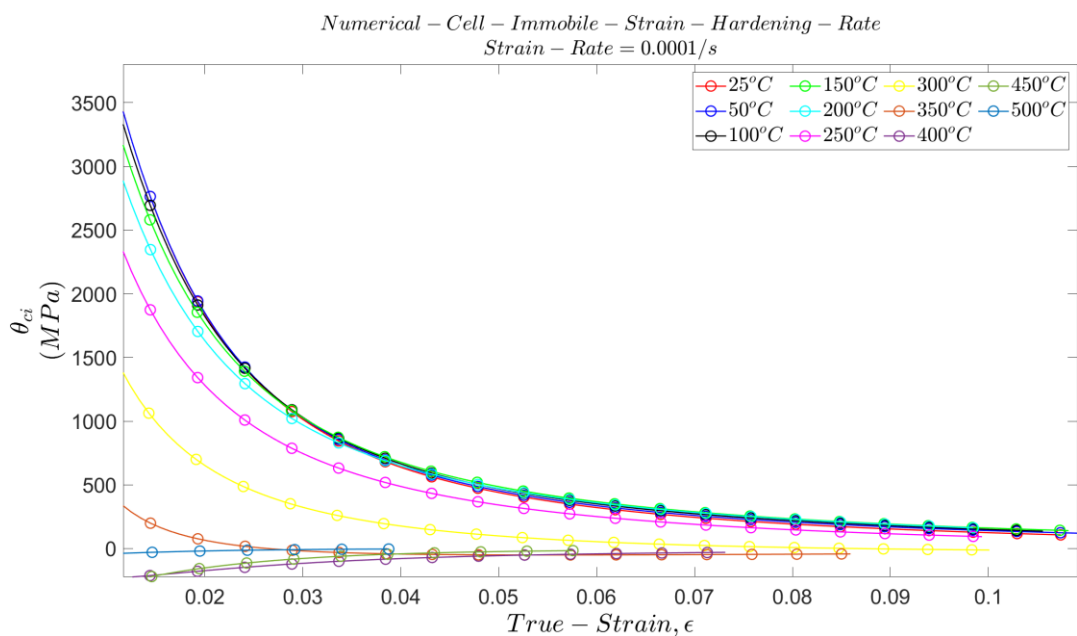
The wall dislocation density does not show progressive drop with strain rate. The rate of increase of wall dislocation with plastic strain is higher at temperatures above 300 °C than those for lower temperatures. The formation of wall dislocation at high temperatures is an energetically favourable process because the incorporation of dislocation into boundaries reduces the overall energy of the dislocation (Abbaschian et al., 2009) and therefore the energy of the structure, also the availability of energy due to high temperature provides the necessary energy to enable the preferred formation process. It is noteworthy to state that the dislocation energy reduction due to incorporation into GNBs is higher than incorporation into IDBs. This indicates a favourable incorporation of cell mobile and immobile (by remobilization) dislocations into the wall immobile dislocations as observed by (Y. Estrin et al., 1998). In the temperature range below 300 °C, an inverse relation between wall immobile dislocation density and temperature is predicted which is in agreement with the earlier prediction

of a favoured formation of cell immobile dislocations in this temperature range due to trapping or pinning process.

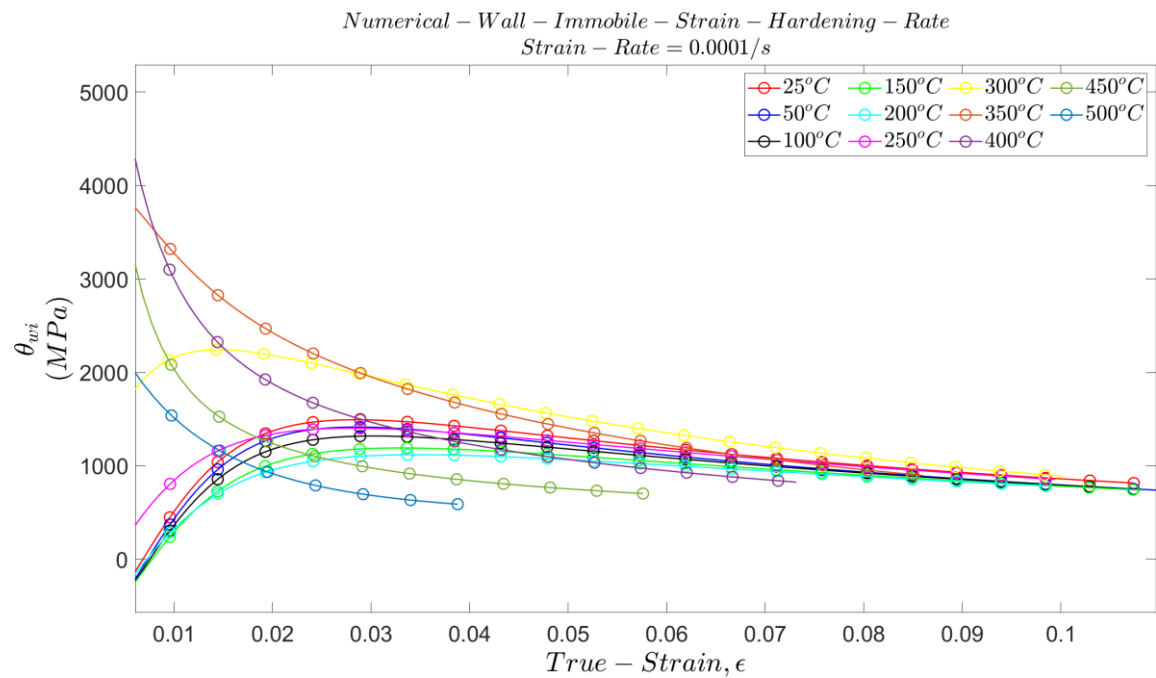
The favoured formation of wall immobile dislocation density at higher temperature may explain the observed low uniform elongation at such temperatures because of the localization of strain within the cell bands leading to early onset of necking. As is shown in the figure 6.20, the presence of cell immobile dislocation is a penalty on strain hardening or contributes nothing other than providing cell mobile dislocation by remobilization.

Based on the obtained evolution of cell immobile and wall immobile dislocation densities, it may be seen that at all test temperatures for all test strain rates, contribution of the cell immobile dislocation density to strain hardening rate at high temperatures (350°C and above) is only substantial at small strains and lower temperature, at strains greater than 3%, the main contribution to the strain hardening is from the wall immobile dislocations, as depicted in the figures following.

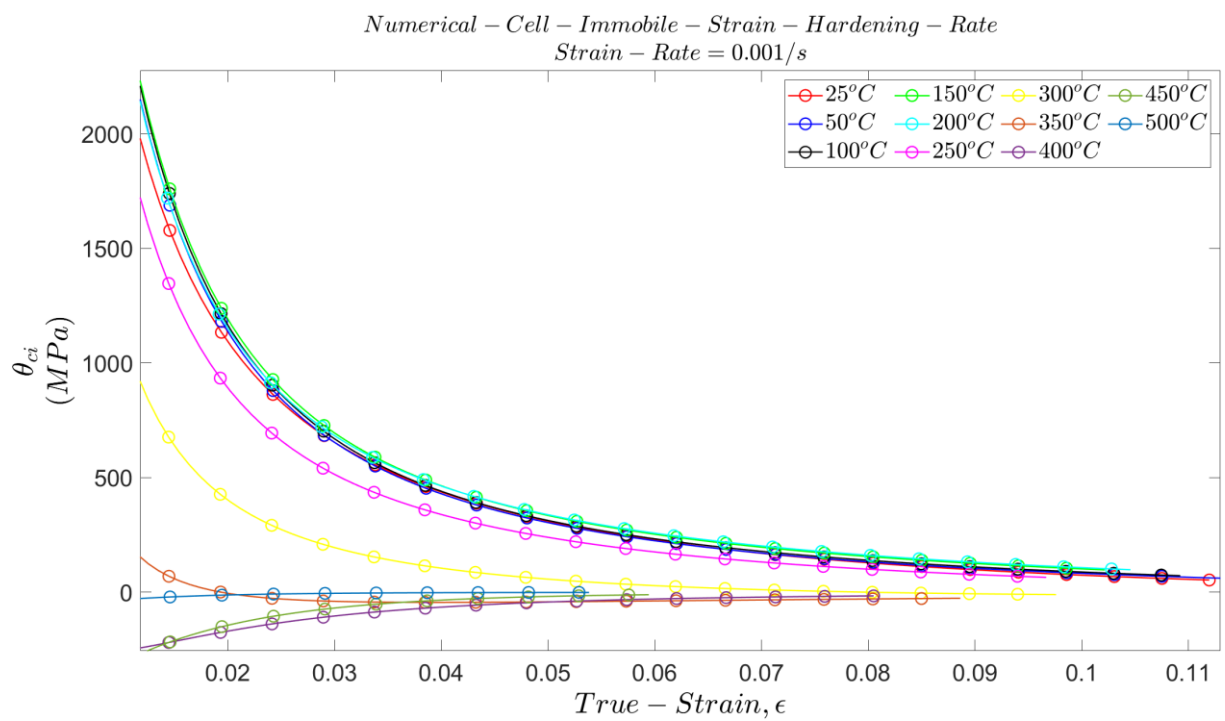
(a)



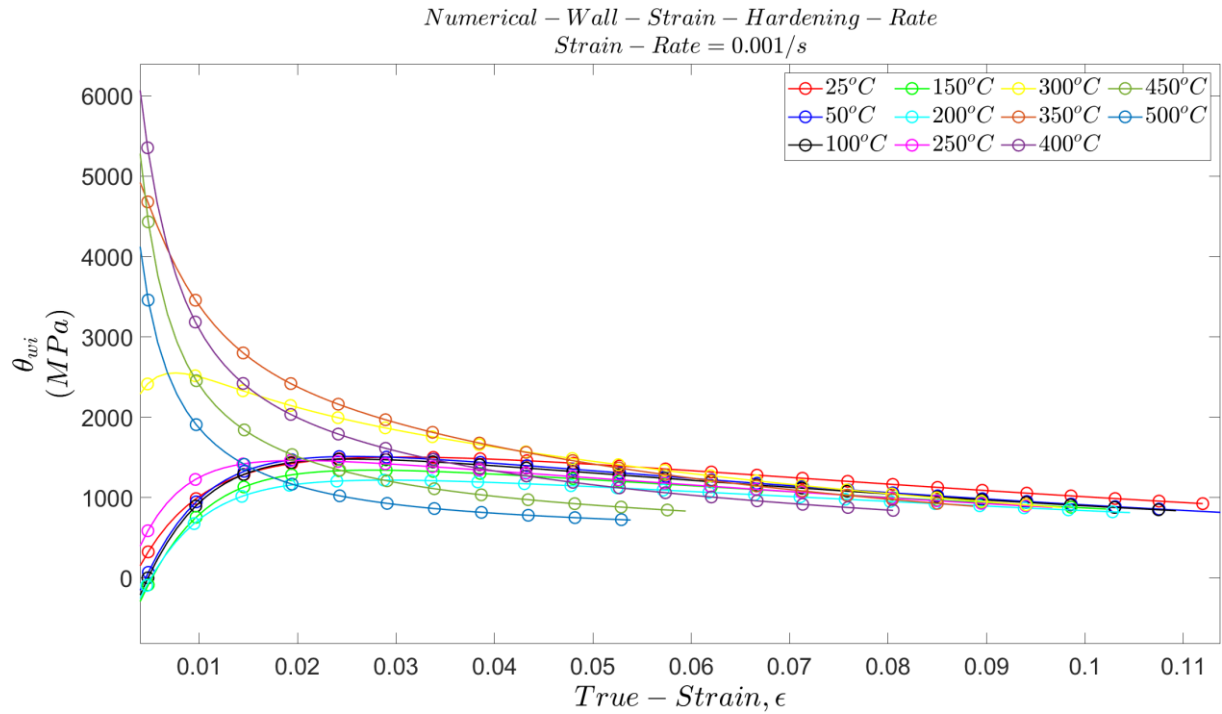
(b)



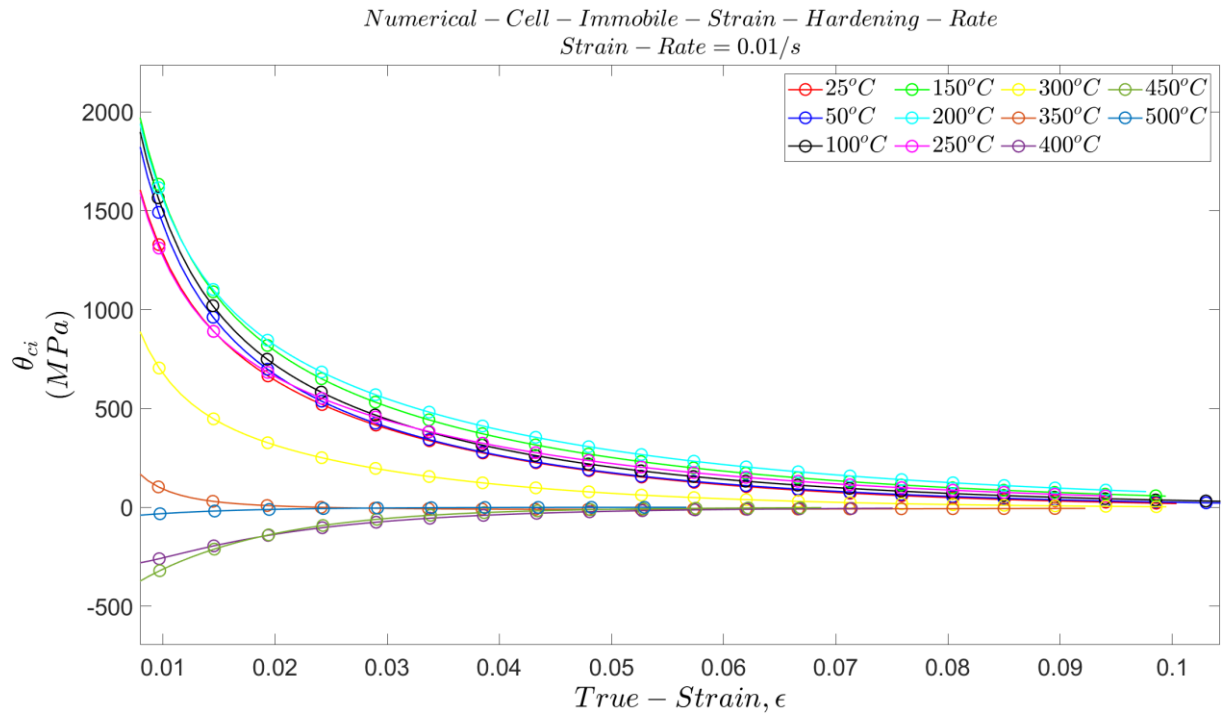
(c)



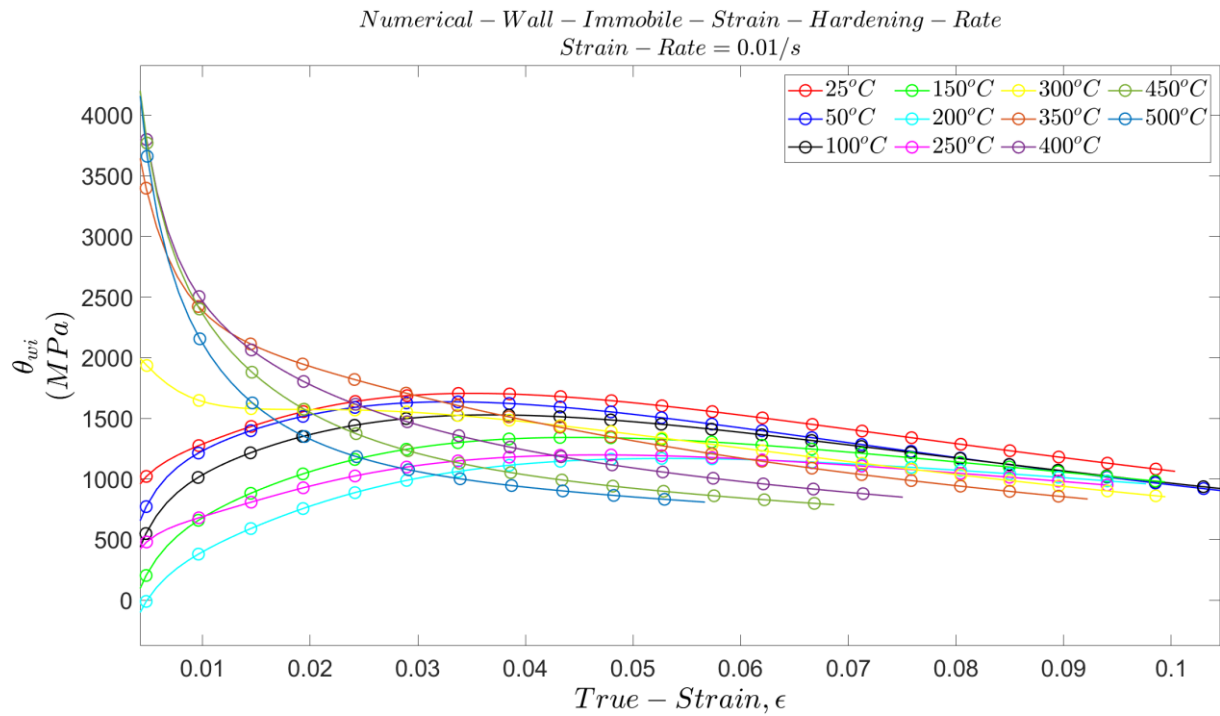
(d)



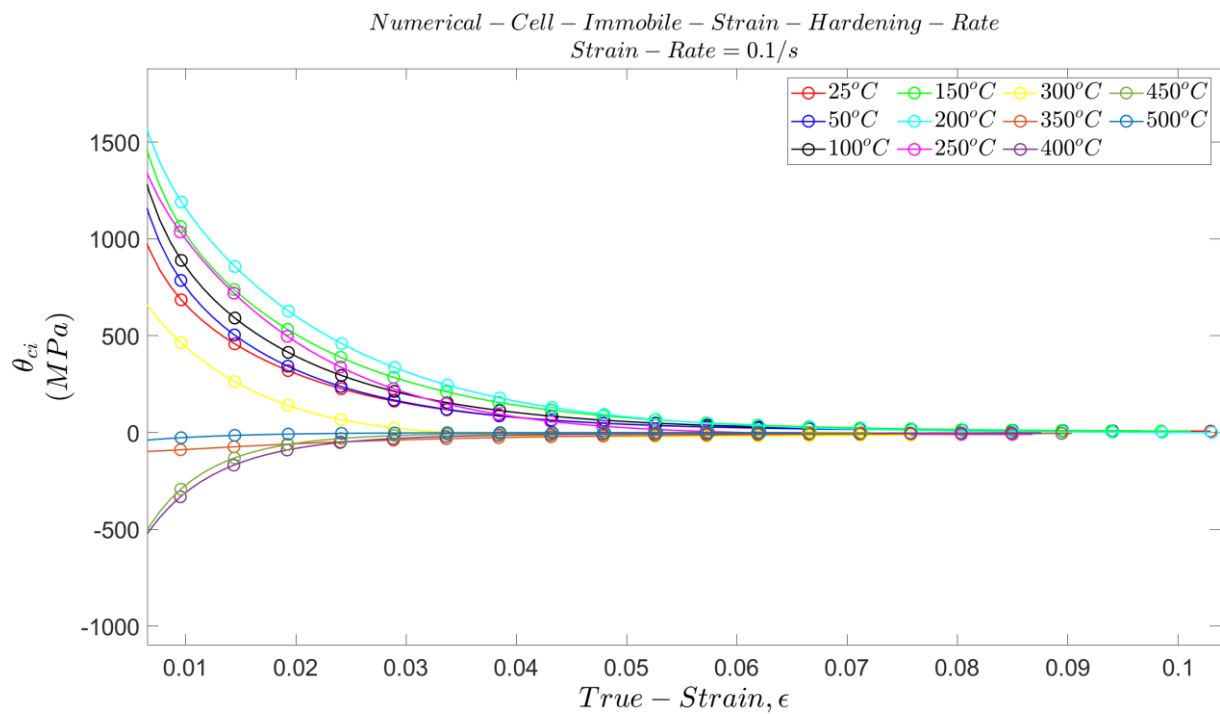
(e)



(f)



(g)



(h)

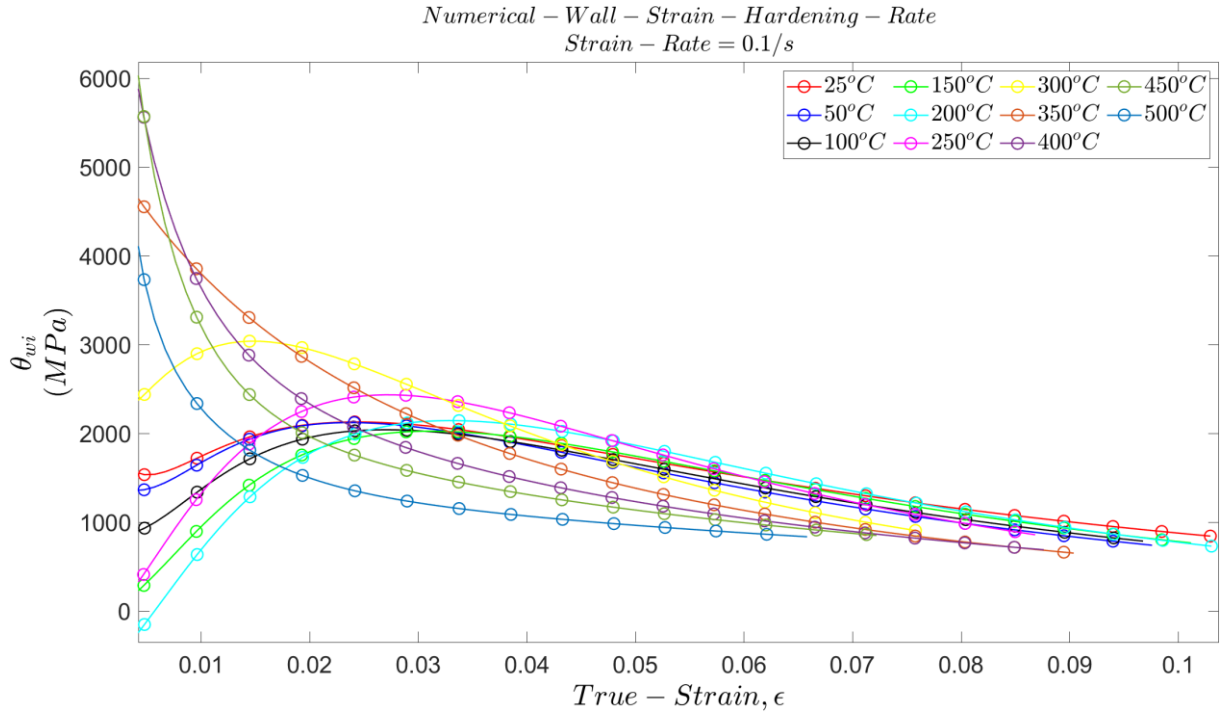


Figure 6.20: Strain hardening contribution from cell and wall immobile dislocation at all test temperatures and strain rates.

In a collective outlook of the dislocation evolutions, for temperatures at 300 °C and below, the mobile cell density decrease to saturation correlates well with the increase of cell immobile density to saturation, which supports the notion that early heterogeneous cell structure formations in terms of IDBs begins the plastic deformation. It observed that the saturation of both kinds of dislocation occur at 2% strain which coincidences with the strain at which wall dislocation density show substantial increase rate. For temperatures at 350 °C and above, plastic deformation occurs with substantial increase of the wall immobile dislocation with slight increase of the cell immobile dislocations which are remobilized and incorporated into the walls as plasticity progresses.

6.5: Material Dislocation Process Coefficient.

6.5.1: Trapping of cell mobile dislocation

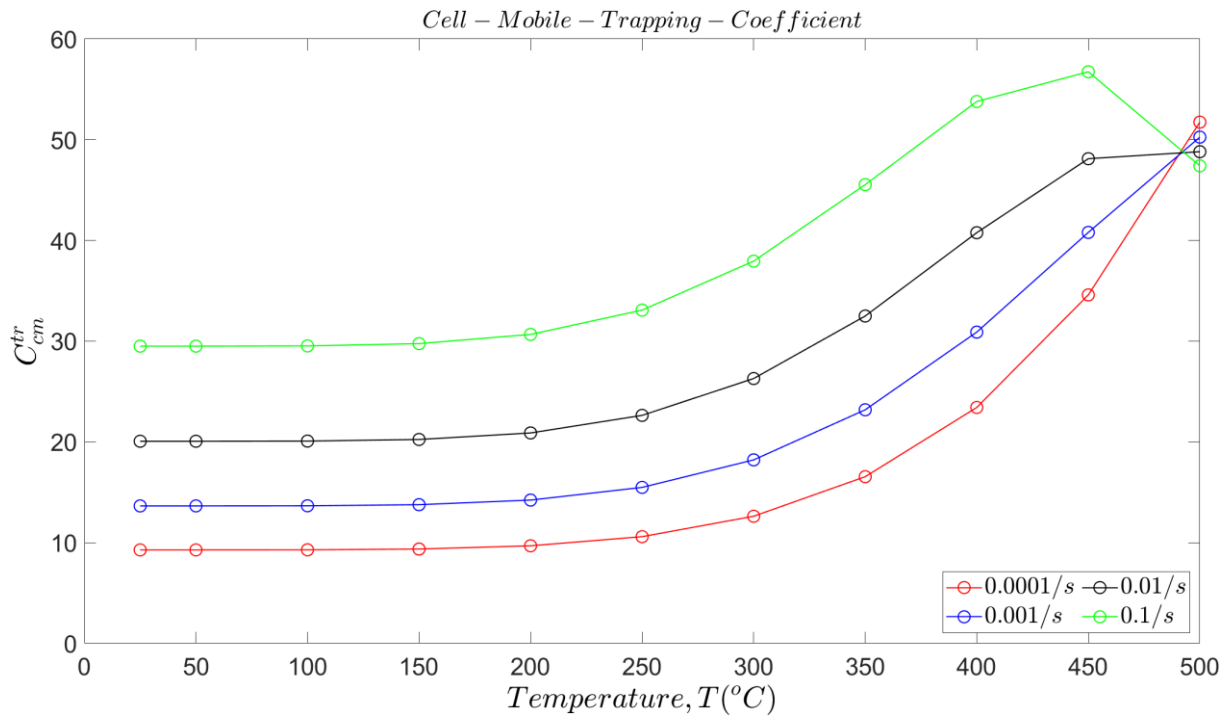


Figure 6.21: Cell mobile trapping coefficient for all test temperatures and strain rates.

The numerical prediction here proposes an increase of trapping probability with temperature. Since trapping is related to the ease of diffusion/migration of interstitial solute to dislocation core, a temperature activated process, it is simply a given that increasing temperature would enhance the trapping probability.

The effect of strain rate on this coefficient as seen in the figure above is an increase with strain rate. This trend is somewhat in opposition to the established knowledge of the relation between the dislocation velocity and trapping probability ([Mishra et al., 1989](#)) where it is understood that high dislocation velocity should result in less trapping by dislocation core decoration with solute atom because enough wait time is not provided for diffusion to dislocation cores. This may point to another mechanism of trapping which is not diffusion dependent but temperature dependent, probably a cross slipping efficiency, which is enhanced at higher temperature, result in dislocation trapping reactions on the new slip planes which leads to further development of

obstacles on these slip planes that increases trapping. Also, in the case of strain rate increase, a need for enhanced cross slip to meet the plastic strain demand of the strain rate is necessary in the presence of slip plane obstacles since the other way the demand of plastic strain can be met is by generation of a huge amount of dislocation which travel short distance, however, generation of mobile dislocation is not temperature and strain rate dependent and therefore it is not efficient to serve the increased strain rate. In summary, higher strain rate and temperature results in higher imposed cross slip which leads to higher dislocation trapping reactions.

The physical demonstration of the trapping efficiency is seen in the increased wall immobile and decreased cell immobile dislocations at higher strain rates i.e. higher remobilization of cell immobile and incorporation into wall immobile dislocations.

6.5.2: Remobilization of Cell and Wall Dislocations.

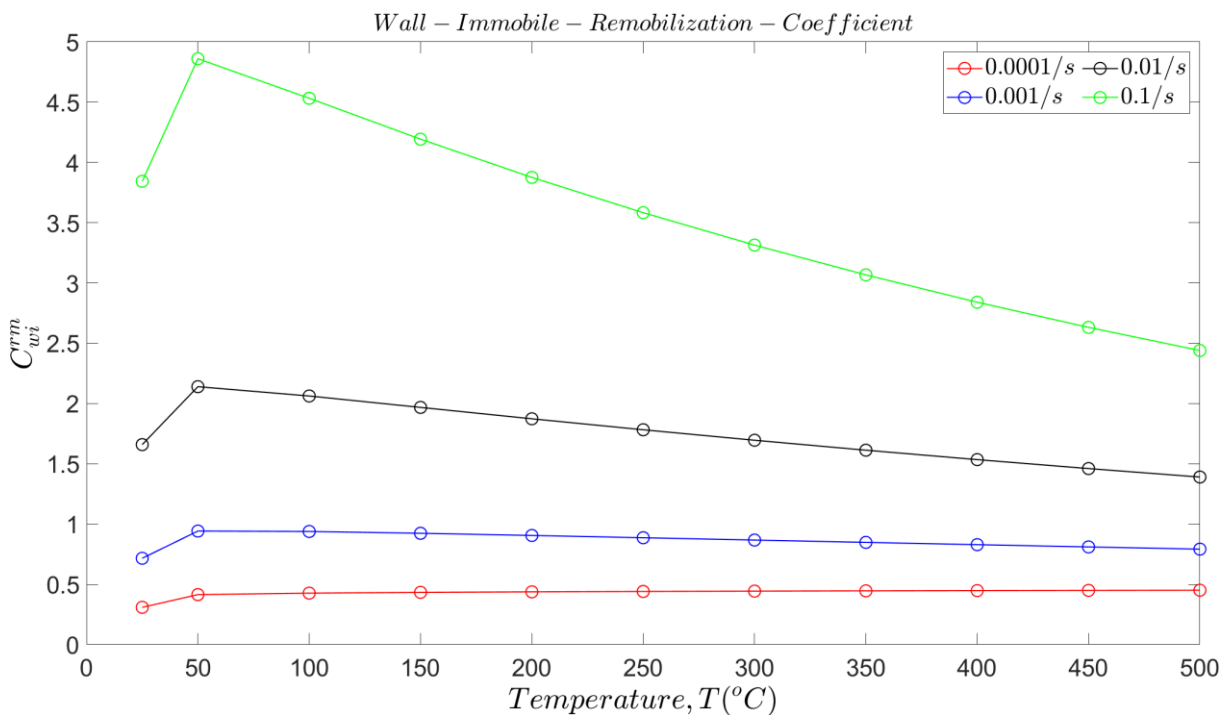


Figure 6.22: Wall immobile remobilization coefficient for all test temperatures and strain rates.

The wall immobile dislocation shows a maximum at higher strain rate but relative flat at the two lowest strain rates. The maximum occurs at 50 °C. This trend posits a stabilization of the dislocation structure in terms of wall immobile dislocations, *GNBs*, however the efficiency of remobilization been high at low temperatures is counterintuitive as temperature results in probability increase of remobilization due to cross-slip and climb being favoured as temperature increases ([Zehetbauer & Seumer, 1993](#)).

The remobilization trend for the cell immobile dislocation shows enhanced efficiency at high temperature only for the two highest strain rates, a steep decrease from 25 °C – 50 °C and a flat line for further temperatures in the case of the lowest strain rates.

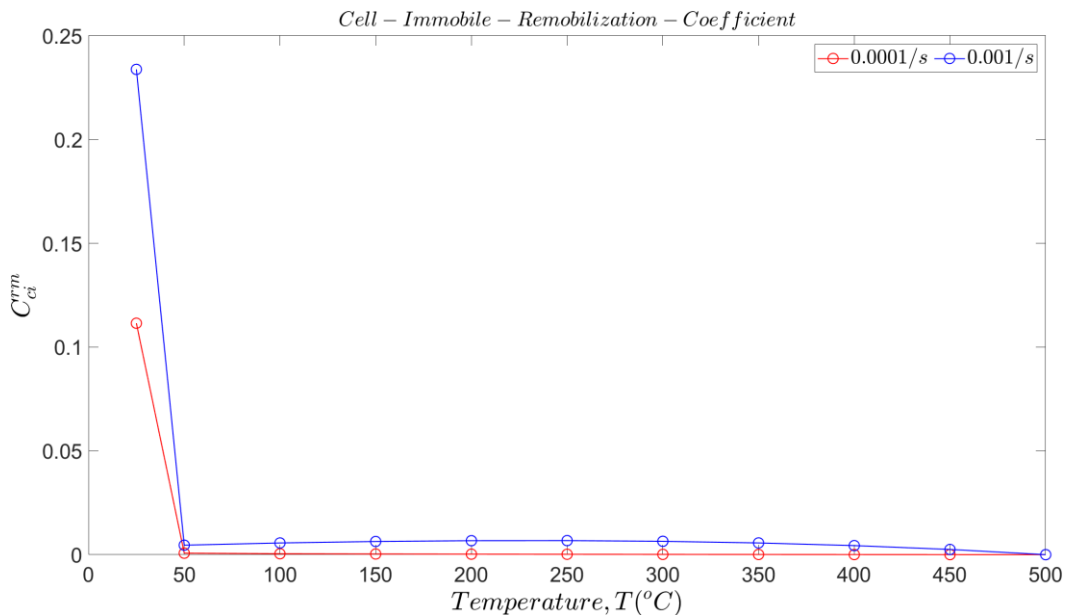


Figure 6.23: Cell immobile remobilization coefficient at all test temperatures for strain rates of 0.0001/s and 0.001/s.

The cell immobile remobilization trend at high temperature and high strain rates shows that the cell immobile dislocation density structure is unstable for the condition, this supports the stable wall immobile structure, and shows up in the increased cell mobile dislocation density at higher temperature. The coefficient values at 25 °C seem an anomaly.

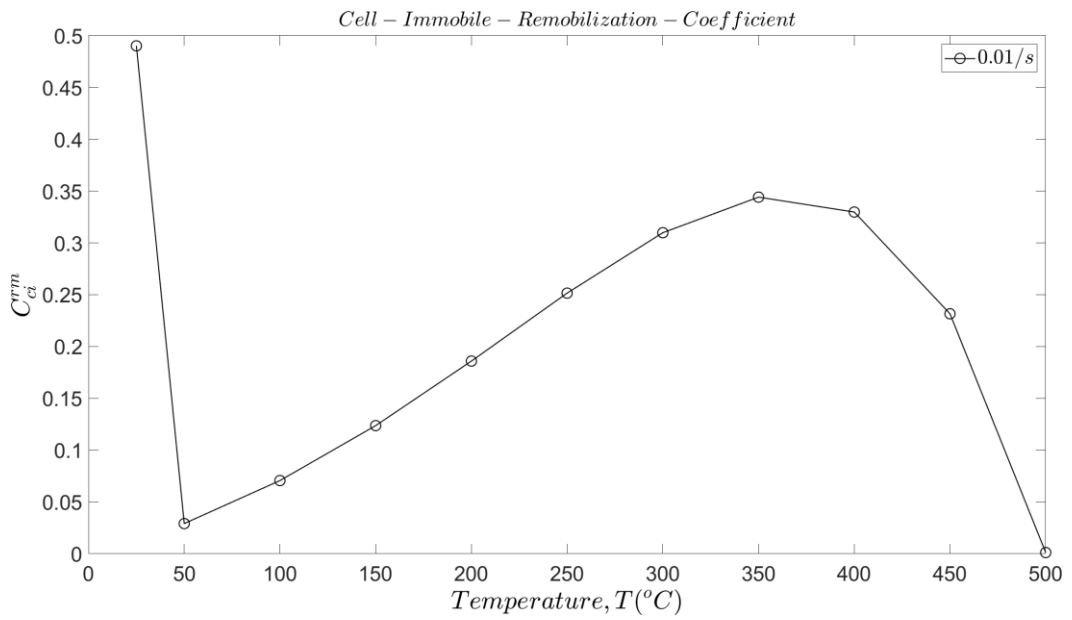


Figure 6.24: Cell immobile remobilization coefficient at all test temperatures for strain rate of $0.01/s$.

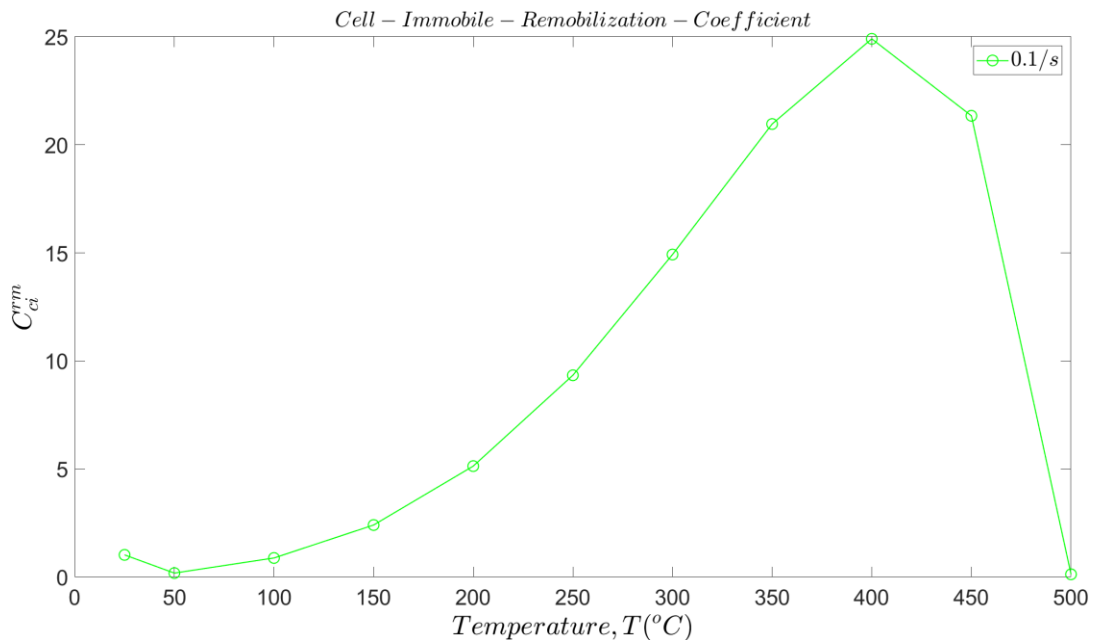


Figure 6.25: Cell immobile remobilization coefficient at all test temperatures for strain rate of $0.1/s$.

6.5.3: Nucleation of Wall Immobile Dislocation.

The nucleation of wall immobile dislocation is seen to increase with temperature in support of the favouring of wall immobile dislocation formation with increasing

temperature which is also supported by the decreasing annihilation and remobilization evolution trend with respect to temperature. The strain rate effect is only a slight increase in wall dislocation nucleation with a swap of strain rate relationship at a temperature between $400\text{ }^{\circ}\text{C} - 500\text{ }^{\circ}\text{C}$. The slight increase with strain rate may be connected to the increase of trapping with strain rate where the trapped dislocations become nuclei for the wall immobile dislocation structure. The swap may also result from substantial annihilation of wall dislocation at high strain rate and high temperature in comparison to lower strain rates and temperatures.

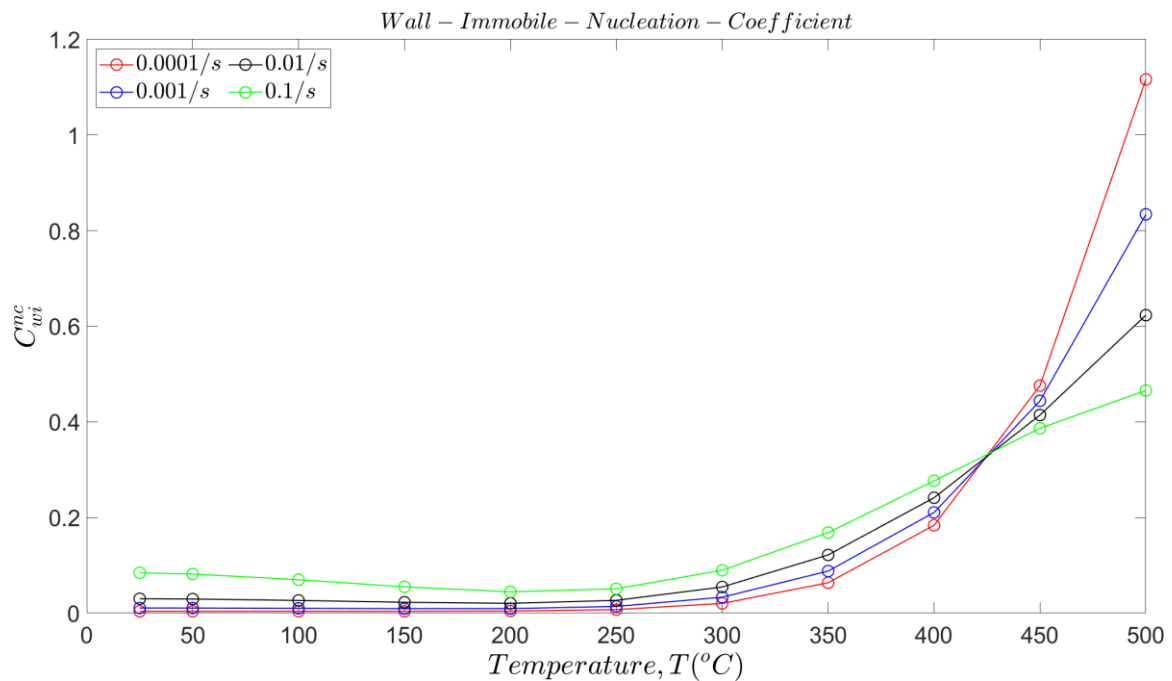


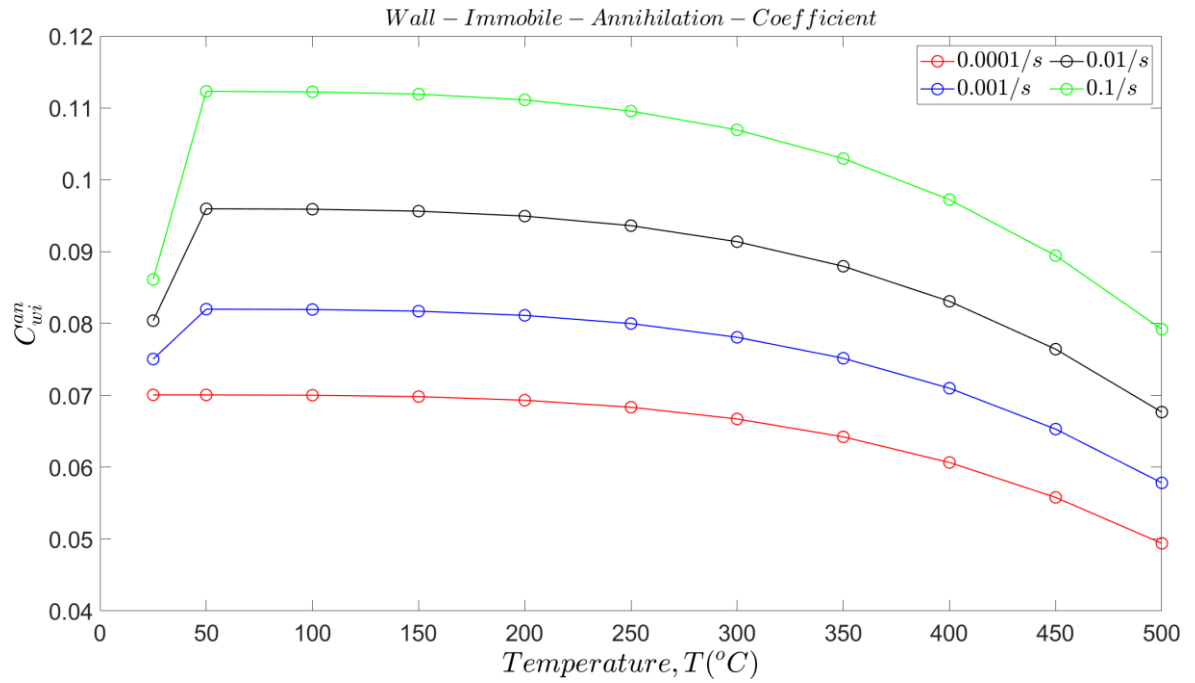
Figure 6.26: Wall immobile nucleation coefficient at all test temperatures for test strain rates.

6.5.4: Annihilation of Dislocation.

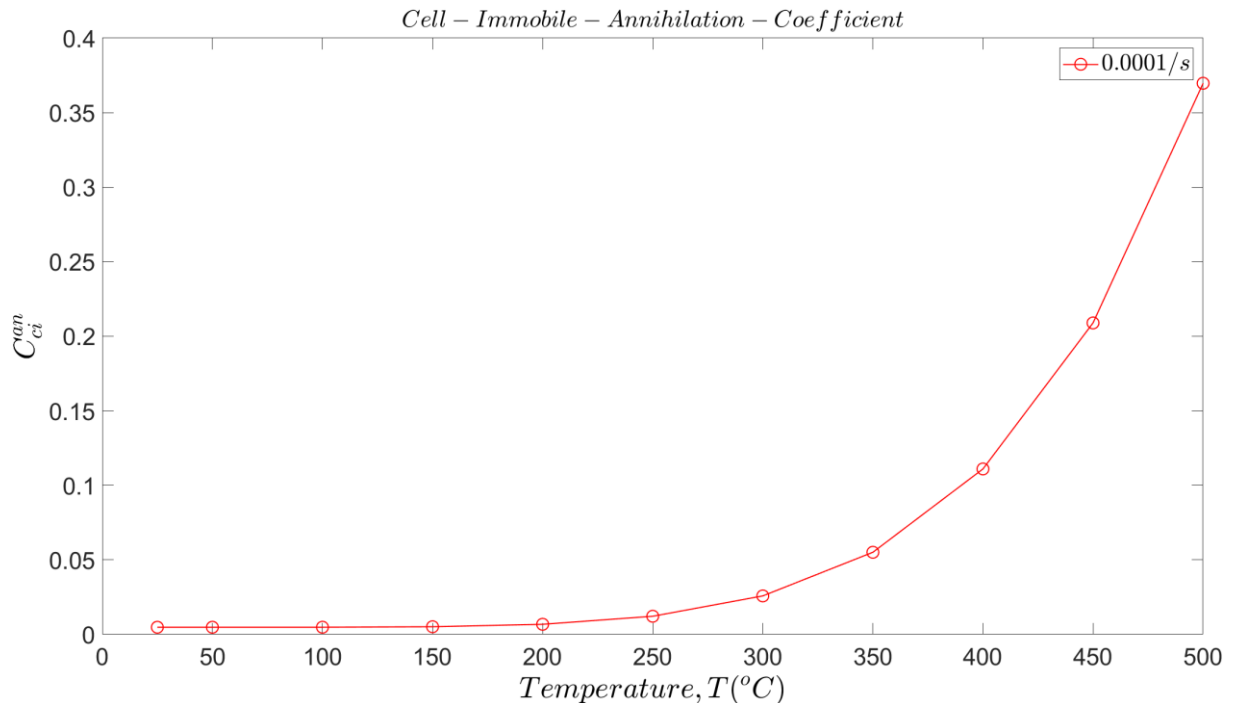
The annihilation coefficient for the wall immobile dislocation is shown to decrease with temperature for all strain rate, with higher strain rates showing higher annihilation coefficients. This trend is counterintuitive given what is known as to the nature of annihilation and temperature (Rollett & Kocks, 1993; Zehetbauer & Seumer, 1993).

The trend for annihilation of cell immobile and mobile dislocations at strain rate of 0.0001/s are the only curves which completely follow the expected annihilation relationship with temperature. At other strain rates, partial or complete opposite annihilation temperature relationship trends are obtained.

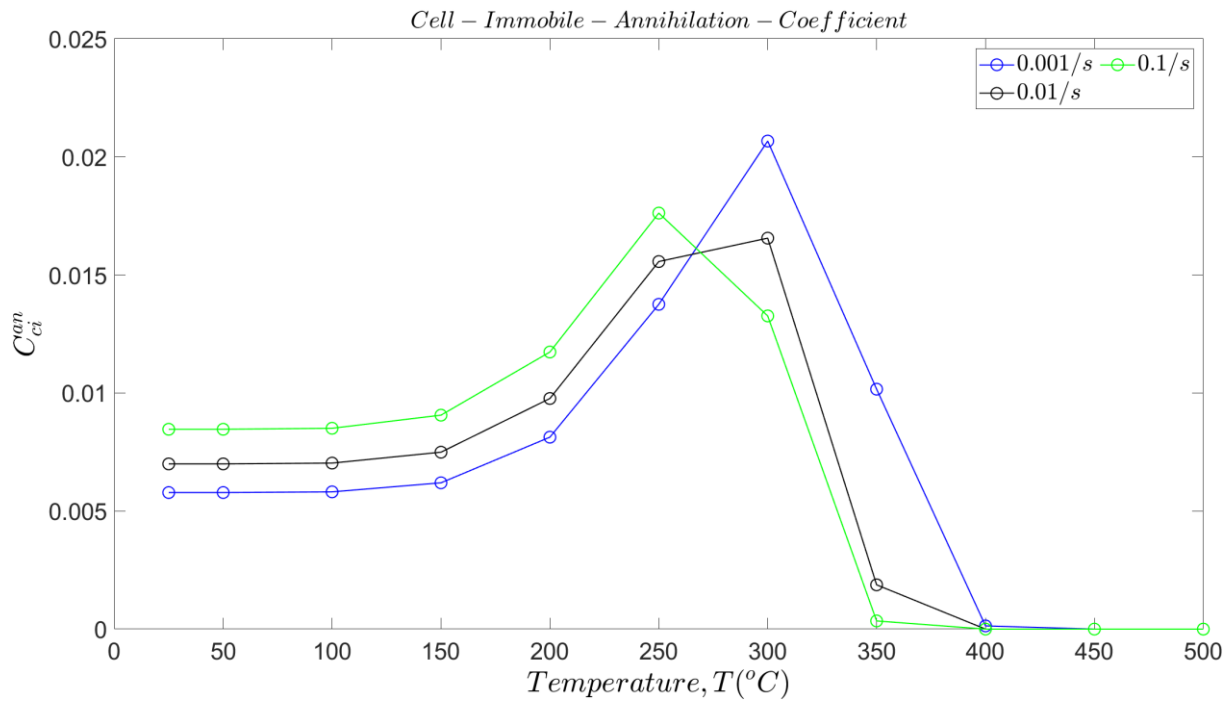
(a)



(b)



(c)



(d)

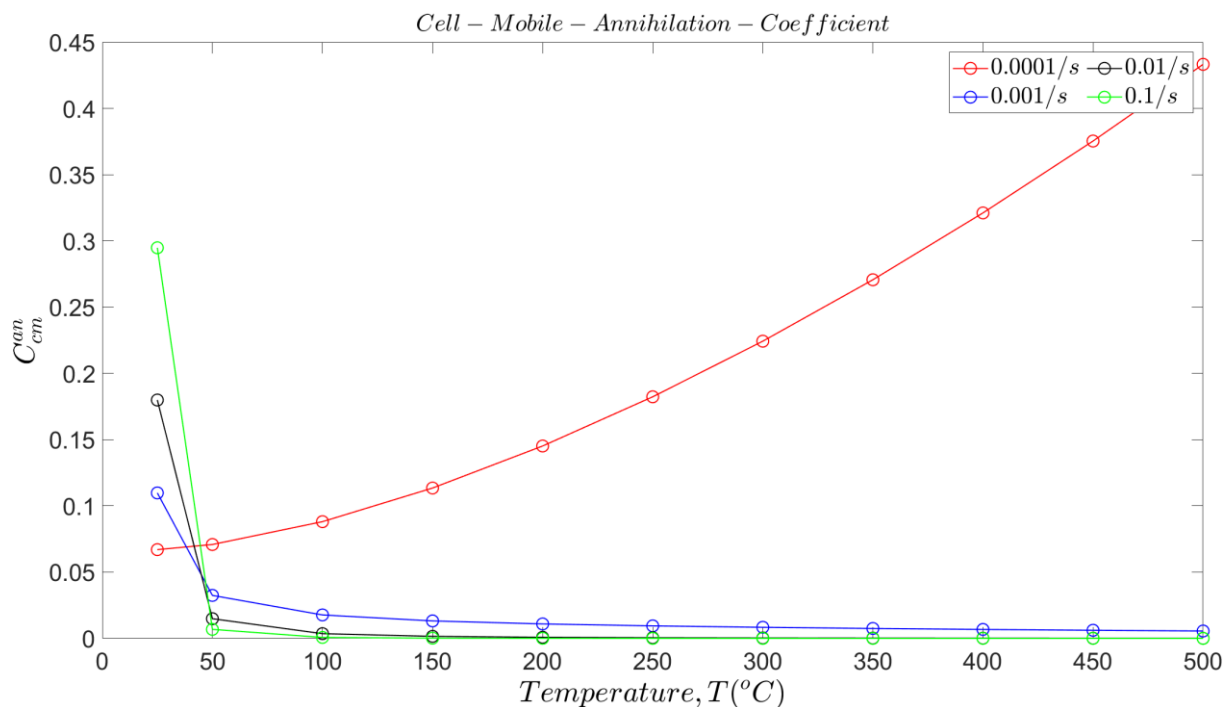


Figure 6.27: Annihilation coefficients for wall immobile (a), cell immobile (b and c), and cell mobile dislocations.

To attempt at a collective outlook on the dislocation process coefficients;

The trend in the dislocation coefficients of the wall immobile nucleation, remobilization, annihilation, and cell mobile trapping are such that a production of slightly increased wall immobile dislocation at higher strain rate at temperatures below 350 °C is obtained. This is achieved by the slight higher nucleation probability with strain rate, and the very substantial cell mobile trapping amidst the higher nucleation and annihilation of the wall immobile dislocations. The trend towards higher wall immobile dislocation density at higher temperature is connected to the reduced annihilation and remobilization efficiency with increasing temperature which as has been stated, is counterintuitive to experimentally established knowledge on annihilation and remobilization process, however the formation of lower energy structures like GNBs are energetically favourable when annihilation or remobilization processes are inefficient in reducing the wall immobile dislocation density.

The trend in the dislocation coefficients of the cell immobile on the other hand as already stated, the remobilization coefficient at the highest strain rate supports the trend seen in the cell mobile dislocation density evolution. The trend for the annihilation coefficient of the cell immobile and mobile dislocations only follow the established knowledge of increased annihilation efficiency at the lowest/reference strain rate. At higher strain rates the trend shows a different outcome.

6.6: Validation.

To properly validate the obtained constitutive parameters, tensile models are developed in the ABAQUS software (Simulia, 2017), and tensile test conditions which are imposed in the physical experiments performed in this work are simulated in an explicit analysis. The models are analysed using a developed user subroutine based on a radial return mapping or elastic predictor plastic corrector algorithm. The flowchart of the algorithm applied in the analysis is as prescribed by (Motaman et al., 2019). From the user subroutine analysis a total of 6 state dependent variables comprising the, mobile, cell immobile, wall immobile dislocation densities, the plastic strain, the plastic strain rate, and the yield or flow stress.

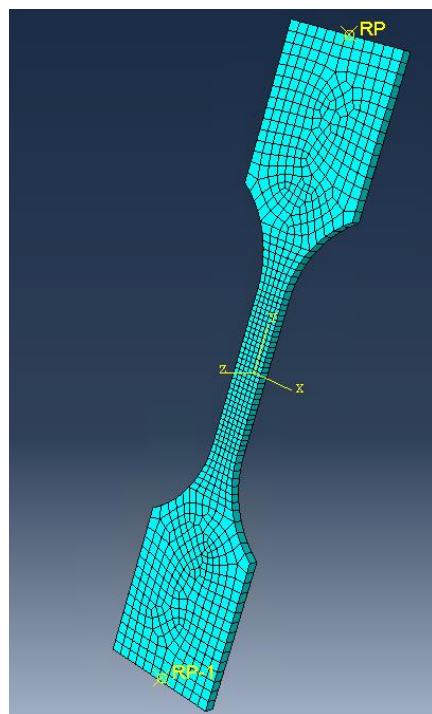


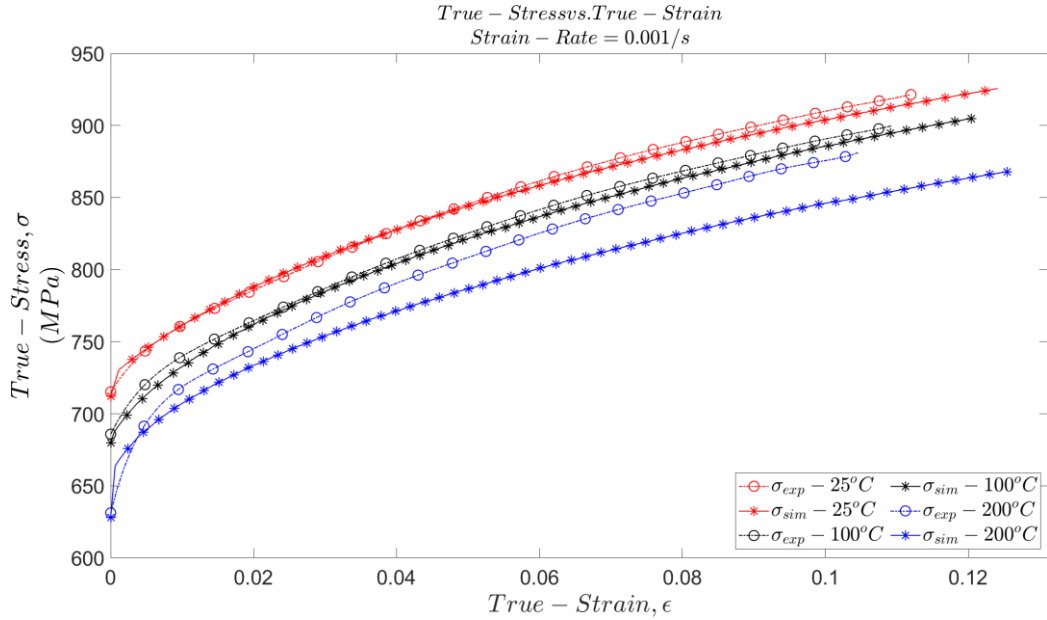
Figure 6.28: Abaqus model developed for the uniaxial tensile analysis.

The model has a total of 785 elements distributed unevenly where a finer mesh density is applied in the deformation region. The elements are also of the C3D8R type i.e. an 8-node linear brick element with reduced integration and hour-glass control, which is the recommended element type for 3D continuum explicit analysis.

The validation analysis executed but with limited success. Only the strain rate of 0.001/s produced some accurate results for certain temperatures in comparison to the experimental results. The results are as presented in the following diagrams in the next section.

6.6.1: Validated Results.

(a)



(b)

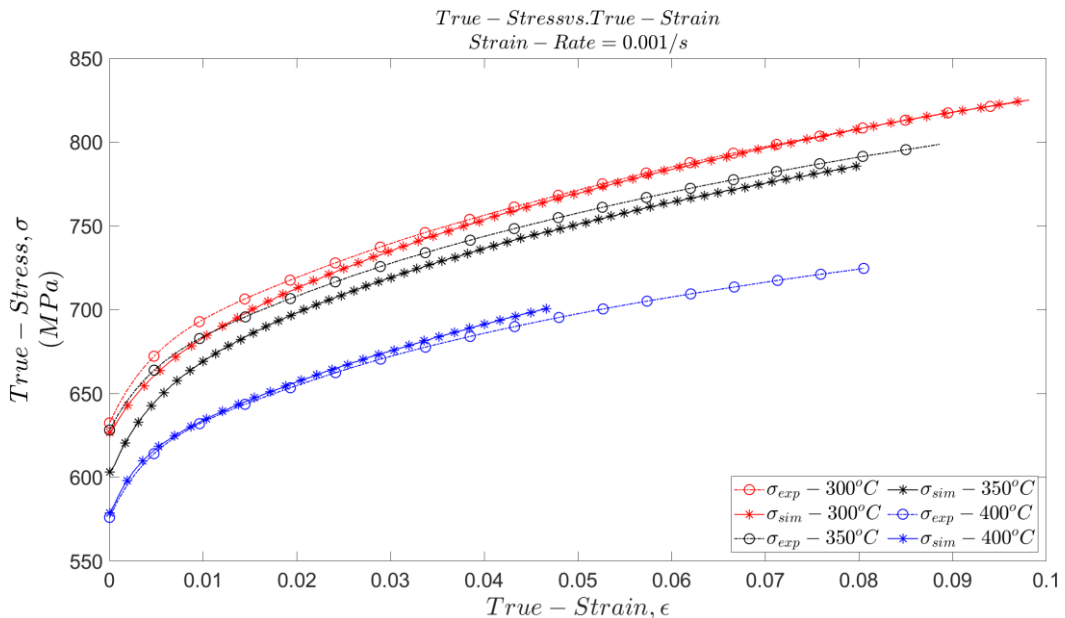


Figure 6.29: Experimental flow curve compared with the simulation result of the flow curve for strain rate of 0.001/s.

The results obtained from the simulation compares quite accurately to those obtained earlier from the results of the optimization for this strain rate i.e. numerical flow curve in figure 6.2.

Also some failed results are presented in the figure below.

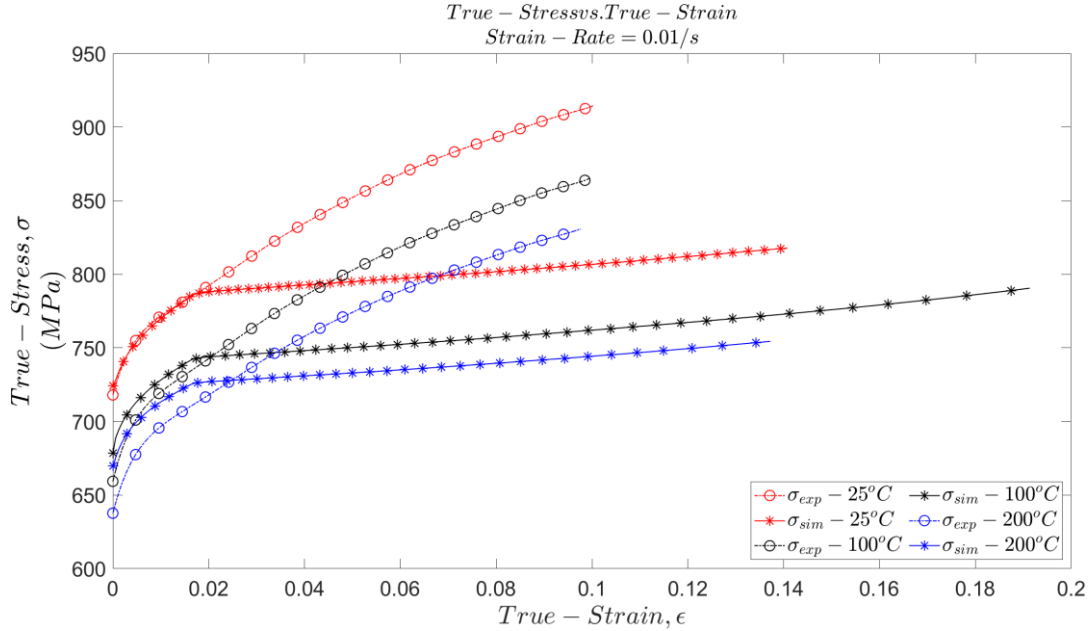


Figure 6.30: Failed simulation results for specific temperatures at strain rate of $0.01/s$.

What would be interesting to note in these failed simulation results is that when compared to the original numerical flow stress curve figure 6.3, it is observed that the simulation flow curve starts out well imitating the numerical flow curve, it however develops inaccurate results all at the same plastic strain of 2%. It is unclear at the moment why this is so. Therefore further analysis is required to ascertain why the user subroutine is able to predict some set of results but incompletely predict some other.

Chapter 7: Why is a Large experimental error and discontinuous trends in the dislocation coefficient obtained?

Two important observations gives answer to the above question. This observation may be made by considering the trend in the strain hardening rate across temperature and strain rate in figures 6.11, 6.12, 6.13, 6.14 and 6.15. We see in these figures that the strain hardening rate across temperatures have clustered curves, while those across strain rate show no consistencies in pattern. Based on the class of materials, the strain hardening rate is expected to decrease with temperature due to increased annihilation events, and decrease with increased strain rate. If we consider how the coefficients are obtained as presented mathematically below:

$$\sigma = \sigma_0 + \frac{\partial \sigma}{\partial \varepsilon} \cdot \Delta \varepsilon$$

$$\frac{\partial \sigma}{\partial \varepsilon} = \text{strain hardening rate}$$

$$\frac{\partial \sigma}{\partial \varepsilon} = \frac{\partial \sigma}{\partial \rho} \cdot \frac{\partial \rho}{\partial \varepsilon}$$

$$\dot{\hat{\rho}}_{cm}^{gn} = M c_{cm}^{gn} \frac{\hat{\rho}_{cm}}{\sqrt{\hat{\rho}_{ci} + \hat{\rho}_{wi}}} \dot{\epsilon}_p$$

$$\dot{\hat{\rho}}_{xy}^{an} = M c_{xy}^{an} \hat{\rho}_{cm} \hat{\rho}_{xy} \dot{\epsilon}_p;$$

$$xy = cm, ci, wi;$$

$$\dot{\hat{\rho}}_{xi}^{ac} = M c_{xi}^{ac} \hat{\rho}_{cm} \sqrt{\hat{\rho}_{xi}} \dot{\epsilon}_p$$

$$\dot{\hat{\rho}}_{xi}^{rm} = M c_{xi}^{rm} \hat{\rho}_{xi} \dot{\epsilon}_p$$

$$\dot{\hat{\rho}}_{wi}^{nc} = M c_{wi}^{nc} \hat{\rho}_{cm} \hat{\rho}_{ci}^{3/2} \dot{\epsilon}_p$$

$$\dot{\hat{\rho}}_{cm}^{tr} = M c_{cm}^{tr} \hat{\rho}_{cm}^{3/2} \dot{\epsilon}_p$$

$$c_{xy}^z = c_{xy0}^z [1 + r_{xy}^z (\hat{T} - 1)^{s_{xy}^z}] \dot{\epsilon}_p^{m_{xy}^z}$$

$$m_{xy}^z = m_{xy0}^z [1 + r_{z_{xy}}^m (\hat{T} - 1)^{s_{z_{xy}}^m}]$$

We deduce from the mathematical excursion above that since inconsistencies are found in the strain hardening behaviour across temperatures and strain rate, obtaining consistent non-discontinuous behaviour of the dislocations are precluded.

Chapter 8: Conclusion and Recommendation.

Although this work concludes with only limited success, based on the following reasons, the numerically obtained constitutive parameters are not accepted;

- The best optimization result obtained has a large error value of 31%. A good results is achieved with a relative error of 0.43% (Amir & Prahl, 2019).
- Overall, the numerically obtained flow curve only fairly match the experimental flow curve, showing varying individual match quality from very good to very bad (especially in the temp range 200°C – 300 °C).
- Inconsistencies in the predictions of the annihilation behaviour, the evolution of dislocation densities at high strain rate and high temperatures, the remobilization at high temperatures, and the existence of discontinuities in a handful of the dislocation evolution curves.
- Inability to be fully validated via simulation for all experiment from which the constitutive parameters were obtained.

Following the experience garnered from several musing of problems encountered in the course of this work, the following recommendations are proposed;

- Experimental data should be fully consistent; this is ensured by use of materials which are not too inhomogeneous. As may be seen from the analysis of the experimental data, the strain hardening behaviour shows no pattern of consistency, the measured flow stress at zero plastic strain also only shows very limited consistency where some data values had to be assumed, and some obtained semi-manually (most of the yield strength in this work) because the experimental results were too out of place compared to what is established in literature for the class of material.

- Smaller specimen on more properly calibrated and set-up test should be used so as to obtain accurate experimental values.
- Given the results obtained from the experiments, it is clear the model is not very stable for inhomogeneous material, therefore the model needs to be improved to withstand such noise that may arise from inconsistent material behaviour.
- The point-wise parameter optimization is not enough to obtain very accurate fit of numerical curve as can be seen in certain numerical flow curve with discontinuities, therefore some constraints need to be imposed on how the points are obtained which captures the original curve shape.
- Some way to calculate a weight function needs to be developed. This will help attack inconsistencies in obtained material curve.
- The effect of the optimization strain-step-length on the optimization result needs to be studied.
- While the strain rate sensitivity parameter is proposed to increase with temperature, in other literature (P. Larour et al., 2013; Prusty & Banerjee, 2020) a decrease is experimentally obtained. This needs to be properly investigated.
- The optimization process requires some imposed constraints informed by actual prior established knowledge, this would help obtain better results especially because optimization are fraught with producing many solutions by changing start values.

References

- Abbaschian, R., Abbaschian, L., & Reed-Hill, R. E. (2009). *Physical Metallurgy Principles* (4th ed.). Cengage Learning, US. <https://doi.org/10.16309/j.cnki.issn.1007-1776.2003.03.004>
- Amir, S., & Prahl, U. (2019). Microstructural constitutive model for polycrystal viscoplasticity in cold and warm regimes based on continuum dislocation dynamics. *Journal of the Mechanics and Physics of Solids*, 122, 205–243.
<https://doi.org/10.1016/j.jmps.2018.09.002>
- ASTM E8. (2010). ASTM E8/E8M standard test methods for tension testing of metallic materials 1. *Annual Book of ASTM Standards* 4, C, 1–27.
<https://doi.org/10.1520/E0008>
- Balasubramanian, S., & Anand, L. (2002). Elasto-viscoplastic constitutive equations for polycrystalline fcc materials at low homologous temperatures. *Journal of the Mechanics and Physics of Solids*, 50(1), 101–126. [https://doi.org/10.1016/S0022-5096\(01\)00022-9](https://doi.org/10.1016/S0022-5096(01)00022-9)
- Barlat, F., Glazov, M. V., Brem, J. C., & Lege, D. J. (2002). A simple model for dislocation behavior, strain and strain rate hardening evolution in deforming aluminum alloys. *International Journal of Plasticity*, 18(7), 919–939. [https://doi.org/10.1016/S0749-6419\(01\)00015-8](https://doi.org/10.1016/S0749-6419(01)00015-8)
- Bergström, Y. (1970). A dislocation model for the stress-strain behaviour of polycrystalline α -Fe with special emphasis on the variation of the densities of mobile and immobile dislocations. *Materials Science and Engineering*, 5(4), 193–200.
[https://doi.org/10.1016/0025-5416\(70\)90081-9](https://doi.org/10.1016/0025-5416(70)90081-9)
- Brunner, D., & Diehl, J. (1991a). Strain-Rate and Temperature Dependence of the Tensile Flow Stress of High-Purity α -Iron above 250 K (Regime I) Studied by Means of Stress-Relaxation Tests. *Physica Status Solidi (A)*, 124(1), 155–170.
<https://doi.org/10.1002/pssa.2211240114>
- Brunner, D., & Diehl, J. (1991b). Temperature and Strain-Rate Dependence of the Tensile Flow Stress of High-Purity α -Iron below 250 K II. Stress/Temperature Regime II and Its Transitions to Regimes I and III. *Physica Status Solidi (A)*, 125(1), 203–216.
<https://doi.org/10.1002/pssa.2211250117>
- Butt, M. Z. (2007). Kinetics of flow stress in crystals with high intrinsic lattice friction. *Philosophical Magazine*, 87(24), 3595–3614.

<https://doi.org/10.1080/14786430701370850>

Cai, M. C., Niu, L. S., Ma, X. F., & Shi, H. J. (2010). A constitutive description of the strain rate and temperature effects on the mechanical behavior of materials. *Mechanics of Materials*, 42(8), 774–781. <https://doi.org/10.1016/j.mechmat.2010.06.006>

Chu, D., & Morris, J. W. (1996). The influence of microstructure on work hardening in aluminum. In *Acta Materialia* (Vol. 44, Issue 7, pp. 2599–2610).
[https://doi.org/10.1016/1359-6454\(95\)00403-3](https://doi.org/10.1016/1359-6454(95)00403-3)

Cottrell, A. H. (2002). Commentary. A brief view of work hardening. *Dislocations in Solids*, 11(C). [https://doi.org/10.1016/S1572-4859\(02\)80002-X](https://doi.org/10.1016/S1572-4859(02)80002-X)

Davoudi, K. M., & Vlassak, J. J. (2018). Dislocation evolution during plastic deformation: Equations vs. discrete dislocation dynamics study. In *Journal of Applied Physics* (Vol. 123, Issue 8). <https://doi.org/10.1063/1.5013213>

de Jong, J. E. (1983). Numerical Analysis of Metalforming Processes: Applications and Experimental Verification. *Proceedings Plasticity of Metals at Finite Strain*, Eds. E. H. Lee and R. L. Mallet, Division Applied Mechanics, Stanford University 1982, 1983, 65–102. <https://doi.org/10.6100/IR107405>

De Rosa, S., Franco, F., Capasso, D., Costagliola, S., & Ferrante, E. (2013). Elasto-viscoplasticity for the metallic materials: a review of the models. In *Aerotecnica Missili & Spazio* (Vol. 92, Issues 1–2, pp. 27–40). <https://doi.org/10.1007/bf03404661>

Dieter, G. E. (2011). Mechanical metallurgy. In *Mechanical metallurgy*.
<https://doi.org/10.5962/bhl.title.35895>

Dingley, D. J., & McLean, D. (1967). Components of the flow stress of iron. *Acta Metallurgica*, 15(5). [https://doi.org/10.1016/0001-6160\(67\)90371-9](https://doi.org/10.1016/0001-6160(67)90371-9)

Domkin, K. (2005). Constitutive models based on dislocation density: Formulation and implementation into finite element codes. In *Luleå University of Technology Department of Applied Physics and Mechanical Engineering Division of Computer Aided Design*. Luleå University of Technology.

Estrin, Y. (1998). Dislocation theory based constitutive modelling: Foundations and applications. *Journal of Materials Processing Technology*, 80–81, 33–39.
[https://doi.org/10.1016/S0924-0136\(98\)00208-8](https://doi.org/10.1016/S0924-0136(98)00208-8)

Estrin, Y., & Mecking, H. (1984). A unified phenomenological description of work hardening and creep based on one-parameter models. *Acta Metallurgica*, 32(1), 57–70.
[https://doi.org/10.1016/0001-6160\(84\)90202-5](https://doi.org/10.1016/0001-6160(84)90202-5)

Estrin, Y., Toth, L. S., Molinari, A., & Brechet, Y. (n.d.). *A dislocation-based model for all hardening stages in large strain deformation.*

Estrin, Y., Tóth, L. S., Molinari, A., & Bréchet, Y. (1998). A dislocation-based model for all hardening stages in large strain deformation. *Acta Materialia*, 46(15).
[https://doi.org/10.1016/S1359-6454\(98\)00196-7](https://doi.org/10.1016/S1359-6454(98)00196-7)

Estrin, Yuri. (1996). Dislocation-Density–Related Constitutive Modeling. In *Unified Constitutive Laws of Plastic Deformation*. <https://doi.org/10.1016/b978-012425970-6/50003-5>

Field, D. P., Merriman, C. C., Allain-Bonasso, N., & Wagner, F. (2012). Quantification of dislocation structure heterogeneity in deformed polycrystals by EBSD. In *Modelling and Simulation in Materials Science and Engineering* (Vol. 20, Issue 2).
<https://doi.org/10.1088/0965-0393/20/2/024007>

Follansbee, P. S., & Kocks, U. F. (1988). A constitutive description of the deformation of copper based on the use of the mechanical threshold stress as an internal state variable. *Acta Metallurgica*, 36(1), 81–93. [https://doi.org/10.1016/0001-6160\(88\)90030-2](https://doi.org/10.1016/0001-6160(88)90030-2)

Gil Sevillano, J., & Aernoudt, E. (1987). Low Energy Dislocation Structures in Highly Deformed Materials*. *Materials Science and Engineering*, 86(C), 67–92.
[https://doi.org/10.1016/0025-5416\(87\)90443-5](https://doi.org/10.1016/0025-5416(87)90443-5)

Gottstein, G. (2004). Physical Foundations of Materials Science. In *Springer-Verlag Berlin Heidelberg GmbH*. Springer-Verlag Berlin Heidelberg GmbH.
<https://doi.org/10.1017/CBO9781107415324.004>

Gray, G. T., Maudlin, P. J., Hull, L. M., Zuo, Q. K., & Chen, S. R. (2005). Predicting material strength, damage, and fracture: The synergy between experiment and modeling. *Journal of Failure Analysis and Prevention*, 5(3), 7–17.
<https://doi.org/10.1361/15477020523725>

Holmedal, B., Marthinsen, K., & Nes, E. (2005). A unified microstructural metal plasticity model applied in testing, processing, and forming of aluminium alloys. *Zeitschrift Fuer Metallkunde/Materials Research and Advanced Techniques*, 96(6).
<https://doi.org/10.3139/146.101067>

Holmquist, T. J., & Johnson, G. R. (1991). DETERMINATION OF CONSTANTS AND COMPARISON OF RESULTS FOR VARIOUS CONSTITUTIVE MODELS. *Journal de Physique IV*, 1, 8.

Hughes, D. A., & Hansen, N. (2018). The microstructural origin of work hardening stages.

Acta Materialia, 148, 374–383. <https://doi.org/10.1016/j.actamat.2018.02.002>

Hughes, Darcy A., Hansen, N., & Bammann, D. J. (2003). Geometrically necessary boundaries, incidental dislocation boundaries and geometrically necessary dislocations. *Scripta Materialia*, 48(2), 147–153. [https://doi.org/10.1016/S1359-6462\(02\)00358-5](https://doi.org/10.1016/S1359-6462(02)00358-5)

Huh, H., Ahn, K., Lim, J. H., Kim, H. W., & Park, L. J. (2014). Evaluation of dynamic hardening models for BCC, FCC, and HCP metals at a wide range of strain rates. *Journal of Materials Processing Technology*, 214(7), 1326–1340.
<https://doi.org/10.1016/j.jmatprotec.2014.02.004>

Hull, D. (1975). *Introduction to Dislocations* (Second Edi). Pergamon Press Ltd., Headington Hill Hall, Oxford OX3 0BW, England.

Humphreys, F. J., & Hatherly, M. (2004). Recrystallization and Related Annealing Phenomena. In *Elsevier*, 2004. Elsevier Ltd.
<https://doi.org/10.1017/CBO9781107415324.004>

Jiang, J., Britton, T. B., & Wilkinson, A. J. (2013). Evolution of dislocation density distributions in copper during tensile deformation. In *Acta Materialia* (Vol. 61, Issue 19, pp. 7227–7239). <https://doi.org/10.1016/j.actamat.2013.08.027>

Kassner, M. E., Geantil, P., & Levine, L. E. (2013). Long range internal stresses in single-phase crystalline materials. In *International Journal of Plasticity* (Vol. 45, pp. 44–60).
<https://doi.org/10.1016/j.ijplas.2012.10.003>

Khan, A. S., & Liang, R. (1999). Behaviors of three BCC metal over a wide range of strain rates and temperatures: Experiments and modeling. *International Journal of Plasticity*, 15(10), 1089–1109. [https://doi.org/10.1016/S0749-6419\(99\)00030-3](https://doi.org/10.1016/S0749-6419(99)00030-3)

Klepaczko, J. (1975). Thermally activated flow and strain rate history effects for some polycrystalline f.c.c. metals. *Materials Science and Engineering*, 18(1), 121–135.
[https://doi.org/10.1016/0025-5416\(75\)90078-6](https://doi.org/10.1016/0025-5416(75)90078-6)

Klepaczko, J. R., & Chiem, C. Y. (1986). On rate sensitivity of f.c.c. metals, instantaneous rate sensitivity and rate sensitivity of strain hardening. *Journal of the Mechanics and Physics of Solids*, 34(1), 29–54. [https://doi.org/10.1016/0022-5096\(86\)90004-9](https://doi.org/10.1016/0022-5096(86)90004-9)

Kuchnicki, S. N., Radovitzky, R. A., & Cuitiño, A. M. (2008). An explicit formulation for multiscale modeling of bcc metals. *International Journal of Plasticity*, 24(12), 2173–2191. <https://doi.org/10.1016/j.ijplas.2008.06.003>

Kuhlmann-Wilsdorf, D. (1989). Theory of plastic deformation: - properties of low energy dislocation structures. *Materials Science and Engineering A*, 113(C), 1–41.

[https://doi.org/10.1016/0921-5093\(89\)90290-6](https://doi.org/10.1016/0921-5093(89)90290-6)

Kuhlmann-Wilsdorf, D. (1999). The theory of dislocation-based crystal plasticity. *Philosophical Magazine A: Physics of Condensed Matter, Structure, Defects and Mechanical Properties*, 79(4), 955–1008. <https://doi.org/10.1080/01418619908210342>

Kuhlmann-Wilsdorf, D. (1987). Energy minimization of dislocations in low-energy dislocation structures. *Physica Status Solidi (A)*, 104(1), 121–144. <https://doi.org/10.1002/pssa.2211040109>

Larour, P. (RWTH A. / I. (2010). Strain rate sensitivity of automotive sheet steels: influence of plastic strain, strain rate, temperature, microstructure, bake hardening and pre-strain. In *Berichte aus dem Institut für Eisenhüttenkunde RWTH Aachen* (Vol. 9, Issue 1).

Larour, P., Bäumer, A., Dahmen, K., & Bleck, W. (2013). Influence of strain rate, temperature, plastic strain, and microstructure on the strain rate sensitivity of automotive sheet steels. In *Steel Research International* (Vol. 84, Issue 5, pp. 426–442). <https://doi.org/10.1002/srin.201200099>

Ledbetter, H. M., & Reed, R. P. (1973). Elastic Properties of Metals and Alloys, I. Iron, Nickel, and Iron-Nickel Alloys. *Journal of Physical and Chemical Reference Data*, 2(3), 531–618. <https://doi.org/10.1063/1.3253127>

Lennon, A. M., & Ramesh, K. T. (2004). The influence of crystal structure on the dynamic behavior of materials at high temperatures. *International Journal of Plasticity*, 20(2), 269–290. [https://doi.org/10.1016/S0749-6419\(03\)00037-8](https://doi.org/10.1016/S0749-6419(03)00037-8)

Li, B. L., Godfrey, A., Meng, Q. C., Liu, Q., & Hansen, N. (2004). Microstructural evolution of IF-steel during cold rolling. *Acta Materialia*, 52(4), 1069–1081. <https://doi.org/10.1016/j.actamat.2003.10.040>

Liang, R., & Khan, A. S. (1999). A critical review of experimental results and constitutive models for BCC and FCC metals over a wide range of strain rates and temperatures. *International Journal of Plasticity*, 15(9), 963–980. [https://doi.org/10.1016/S0749-6419\(99\)00021-2](https://doi.org/10.1016/S0749-6419(99)00021-2)

Lim, H., Battaile, C. C., Carroll, J. D., Boyce, B. L., & Weinberger, C. R. (2015). A physically based model of temperature and strain rate dependent yield in BCC metals: Implementation into crystal plasticity. In *Journal of the Mechanics and Physics of Solids* (Vol. 74, pp. 80–96). <https://doi.org/10.1016/j.jmps.2014.10.003>

Ma, A., Roters, F., & Raabe, D. (2007). A dislocation density based constitutive law for BCC

materials in crystal plasticity FEM. *Computational Materials Science*, 39(1 SPEC. ISS.), 91–95. <https://doi.org/10.1016/j.commatsci.2006.04.014>

Malygin, G. A. (1999). Dislocation self-organization processes and crystal plasticity. In *Uspekhi Fizicheskikh Nauk* (Vol. 169, Issue 9, pp. 1008–1010).
<https://doi.org/10.3367/ufnr.0169.199909c.0979>

McDowell, D. L. (2000). Modeling and experiments in plasticity. *International Journal of Solids and Structures*, 37(1–2), 293–309. [https://doi.org/10.1016/S0020-7683\(99\)00094-3](https://doi.org/10.1016/S0020-7683(99)00094-3)

McDowell, D. L. (2010). A perspective on trends in multiscale plasticity. In *International Journal of Plasticity* (Vol. 26, Issue 9, pp. 1280–1309).
<https://doi.org/10.1016/j.ijplas.2010.02.008>

Mechanical Properties of Materials | MechaniCalc. (n.d.). Retrieved October 1, 2021, from <https://mechanicalc.com/reference/mechanical-properties-of-materials>

Mecking, H., & Kocks, U. F. (1981). Kinetics of flow and strain-hardening. *Acta Metallurgica*, 29(11), 1865–1875. [https://doi.org/10.1016/0001-6160\(81\)90112-7](https://doi.org/10.1016/0001-6160(81)90112-7)

Mishra, N. S., Mishra, S., & Ramaswamy, V. (1989). Analysis of the temperature dependence of strain-hardening behavior in high- strength steel. *Metallurgical Transactions A*, 20(12), 2819–2829. <https://doi.org/10.1007/BF02670174>

Motaman, S. A. H., Schacht, K., Haase, C., & Prahls, U. (2019). Thermo-micro-mechanical simulation of metal forming processes. *International Journal of Solids and Structures*, 178–179, 59–80. <https://doi.org/10.1016/j.ijsolstr.2019.05.028>

Mughrabi, H. (1983). Dislocation wall and cell structures and long-range internal stresses in deformed metal crystals. *Acta Metallurgica*, 31(9), 1367–1379.
[https://doi.org/10.1016/0001-6160\(83\)90007-X](https://doi.org/10.1016/0001-6160(83)90007-X)

Mughrabi, H. (1987). A two-parameter description of heterogeneous dislocation distributions in deformed metal crystals. *Materials Science and Engineering*, 85(C), 15–31.
[https://doi.org/10.1016/0025-5416\(87\)90463-0](https://doi.org/10.1016/0025-5416(87)90463-0)

Nabarro, F. R. N., Basinski, Z. S., & Holt, D. B. (1964). The plasticity of pure single crystals. In *Advances in Physics* (Vol. 13, Issue 50, pp. 193–323).
<https://doi.org/10.1080/00018736400101031>

Nemat-Nasser, S., & Li, Y. (1998). Flow stress of F.C.C. polycrystals with application to OFHC Cu. *Acta Materialia*, 46(2), 565–577. [https://doi.org/10.1016/S1359-6454\(97\)00230-9](https://doi.org/10.1016/S1359-6454(97)00230-9)

Nemat-Nasser, S., Okinaka, T., & Ni, L. (1998). A physically-based constitutive model for
xi

BCC crystals with application to polycrystalline tantalum. *Journal of the Mechanics and Physics of Solids*, 46(6), 1009–1038. [https://doi.org/10.1016/S0022-5096\(97\)00064-1](https://doi.org/10.1016/S0022-5096(97)00064-1)

Nes, E., Pettersen, T., & Marthinsen, K. (2000). On the mechanisms of work hardening and flow-stress saturation. *Scripta Materialia*, 43(1). [https://doi.org/10.1016/S1359-6462\(00\)00363-8](https://doi.org/10.1016/S1359-6462(00)00363-8)

Paul, S. K. (2012). Predicting the flow behavior of metals under different strain rate and temperature through phenomenological modeling. In *Computational Materials Science* (Vol. 65, pp. 91–99). <https://doi.org/10.1016/j.commatsci.2012.06.039>

Prusty, B. G., & Banerjee, A. (2020). Structure-property correlation and constitutive description of structural steels during hot working and strain rate deformation. In *Materials* (Vol. 13, Issue 3). <https://doi.org/10.3390/ma13030556>

Pulkkinen, S. (2008). *A Review of Methods for Unconstrained Optimization : Theory , Implementation and Testing*. November, 1–104.

Rittel, D., Kidane, A. A., Alkhader, M., Venkert, A., Landau, P., & Ravichandran, G. (2012). On the dynamically stored energy of cold work in pure single crystal and polycrystalline copper. In *Acta Materialia* (Vol. 60, Issue 9, pp. 3719–3728). <https://doi.org/10.1016/j.actamat.2012.03.029>

Rollett, A. D., & Kocks, U. F. (1993). A Review of the Stages of Work Hardening. *Solid State Phenomena*, 35–36, 1–18. <https://doi.org/10.4028/www.scientific.net/ssp.35-36.1>

Roters, F., Eisenlohr, P., Hantcherli, L., Tjahjanto, D. D., Bieler, T. R., & Raabe, D. (2010). Overview of constitutive laws, kinematics, homogenization and multiscale methods in crystal plasticity finite-element modeling: Theory, experiments, applications. In *Acta Materialia* (Vol. 58, Issue 4, pp. 1152–1211). <https://doi.org/10.1016/j.actamat.2009.10.058>

Roters, F., Raabe, D., & Gottstein, G. (2000). Work hardening in heterogeneous alloys - a microstructural approach based on three internal state variables. *Acta Materialia*, 48(17). [https://doi.org/10.1016/S1359-6454\(00\)00289-5](https://doi.org/10.1016/S1359-6454(00)00289-5)

Rusinek, A., Zaera, R., & Klepaczko, J. R. (2007). Constitutive relations in 3-D for a wide range of strain rates and temperatures - Application to mild steels. In *International Journal of Solids and Structures* (Vol. 44, Issue 17, pp. 5611–5634). <https://doi.org/10.1016/j.ijsolstr.2007.01.015>

Salvado, F. C., Teixeira-Dias, F., Walley, S. M., Lea, L. J., & Cardoso, J. B. (2017). A review on the strain rate dependency of the dynamic viscoplastic response of FCC metals. *Progress*

in Materials Science, 88, 186–231. <https://doi.org/10.1016/j.pmatsci.2017.04.004>

Schulze, V., & Vöhringer, O. (2000). Influence of alloying elements on the strain rate and temperature dependence of the flow stress of steels. *Metallurgical and Materials Transactions A: Physical Metallurgy and Materials Science*, 31(3), 825–830.
<https://doi.org/10.1007/s11661-000-0026-1>

Sedláček, R., & Blum, W. (2002). Microstructure-based constitutive law of plastic deformation. *Computational Materials Science*, 25(1–2), 200–206.
[https://doi.org/10.1016/S0927-0256\(02\)00264-1](https://doi.org/10.1016/S0927-0256(02)00264-1)

Seeger, A. (2002). Peierls barriers, kinks, and flow stress: Recent progress. *Zeitschrift Fuer Metallkunde/Materials Research and Advanced Techniques*, 93(8), 760–777.
<https://doi.org/10.3139/146.020760>

Shanthraj, P., & Zikry, M. A. (2011). Dislocation density evolution and interactions in crystalline materials. *Acta Materialia*, 59(20).
<https://doi.org/10.1016/j.actamat.2011.08.041>

Simo, J. C. (1998). Numerical analysis and simulation of plasticity. *Handbook of Numerical Analysis*, 6(Part 3), 183–499. [https://doi.org/10.1016/S1570-8659\(98\)80009-4](https://doi.org/10.1016/S1570-8659(98)80009-4)

Simulia. (2017). Abaqus 6.11 Theory Manual. *Providence, RI, USA: DS SIMULIA Corp*, 1172.
<http://scholar.google.com/scholar?hl=en&btnG=Search&q=intitle:Abaqus+6.11+theory+manual#o>

Stainier, L., Cuitiño, A. M., & Ortiz, M. (2002a). A micromechanical model of hardening, rate sensitivity and thermal softening in bcc single crystals. *Journal of the Mechanics and Physics of Solids*, 50(7), 1511–1545. [https://doi.org/10.1016/S0022-5096\(01\)00114-4](https://doi.org/10.1016/S0022-5096(01)00114-4)

Stainier, L., Cuitiño, A. M., & Ortiz, M. (2002b). A micromechanical model of hardening, rate sensitivity and thermal softening in bcc single crystals. *Journal of the Mechanics and Physics of Solids*, 50(7). [https://doi.org/10.1016/S0022-5096\(01\)00114-4](https://doi.org/10.1016/S0022-5096(01)00114-4)

Tang, B., Wu, F., Wang, Q., Li, C., Liu, J., & Ge, H. (2020). Numerical and experimental study on ductile fracture of quenchable boron steels with different microstructures. *International Journal of Lightweight Materials and Manufacture*, 3(1), 55–65.
<https://doi.org/10.1016/j.ijlmm.2019.07.001>

Testa, G., Bonora, N., Ruggiero, A., & Iannitti, G. (2020). Flow stress of bcc metals over a wide range of temperature and strain rates. In *Metals* (Vol. 10, Issue 1).
<https://doi.org/10.3390/met10010120>

Voyadjis, G. Z., & Abed, F. H. (2005). Microstructural based models for bcc and fcc metals

- with temperature and strain rate dependency. *Mechanics of Materials*, 37(2-3 SPEC. ISS.), 355–378. <https://doi.org/10.1016/j.mechmat.2004.02.003>
- Wagoner, R. H., & Chenot, J.-L. (2001). Sheet-Metal Formability Tests. In *Metal Forming Analysis* (Vol. 4, Issue 1, pp. 177–204). <https://doi.org/10.1017/cbo9781139087070.009>
- Xiao, Y. Z., & Chen, J. (2009). A review of research in macroscopic hardening models in numerical simulation of sheet metal forming. *Suxing Gongcheng Xuebao/Journal of Plasticity Engineering*, 16(4), 51–58. <https://doi.org/10.3969/j.issn.1007-2012.2009.04.0011>
- Yalcinkaya, T., Brekelmans, W. A. M., & Geers, M. G. D. (2008). BCC single crystal plasticity modeling and its experimental identification. *Modelling and Simulation in Materials Science and Engineering*, 16(8). <https://doi.org/10.1088/0965-0393/16/8/085007>
- Zehetbauer, M. (1993). Cold work hardening in stages IV and V of F.C.C. metals-II. Model fits and physical results. *Acta Metallurgica Et Materialia*, 41(2), 589–599. [https://doi.org/10.1016/0956-7151\(93\)90089-B](https://doi.org/10.1016/0956-7151(93)90089-B)
- Zehetbauer, M., & Seumer, V. (1993). Cold work hardening in stages IV and V of F.C.C. metals-I. Experiments and interpretation. *Acta Metallurgica Et Materialia*, 41(2), 577–588. [https://doi.org/10.1016/0956-7151\(93\)90088-A](https://doi.org/10.1016/0956-7151(93)90088-A)
- Zerilli, F. J. (2004). Dislocation mechanics-based constitutive equations. *Metallurgical and Materials Transactions A: Physical Metallurgy and Materials Science*, 35 A(9), 2547–2555. <https://doi.org/10.1007/s11661-004-0201-x>

List of Figures

Figure 2.1: Regime of strain rate/loading rate (Prusty & Banerjee, 2020).....	4
Figure 2.2: Deformation process extent and rate (Prusty & Banerjee, 2020).	4
Figure 2.3: Resolution for plasticity including the typical minimum explicit length scale of resolution at each scale (McDowell 2000).....	5
Figure 2.4: The Tensile Stress-Strain Curve (Gray et al., 2005).....	8
Figure 2.5: The true and engineering stress-strain curve (Mechanical Properties of Materials MechaniCalc, n.d.)	10
Figure 2.6: Schematic of grain microstructural subdivision during plastic deformation (Amir & Prahl, 2019).	11
Figure 3.1: Yield loci in 2D principal stress space (Dieter, 2011).....	14
Figure 3.2: The Von Mises and Tresca yield surfaces in 3D space (Dieter, 2011).....	14
Figure 4.1: Schematic of the double-kink mechanism (Stainier et al., 2002b).	32
Figure 4.2: The variation of the viscous/thermal/friction stress with temperature at constant strain rates (P. (RWTH A. / I. Larour, 2010).....	35
Figure 4.3: The variation of the viscous/thermal/friction stress with strain rate at constant temperatures (P. (RWTH A. / I. Larour, 2010).	36
Figure 4.4: Schematic representation of the multiscale nature current model (Amir & Prahl, 2019).....	44
Figure 6.1: Comparative displays of test yield stress and computed stress for 0.0001/s strain rate at all test temperatures.	59
Figure 6.2: Comparative displays of test yield stress and computed stress for 0.001/s strain rate at all test temperatures.	60
Figure 6.3: Comparative displays of test yield stress and computed stress for 0.01/s strain rate at all test temperatures.	62
Figure 6.4: Comparative displays of test yield stress and computed stress for 0.1/s strain rate at all test temperatures.....	63
Figure 6.5: Experimental determined yield stress at zero plastic strain across all test temperature and strain rates.....	64
Figure 6.6: Numerically determined yield stress at zero plastic strain across all test temperature and strain rates.....	65
Figure 6.7: Viscous stress as a function of temperature at all test strain rate.	66

Figure 6.8: Shear-Modulus-Mean-Interaction-Strength for the cell immobile dislocation as a function of temperature.....	66
Figure 6.9: Shear-Modulus-Mean-Interaction-Strength for the wall immobile dislocation as a function of temperature.....	67
Figure 6.10: Strain rate sensitivity parameter of the viscous stress as a function of temperature.....	68
Figure 6.11: Experimental (a), and numerical (b), strain hardening rate for all temperatures at a strain rate of 0.0001/s.....	70
Figure 6.12: Experimental (a), and numerical (b), strain hardening rate for all temperatures at a strain rate of 0.001/s.....	71
Figure 6.13: Experimental (a), and numerical (b), strain hardening rate for all temperatures at a strain rate of 0.01/s.....	72
Figure 6.14: Experimental (a), and numerical (b), strain hardening rate for all temperatures at a strain rate of 0.1/s.....	73
Figure 6.15: Strain hardening rate at all test strain rate and temperatures.....	77
Figure 6.16: Total dislocation density as plastic deformation progresses at strain rates 0.0001/s, (a), 0.001/s, (b), 0.01/s (c), and 0.1/s, (d).....	79
Figure 6.17: Cell mobile dislocation density at all test strain rate and temperatures.....	82
Figure 6.18: Cell immobile dislocation density for all test strain rates and temperatures... ..	85
Figure 6.19: Wall immobile dislocation density for all test strain rates and temperatures..	87
Figure 6.20: Strain hardening contribution from cell and wall immobile dislocation at all test temperatures and strain rates.....	92
Figure 6.21: Cell mobile trapping coefficient for all test temperatures and strain rates.....	93
Figure 6.22: Wall immobile remobilization coefficient for all test temperatures and strain rates.....	94
Figure 6.23: Cell immobile remobilization coefficient at all test temperatures for strain rates of 0.0001/s and 0.001/s.....	95
Figure 6.24: Cell immobile remobilization coefficient at all test temperatures for strain rate of 0.01/s.....	96
Figure 6.25: Cell immobile remobilization coefficient at all test temperatures for strain rate of 0.1/s.....	96
Figure 6.26: Wall immobile nucleation coefficient at all test temperatures for test strain rates.....	97
Figure 6.27: Annihilation coefficients for wall immobile (a), cell immobile (b and c), and cell mobile dislocations.....	99
Figure 6.28: Abaqus model developed for the uniaxial tensile analysis.....	101
Figure 6.29: Experimental flow curve compared with the simulation result of the flow curve for strain rate of 0.001/s	102

Figure 6.30: Failed simulation results for specific temperatures at strain rate of 0.01/s.. 103

List of Tables

Table 4.1: Equations of Quasistatic Models.....	27
Table 4.2: Table showing expression for dislocation properties.	32
Table 4.3: Table showing different expression for the activation energy and resulting thermal stress.....	34
Table 4.4: Table showing other expressions for the thermal stress.	35
Table 6.1: Chemical Composition of the S700 single phase steel specimens.	53
Table 6.2: Reference constant and normalization parameters.	57
Table 6.3: Table of constitutive parameters determined from the optimization.	57

List of Equations

Equation 3.1	13
Equation 3.2	15
Equation 3.3	15
Equation 3.4	23
Equation 3.5	24
Equation 4.1	38
Equation 4.2.a	39
Equation 4.3	39
Equation 6.1.a	54
Equation 6.2.b	54
Equation 6.3.a	54
Equation 6.4.a	55
Equation 6.5.a	55
Equation 6.6	56